2013

Induction Motors With Rotor Helical Motion

Ebrahim Amiri
Louisiana State University and Agricultural and Mechanical College, eamiri3@lsu.edu

INDUCTION MOTORS WITH ROTOR HELICAL MOTION

A Dissertation

Submitted to the Graduate Faculty of the
Louisiana State University and
Agricultural and Mechanical College
in partial fulfillment of the
requirements for the degree of
Doctor of Philosophy

in

The Division of Electrical and Computer Engineering
School of Electrical Engineering and Computer Science

by
Ebrahim Amiri
B.S., Amirkabir University of Technology, 2005
M.S., Amirkabir University of Technology, 2008
December 2013

This dissertation would not have been possible without the endless support from:

My Mother, My Father, My Brothers and My Advisor

ACKNOWLEDGEMENTS

I would like to express my gratitude to my advisor and mentor, Dr. Ernest A. Mendrela, for being a constant source of encouragement during all the years of my graduate school.

I would like to thank Dr. Leszek Czarnecki not only for being a part of my dissertation committee, but also for providing valuable guidance in and out of class during my graduate studies. I would also like to thank the other dissertation committee members, Dr. Shahab Mehraeen, Dr. Pratul K. Ajmera and Dr. Gestue Olafsson for their valuable time and suggestions in preparing this dissertation.

TABLE OF CONTENTS

LIST OF TABLES

LIST OF ILLUSTRATIONS

ABSTRACT

Performance analysis of the twin-armature rotary-linear induction motor, a type of motor with two degrees of mechanical freedom, is the subject of this dissertation. The stator consists of a rotary armature and linear armature placed aside one another. Both armatures have a common rotor which can be either solid or cage rotor. The rotor can move rotary, linearly or with helical motion. The linear motion generates dynamic end effect on both armatures. Modeling such an effect in rotary armature is a significant challenge as it requires a solution considering motion with two degrees of mechanical freedom. Neither of the available FEM software package is currently capable to solve such a problem. The approach used to address linear motion on rotary armature is based on the combination of transient time-stepping finite element model and frequency domain slip frequency technique. The results obtained from FEM modeling are partially verified by test carried out on experimental model of the motor to validate the theoretical modeling of the motor.

FEM performance analysis of the linear armature is rather straightforward as it only involves motion in one direction similar to a conventional linear induction motor. However, due to the finite core length and open magnetic circuit in the direction of motion, the air gap flux density distribution can still be distorted, even at zero axial speed. This distortion is known as static end effect. A novel equivalent circuit steady-state model for linear induction motors is presented to include this phenomenon. The novelty resides in classification and inclusion of end effects in the equivalent circuit. Duncan model is used to address dynamic end effect and appropriately modified to account for the saturation of back iron. The static end effect, which manifests itself by the alternating field component, is represented by additional circuit branch

similar to the ones of motor with alternating magnetic field. The results regarding determination of basic performance characteristics are compared with those obtained from finite element simulation. The proposed equivalent circuit considers all major phenomena in linear motors and is more accurate than the conventional equivalent circuit available in the literature.

Finally, the performance of the motor with solid layer is compared with the one with cage rotor. It is concluded that, in general, motor with the cage rotor has the better performance compared to the solid double layer rotor.

CHAPTER 1 : OVERVIEW OF THE PROJECT

A demand for sophisticated motion is steadily increasing in several advanced application fields, such as robotics, tooling machines, pick-and-place systems, etc. These kinds of applications require implementation of at least two or more conventional motors/actuators, often operating with different type of mechanical gear. Electric motors/actuators that are able directly perform complex motion (with multiple degrees of mechanical freedom – multi-DoMF) may provide appreciable benefits in terms of performances, volume, weight and cost.

1.1 Topologies of Induction Motors with Two Degrees of Mechanical Freedom

Several topologies of electric motors featuring a multi-DoMF structure were reviewed in the technical literatures [1, 2]. Considering the geometry, three classes of motors can be distinguished:

- X-Y motors – flat structure
- Rotary-linear motor – cylindrical geometry
- Spherical motors – spherical geometry

X-Y motors: X-Y motors, also called planar motors, are the machines which are able to translate on a plane, moving in the direction defined by two space co-ordinates. They may be usefully employed for precision positioning in various manufacturing systems such as drawing devices or drive at switch point of guided road/e.g. railway. The representative of X-Y motors is shown schematically in Fig. 1-1. A primary winding consist of two sets of three phase windings placed perpendicularly to one another. Therefore, magnetic traveling fields produced by each winding are moving perpendicularly to one another as well. Secondary part can be made of non-

magnetic conducting sheet (aluminum, copper) backed by an iron plate. The motor with a rotor rectangular grid-cage winding is another version that can be considered.

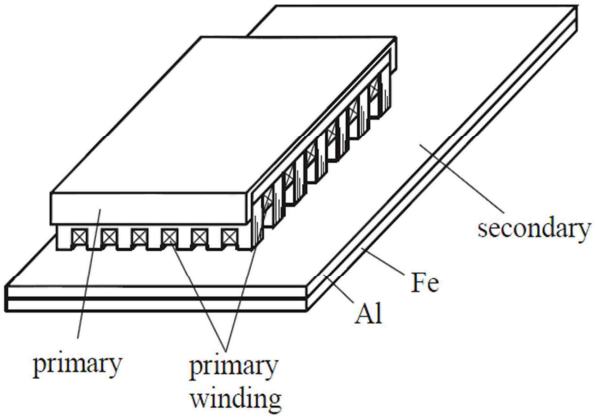

Fig 1-1. Construction scheme of X-Y induction motor [1].

The forces produced by each of traveling fields can be independently controlled contributing to the control of both magnitude and direction of the resultant force. This in turn controls the motion direction of the X-Y motor.

Rotary-linear motors: Mechanical devices with multiple degrees of freedom are widely utilized in industrial machinery such as boring machines, grinders, threading, screwing, mounting, etc. Among these machines those which evolve linear and rotary motion, independently or simultaneously, are of great interest. These motors, which are able effectively generate torque and axial force in a suitably controllable way, are capable of producing pure rotary motion, pure linear motion or helical motion and constitute one of the most interesting topologies of multi-degree-of freedom machines [3]. Some examples of such actuators have already been the subject of studies or patents [4,5]. A typical rotary-linear motor with twin-armature is shown in Fig. 1-2. A stator consists of two armatures; one generates a rotating

magnetic field, another traveling magnetic field. A solid rotor, common for the two armatures is applied. The rotor consists of an iron cylinder covered with a thin copper layer. The rotor cage winding that looks like grid placed on cylindrical surface is another version to be studied. The direction of the rotor motion depends on two forces: linear (axially oriented) and rotary, which are the products of two magnetic fields and currents induced in the rotor. By controlling the supply voltages of two armatures independently, the motor can either rotate or move axially or can perform a helical motion.

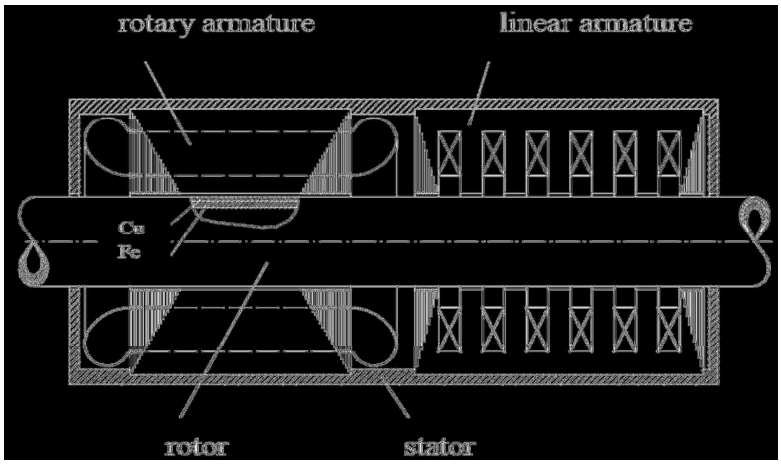

Fig 1-2. Scheme of twin armature rotary-linear induction motor [1].

Spherical motors: The last class of multi-DoMF motors has spherical structure. The rotor is able to turn around axis, which can change its position during the operation. Presently, such actuators are mainly proposed for pointing of micro-cameras and laser beams, in robotic, artificial vision, alignment and sensing applications [3]. In larger sizes, they may be also used as active wrist joints for robotic arms. Fig. 1-3 shows one of the designs in which the rotor driven by two magnetic fields generated by two armatures moving into two directions perpendicular to one another. This design is a counterpart of twin-armature rotary-linear motor.

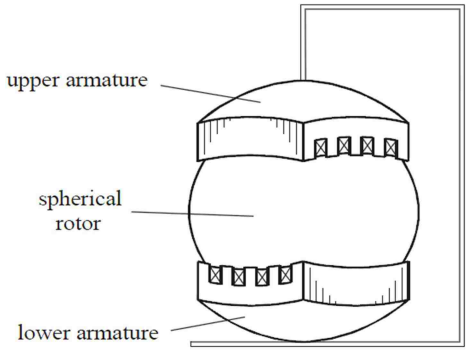

Fig 1-3. Construction scheme of twin-armature induction motor with spherical rotor [1].

The object of the study is a rotary-linear induction motor. The literature review on this type of the motor and the related phenomena are enclosed in chapter 2 and 3.

1.2 Objectives of the Dissertation

The following are the objectives of this project:

- To determine the performance of rotary-linear motor with inclusion of end effects.
- To develop the equivalent circuit of rotary-linear induction motor with inclusion of parameter, which characterize motor end effects.
- To compare the performance of twin-armature rotary-linear induction motors of two different rotors: solid, and cage type rotor.

1.3 Structure of Dissertation

The dissertation consists of the following chapters:

Chapter 2 reviews the literature on rotary-linear induction motors, their topology and principle of operation on the basis of the magnetic field moving helically. A literature review is done on the mathematical model of helical-motion induction motor.

Chapter 3 describes the phenomena known as end effects caused by finite length of the armature and its negative influences on the motor performance.

Chapter 4 discusses briefly the information about numerical methods used in the project. Basic Maxwell's equations and approach to solve them are described. Finite element method (FEM) tools used in the project such as FEMM and 3D Maxwell are presented.

Chapter 5 presents a construction of a twin-armature rotary-linear induction motor with solid double layer rotor and its design data. An equivalent circuit of the motor is developed with inclusion of parameters responsible for end effects. The circuit parameters were determined using the 3-D (FEM). The performance of the motor in steady-state condition is studied and compared to the motor with the cage rotor. Comparison of results obtained from computer simulation and experimental test has been done.

Chapter 6 presents the conclusions along with the future work on this project.

CHAPTER 2 : LITERATURE REVIEW ON ROTARY-LINEAR INDUCTION MOTORS

2.1 Topology of Rotary-Linear Induction Motors

Rotary-linear motors, able to provide both axial force and torque, represent an interesting solution for managing combined linear and rotary motions, as an alternative to complex motion drives, which usually apply two separated conventional motors. Regardless of the type of rotor, cage or solid, rotary linear induction motors can be classified according to the type of stator.

2.1.1 Twin-Armature Rotary-Linear Induction Motor

The scheme of the motor construction was shown earlier in Fig. 1-2. Two armatures produce the rotating and traveling magnetic fields that act on a common rotor. The result of that is the torque and thrust, which drive the rotor with a helical motion. If the two armatures are not too close to one another, the electromagnetic interaction between them is negligible. Thus the motor can be considered as a pair of two independent motors, rotary and linear, whose rotors are coupled stiffly by a mechanical clutch. However, since each armature has a finite length, a phenomena called end effects takes place and deteriorate the performance of the motor. The influence of these effects on the magnetic field of both armature and further – on torque and thrust is brought in Chapter 3 in details.

2.1.2 Double-Winding Rotary-Linear Induction Motor

The double-winding rotary-linear motor is a modification of the twin-armature motor. It has similar rotary and linear windings put together in the same armature core in such a way that one winding overlaps another (Fig 2-1). Since the windings are placed perpendicularly to one

another no electromagnetic interaction between them is expected under the assumption of an unsaturated magnetic circuit. The operation of the motor can be regarded as the work of two independent motors, both rotary and tubular-linear, whose rotors are coupled rigidly together. In the real motor, where the iron core can be partially saturated by the cumulative interaction of magnetic fields of both windings the mutual magnetic interaction should be taken into account.

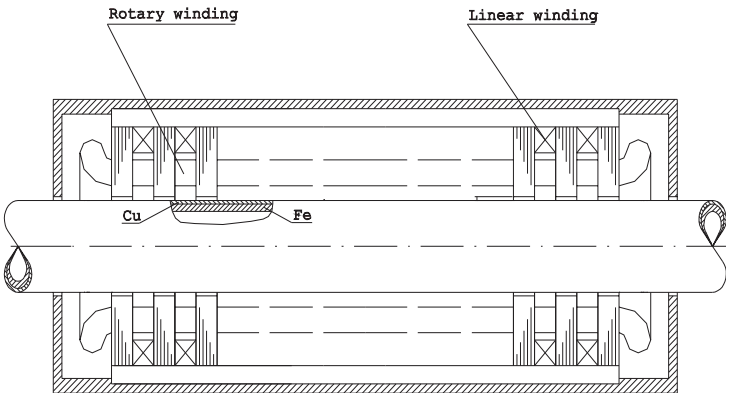

Fig 2-1. Scheme of double-winding rotary-linear induction motor [1].

The mathematical model of the motor was derived in [1] with the assumption that all motor elements are being linear. In this case the electromagnetic properties do not differ from that of the twin-armature motor. The only possible difference relates to the magnetic flux density distribution on the rotor surface

2.2 Mathematical Model of Induction Motor with Helical Magnetic Field

The basic and most comprehensive research on induction motors with 2DoMF is contained in the book [1]. The analysis of these motors is based on theory of the induction motors whose magnetic field is moving in the direction determined by two space coordinates. According to this theory the magnetic field of any type of motor with 2 DoMF can be

represented by the sum of two or more rotating-traveling field what allows to consider the complex motion of the rotor as well as end effects caused by the finite length of stator. In the next subsections a sketch of theory of the motor with the rotating-traveling magnetic field whose rotor is moving with helical motion is presented.

2.2.1 Definition of Magnetic Field and Rotor Slip

Magnetic field description: The magnetic field moving helically in the air-gap is represented by the magnetic flux density B wave moving in the direction placed between two co-ordinates z and θ (Fig. 2-2).

It can be expressed by the following formula [1]:

$$B = B_m \exp\left[j\left(\omega t - \frac{\pi}{\tau_\theta}\theta - \frac{\pi}{\tau_z} z \right)\right] \tag{2-1}$$

where τ_θ and τ_z are pole pitches in θ and z directions (see Fig. 2-2)

The electromagnetic force that exerts on the rotor is perpendicular to the wave front and can be divided into two components: F_z – linear force, F_θ - rotary component (Fig. 2-2). The relationships between force components are:

$$\frac{F_\theta}{F_z} = ctg\,\alpha\ , \qquad F_\theta = F\cos\alpha \tag{2-2}$$

where

$$\cot\alpha = \frac{\tau_z}{\tau_\theta} \tag{2-3}$$

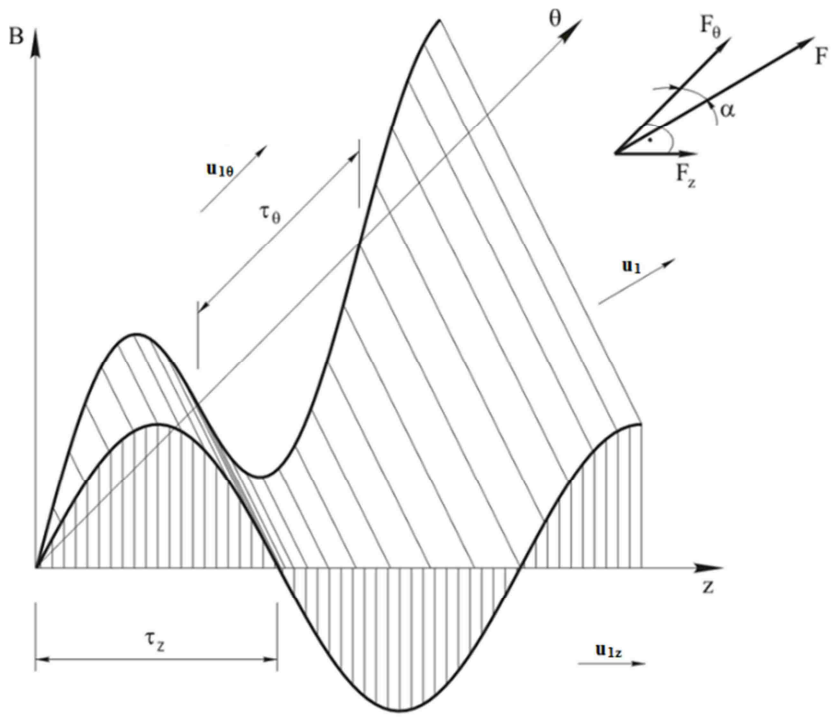

Fig 2-2. Magnetic field wave moving into direction between two spaces coordinates [1].

The physical model of the motor which could generate such a field is shown in Fig. 2-3.

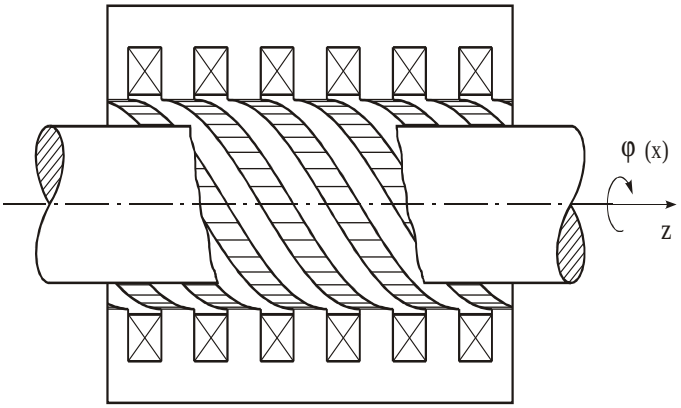

Fig 2-3. Rotary-linear induction motor with rotating-traveling magnetic field [1].

Rotor slip: To derive a formula for the rotor slip the motor is first considered to operate at asynchronous speed. Meaning, an observer standing on the rotor surface feels a time variant magnetic field. Therefore, magnetic field for a given point $P(\theta_1, z_1)$ (Fig. 2-4) on the rotor surface is varying in time and expressed by the following equation:

$$B(t, \theta_1, z_1) = B_m \exp\left[j\left(\omega t - \frac{\pi}{\tau_\theta}\theta_1 - \frac{\pi}{\tau_z}z_1\right)\right] = var \tag{2-4}$$

Eqn (2-4) is true if:

$$\omega t - \frac{\pi}{\tau_\theta}\theta_1(t) - \frac{\pi}{\tau_z}z_1(t) = \psi(t) \tag{2-5}$$

where $\psi(t)$ is the angle between point *P* and the wave front of the magnetic field wave.

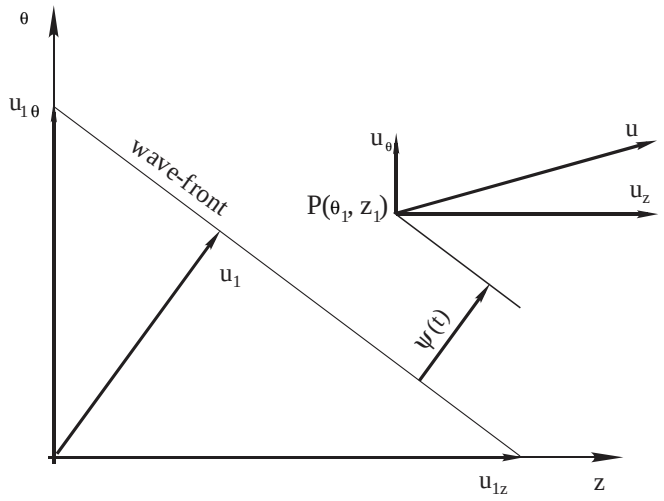

Fig 2-4. Rotary-linear slip derivation [1].

Differentiating Eqn. (2-5) with respect to time t yields:

$$\omega - \frac{\pi}{\tau_\theta}\omega_\theta - \frac{\pi}{\tau_z}u_z = \omega_2 \tag{2-6}$$

where ω_2 (slip speed) is the angular speed of point P with respect to the stator field, and ω_θ and u_z are the angular and linear speeds of the rotor, respectively.

The field velocities along θ and z axes are expressed by the equations:

$$\omega_{1\theta} = 2\tau_\theta f \ , \qquad u_{1z} = 2\tau_z f \tag{2-7}$$

Inserting (2-7) to (2-6), it takes the form:

$$\omega - \frac{\omega}{\omega_{1\theta}}\omega_\theta - \frac{\omega}{u_{1z}}u_z = \omega_2 \tag{2-8}$$

Similarly, as in the theory of conventional induction motors, it can be written:

$$\omega_2 = \omega s \tag{2-9}$$

where s is the slip and ω is the speed of rotating field.

From (2-8) and (2-9) the following equation for rotor slip is finally obtained:

$$s_{\theta z} = 1 - \frac{\omega_\theta}{\omega_{1\theta}} - \frac{u_z}{u_{1z}} \tag{2-10}$$

The two dimensional rotor slip $s_{\theta z}$ obtained in Eqn (2-10) is a function of rotary and linear rotor speed components as well as the speeds of the magnetic field moving along two space coordinates. If the motion of rotor is blocked along one of the coordinates, this slip takes the form known for motors with one degree of mechanical freedom. For example: if the rotor is blocked in the axial direction, the u_z component drops to zero and the slip takes the form:

$$s_{\theta z} = s_{\theta} = 1 - \frac{\omega_{\theta}}{\omega_{1\theta}} \tag{2-11}$$

which has the form of rotor slip in the theory of conventional induction motor.

2.2.2 Equivalent Circuit

For the induction motor with rotating-travelling field the equivalent circuit is shown in Fig. 2-5, which corresponds to the well-known circuit of rotary induction motor. The only difference is in the rotor slip which for rotary-linear motor depends on both rotary and linear rotor speeds.

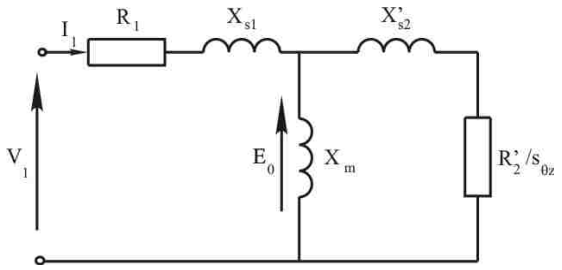

Fig 2-5. Equivalent circuit of induction motor with rotating-travelling magnetic field.

Similarly to the conventional rotary motors, the secondary resistance can be split into two resistances as shown in Fig. 2-6. R'_2 represents the power loss in the rotor windings and the second part ($R'_2 \frac{1-s_{\theta z}}{s_{\theta z}}$) contributes to mechanical power P_m.

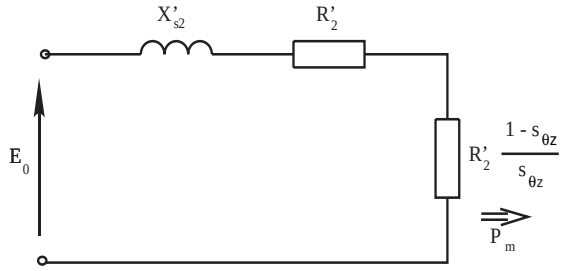

Fig 2-6. Equivalent circuit of rotor of rotary-linear induction motor [1].

The mechanical power of the resultant motion between θ and z axis is proportional to the resistance $R_2' \frac{1-s_{\theta z}}{s_{\theta z}}$ and is equal to:

$$P_m = mR_2' \frac{1 - s_{\theta z}}{s_{\theta z}} I_2'^2 \tag{2-12}$$

where m is the number of phases.

Inserting Eqn. (2-10) into Eqn. (2-12), yields:

$$P_m = mI_2'^2 \frac{R_2'}{s_{\theta z}} \left(\frac{\omega_\theta}{\omega_{1\theta}} + \frac{u_z}{u_{1z}} \right) \tag{2-13}$$

The resultant mechanical power P_m can be expressed in the form of its component in θ and z direction:

$$P_m = P_{m\theta} + P_{mz} \tag{2-14}$$

From (2-11), (2-13) and (2-14),

$$P_{m\theta} + P_{mz} = mR_2' \frac{1 - s_\theta}{s_{\theta z}} I_2'^2 + mR_2' \frac{1 - s_z}{s_{\theta z}} I_2'^2 \tag{2-15}$$

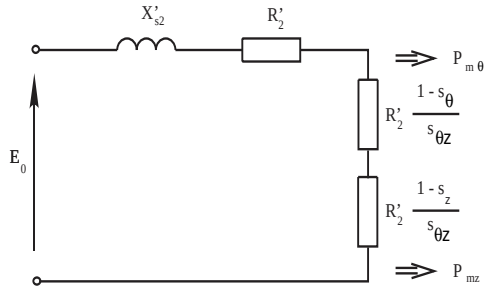

Fig 2-7. Equivalent circuit of rotor of rotary-linear induction motor with mechanical resistance split into two components [1].

Therefore, Fig. 2-6 can be redrawn in terms of the resistance split into two components as shown in Fig. 2-7.

2.2.3 Electromechanical Characteristics

Unlike conventional rotary motors with the curvy characteristics of electromechanical quantities versus slip, electromechanical quantities in rotary-linear motor cannot be interpreted in one dimensional shape and should be plotted in a surface profile as a function of either slip $s_{\theta z}$ or speed components u_θ and u_z. The circumferential speed u_θ is expressed as follows:

$$u_\theta = R_r \,.\, \omega_\theta \tag{2-16}$$

where R_r is the rotor radius.

As an example, the force-slip characteristic of a typical rotary-linear motor is plotted in Fig. 2-8.

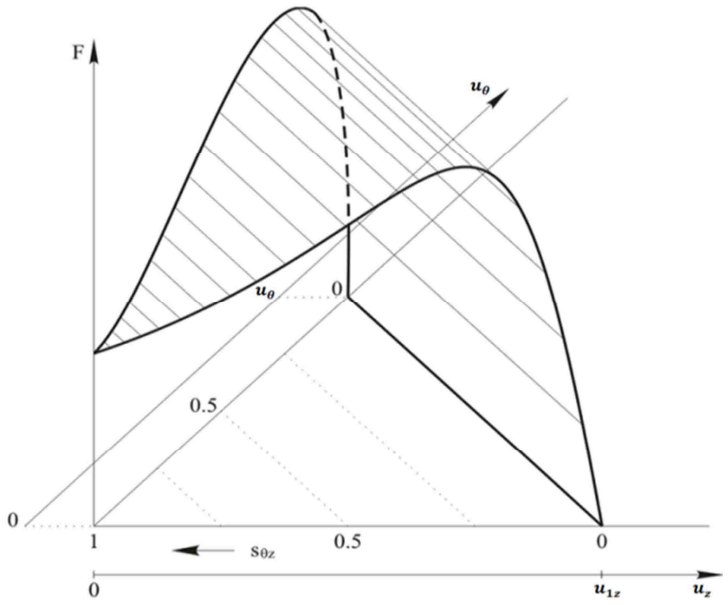

Fig 2-8. Electromechanical characteristic of the induction motor with rotating-travelling field [1].

In order to determine the operating point of the machine set, let the rotor be loaded by two machines acting independently on linear (axial) and rotational directions with the load force characteristics shown in Fig. 2-9.

The equilibrium of the machine set takes place when the resultant load force is equal in its absolute value and opposite to the force developed by the motor. The direction of the electromagnetic force F of the motor is constant and does not depend on the load. Thus, at steady state operation both load forces $F_{l\theta}$ and F_{lz} acts against motor force components F_θ and F_z in the same direction if the following relation between them takes place

$$\frac{F_\theta}{F_z} = \frac{F_{l\theta}}{F_{lz}} = ctg\alpha = \frac{\tau_z}{\tau_\theta} \tag{2-17}$$

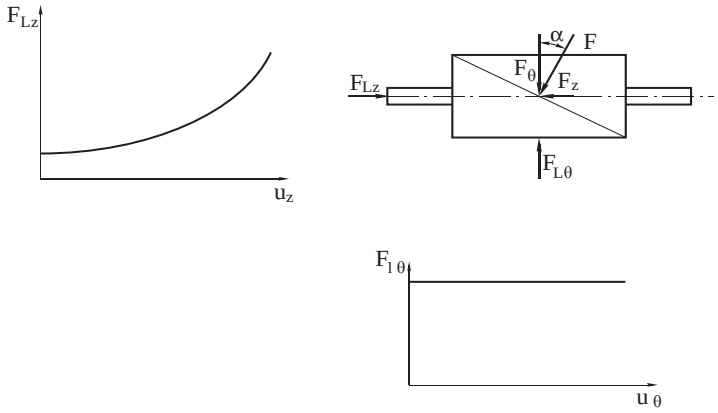

Fig 2-9. Load characteristics for IM-2DoMF, F_{lz}: load force in axial direction, $F_{L\theta}$: load force in rotary direction. [1].

To draw both load characteristics on a common graph, the real load forces $F_{l\theta}$ and F_{lz} acting separately on rotational and linear directions should be transformed into $F'_{l\theta}$ and F'_{lz}, forces acting on the direction of the motor force F. These equivalent forces are:

$$F_{l\theta}^{'} = \frac{F_{l\theta}}{\cos\alpha}, \quad F_{lz}^{'} = \frac{F_{lz}}{\sin\alpha} \tag{2-18}$$

The transformed load characteristics drawn as a function of u_θ and u_z, as shown in Fig. 2-10, are the surfaces intersecting one another along the line segment $\overline{KA}$. This line segment that forms the $F_l(u)$ characteristic is a set of points where the following equation is fulfilled

$$F_{l\theta}^{'} = F_{lz}^{'} \tag{2-19}$$

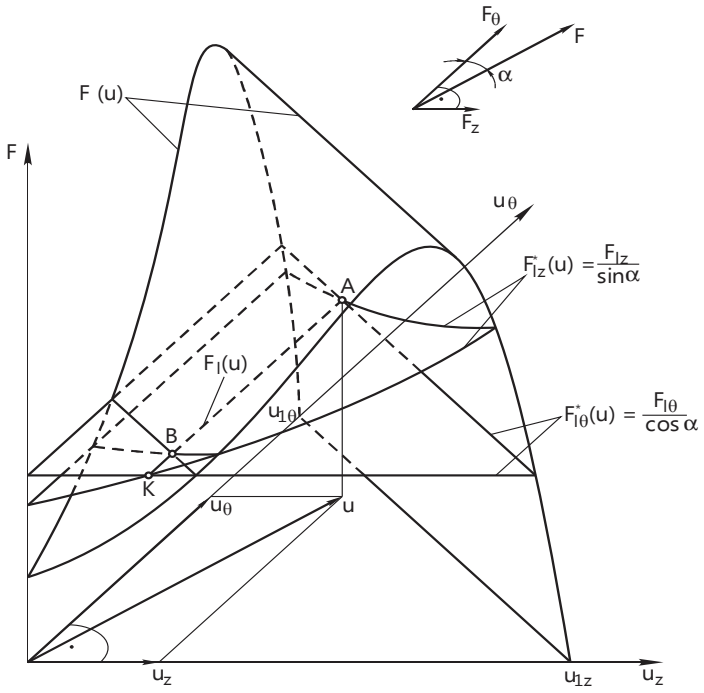

Fig 2-10. Determination of the operating point A of the machine set with IM-2DoMF [1].

The load characteristic $F_l(_u)$ intersects with the motor characteristic at points A and B, where the equilibrium of the whole machine set takes place. To check if the two points are stable

the steady state stability criterion can be used, which is applied to rotary motors in the following form:

$$\frac{dF}{du} < \frac{dF_l(u_\theta, u_z)}{du} \tag{2-20}$$

$$\frac{dF_{l\theta}}{du_\theta} > 0\,, \quad \frac{dF_{lz}}{du_z} > 0 \tag{2-21}$$

Applying this criterion, point A in Fig. 2-10 is stable and point B is unstable.

2.2.4 Conversion of Mathematical Model of IM-2DoMF to 1DoMF

The mathematical model of IM-2DoMF presented in previous subsections is more general than the one for linear or rotating machines. The rotating magnetic field wave of rotating machines and the traveling field of linear motors are in the mathematical description special cases of the rotating – traveling field. If the wave length remains steady, pole pitches along both axis (τ_θ, τ_z) will vary by changing the motion direction of field waves. For example: if the wave front (see Fig. 2-2) turns to θ axis then $\tau_z = \infty$. This makes the formula (2-1) changes to:

$$B(t, \theta) = B_m \exp\left[j\left(\omega t - \frac{\pi}{\tau_\theta}\theta \right) \right] \tag{2-22}$$

which is the flux density function for rotary motor. The $\alpha = 0$ and according to Eqn (2-2) the force $F = F_\theta$ what is the case for rotary motors. On the other hand, turning the wave completely toward z axis leads to infinity pole pitch value along θ axis ($\tau_\theta = \infty$). By inserting this into Eqn (2-1) and (2-10) the description of both field and slip expressed by two space coordinates turns to the description of such quantities in linear motors.

In other word, the mathematical model of the rotary-linear motor has a general form of two mechanical degree of freedom motor and can be reduced at any time to the model either of rotary or linear motors, motors with single degree of mechanical freedom.

CHAPTER 3 : EDGE EFFECTS IN ROTARY-LINEAR INDUCTION MOTORS – QUALITATIVE EXAMINATION

The twin-armature rotary-linear induction motor, which is the object of this chapter consists of two armatures what makes this machine a combination of two motors: rotary and tubular linear, whose rotor are coupled together. This implies that the phenomena that take place in each set of one-degree of mechanical freedom motors also occur in the twin-armature rotary-linear motor in perhaps more sophisticated form due to the complex motion of the rotor. One of these phenomena is called end effects and occurs due to finite length of the stator at rotor axial motion. This phenomenon is not present in conventional rotating induction machines, but play significant role in linear motors.

The end effects are the object of study of many papers [6, 7, 8, 9, 10, 11, 12]. In the literature, end effects are taken into account in various ways. In the circuit theory a particular parameter can be separated from the rest of the equivalent circuit elements. This approach has been done in [13, 14, 15, 16, 17]. Kwon et al. solved a LIM with the help of the FEM, and they suggested a thrust correction coefficient to model the end effects [18]. Fujii and Harada in [19] modeled a rotating magnet at the entering end of the LIM as a compensator and reported that this reduced end effect and thrust was the same as a LIM having no end effects. They used FEM in their calculations. Another application of FEM in analyzing LIMs is reported in [20]. A d-q axis equivalent model for dynamic simulation purposes is obtained by using nonlinear transient finite element analysis.

The end effect has been also included in the analysis of rotary linear motors in [1, 21, 22]. This inclusion was done by applying Fourier's harmonic method when solving the Maxwell's

equations that describe motor mathematically [1]. This approach was also applied to study the linear motor end effects [11, 12].

The edge effects phenomena caused by finite length of both armatures can be classified into two categories as follows:

- End effects: which occurs in the tubular linear part of the motor and partially in the rotary part.
- Transverse edge effects: which exists in the rotary part.

3.1 End Effects

One obvious difference between LIM and conventional rotary machines is the fact that in LIM the magnetic traveling field occurs at one end and disappears at another. This generates the phenomena called end effects. End effects can be categorized into two smaller groups called: static end effects and dynamic end effects.

3.1.1 Static End Effects

This is the phenomenon which refers to the generation of alternating magnetic field in addition to the magnetic traveling field component. The process of generation of alternating magnetic field at different instances is shown in Fig. 3-1.

Instant $t_1 = 0$ sec: The 3-phase currents are of the values shown by phasor diagram in Fig. 3-1 (b-c) with maximum in phase A. The current distribution in the primary winding relevant to these values is shown in Fig. 3-1 (a) and its first space harmonic is represented by curve J in Fig. 3-1 (b). The distribution of magneto-motive force F_m in the air-gap corresponding to this linear

current density has the cosine form with the maximum value at both edges of the primary part shown in Fig. 3-1 (b). This mmf generates the magnetic flux which consists of two components: alternating flux Φ_a shown in Fig. 3-1 (a) and traveling flux component. The distribution of these two components B_a and B_t as well as the resultant flux density $B_a + B_t$ are shown in Fig. 3-1 (c).

Instant t_2 = ¼ T sec (where T is sine wave period): The 3-phase currents are of value shown by phasor diagram in Fig. 3-1 (d) with zero in phase A. These currents make the distribution of the first harmonic of mmf F_m as shown in Fig. 3-1 (d). Since there is no mmf at primary edges, the alternating flux component Φ_a does not occur and the traveling flux B_t is the only available component.

Instant t_3 = ½ T sec: After a half period, the currents are of values shown by phasor diagram in Fig. 3-1 (e) with the maximum negative value in phase A. The relevant mmf distribution reveals its maximum negative value at primary edges which generates the magnetic flux Φ_a represented by its flux density B_a (see Fig. 3-1 (e)), which adds to the traveling flux component B_t.

Analyzing the above phenomenon in time, one may find that magnetic flux density has two components: B_a which does not move in space but changes periodically in time called alternating component and B_t which changes in time and space and is called traveling component. The first component B_a does not exist in motors with infinity long primary part which is the case in conventional rotary machines.

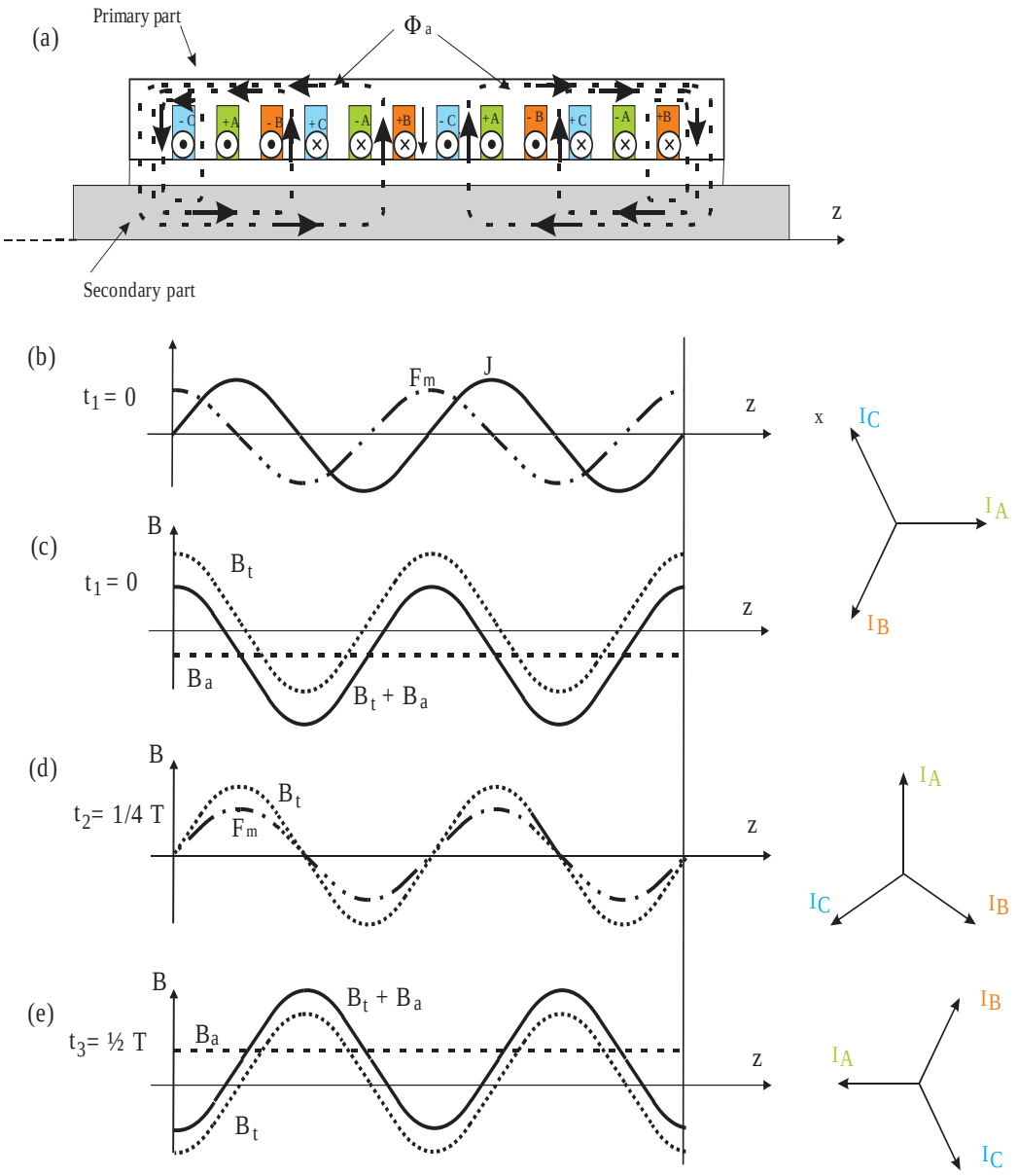

Fig 3-1. The process of generation of alternating magnetic field at different instances in 4-pole tubular motor: (Φ_a) – alternating component of magnetic flux (B_a) – alternating component of magnetic flux density in the air-gap (B_t) - travelling component of magnetic flux density in the air-gap (J) – linear current density of the primary part (F_m) – magneto-motive force of primary part in the air-gap.

Summarizing, the resultant magnetic flux density distribution is a combination of the traveling wave component $B_t(t)$ and alternating magnetic field $B_a(t)$ denoted by:

$$B(t,z) = B_t \cos\left(\omega t - \frac{\pi}{\tau_p} z + \delta_m\right) + B_a \sin\left(\omega t - \frac{\pi}{\tau_p} + \delta_a\right) \quad (3\text{-}1)$$

where τ_p is pole pitch

When only the travelling wave exists, the envelop of flux density distribution in the air gap is uniform over the entire length of the primary core but the second term deforms the air gap field distribution to the shape shown in Fig. 3-2. The alternating flux contributes to the rising of additional power losses in the secondary and to producing of braking force when one part of LIM motor is moving with respect to the other one [11], [12], [22]. This component occurs no matter what is the value of the speed of secondary part [23].

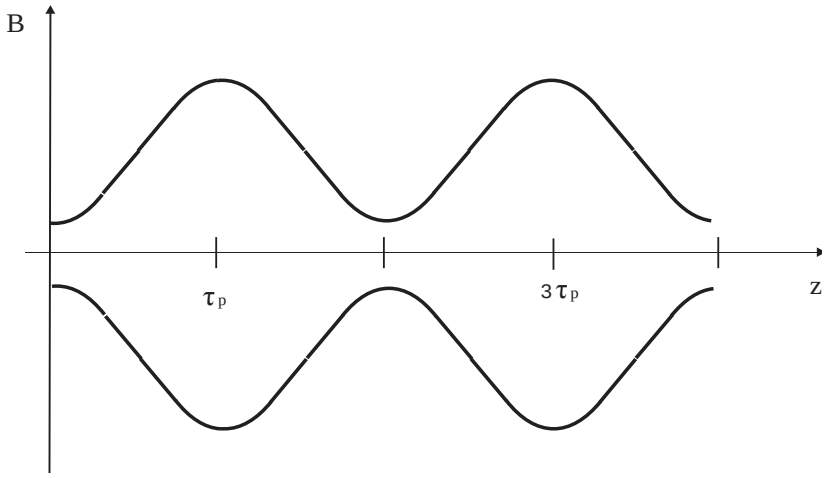

Fig 3-2. The envelope of the resultant magnetic flux density in the air-gap of four pole linear motor due to presence of the alternating magnetic field (τp - pole pitch).

3.1.2 Dynamic End Effects

The dynamic end effects are the entry and exit effects that occur when the secondary moves with respect to the primary part. This phenomenon will be explained in two stages:

Stage I: secondary part moves with synchronous speed:

There are no currents induced (within the primary part range) due to traveling magnetic field component (since the secondary moves synchronously with travelling field). However, the observer standing on the secondary (see Fig. 3-3) feels relatively high change of magnetic flux when enters the primary part region and when leaves this region at exit edge. This change contributes to rising of the eddy currents at both the entry and exit edges. These currents damp the magnetic field in the air-gap at entry in order to keep zero flux linkage for the secondary circuit. At the exit edge the secondary eddy currents tries to sustain the magnetic flux linkage outside the primary zone the same as it was before the exit. This leads to damping magnetic flux at the entry edge and to appearance of magnetic flux tail beyond the exit edge (Fig. 3-4 (a)). The distribution of the primary current density (J_1) is uniform over the entire region. The envelop of the eddy currents induced in the secondary (J_2) shown in Fig. 3-4 (a) is relevant to the magnetic flux density distribution in the air-gap.

The eddy currents at the entry and exit edges attenuate due to the fact that the magnetic energy linked with these currents dissipate in the secondary resistance. Thus, the lower is the secondary resistance the more intensive is damping at entry and the longer is the tail beyond the exit.

Stage II: secondary part moves with a speed less than the synchronous speed:

The currents are induced in the secondary over the entire primary length due to slip of the secondary with respect to the travelling component of primary magnetic flux. These currents superimpose the currents that are due to the entry and exit edges. The resultant eddy current

envelop is shown schematically in Fig. 3-4 (b). The flux density distribution in the air-gap and current density in the primary windings are also shown in Fig. 3-4 (b). As it is illustrated the primary current density is uniformly distributed along the primary length only if the coils of each phase are connected in series and the symmetry of 3-phase currents is not affected by the end effects. The magnetic flux density distribution has the same shape and changes in a same pattern in both stages, but due to the rotor current reaction, stage II has a lower B. However, primary current density is higher at the stage II if the primary winding is supplied in both cases with the same voltage.

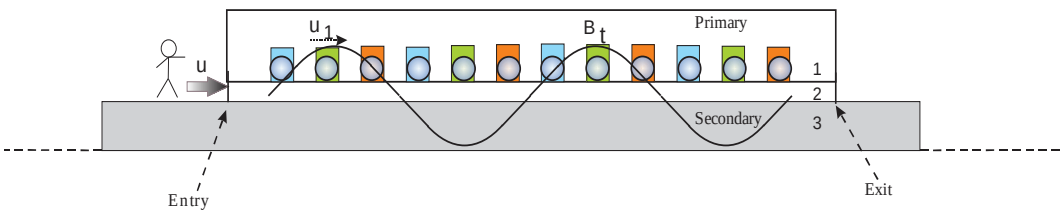

Fig 3-3. End effect explanation: (B_t) - travelling component of magnetic flux density in the air-gap (u_1) speed of traveling magnetic field (u) speed of the rotor.

In general, end effect phenomena leads to non-uniform distribution of:

- magnetic field in the air-gap,
- current in the secondary,
- driving force density,
- power loss density in the secondary.

Thus, this contributes to:

- lower driving force,

- higher power losses,
- lower motor efficiency,
- lower power factor.

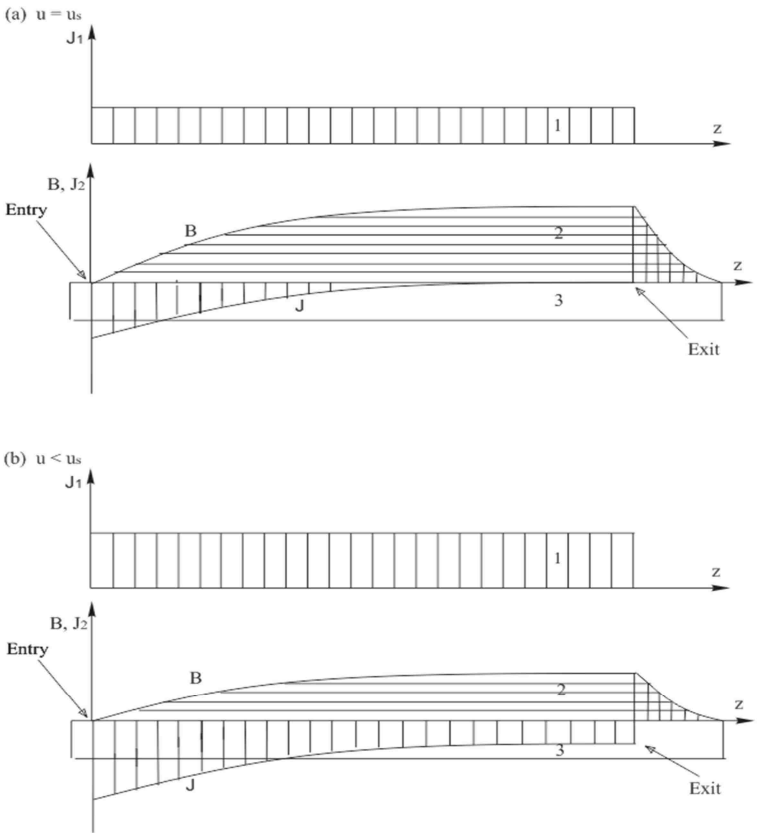

Fig 3-4. Distribution of primary current (J_1), secondary current (J2) and magnetic flux density in the air-gap (B): (a) u =us (b) u < u_s.

Due to dynamic end effects, the resultant magnetic flux density in the air-gap can be expressed as a summation of three flux density components as follows [7]:

$$B(t,z) = B_t \cos\left(\omega t - \frac{\pi}{\tau_p} z + \delta_m\right) + B_1 e^{-z/\alpha_1} \cos\left(\omega t - \frac{\pi}{\tau_{pe}} z + \delta_1\right) + B_2 e^{+z/\alpha_2} \cos\left(\omega t + \frac{\pi}{\tau_{pe}} z + \delta_2\right) \quad (3\text{-}2)$$

All the three terms of this equation have the same frequency. The first term is the traveling wave moving forward at synchronous speed. The second term is an attenuating traveling wave generated at the entry end, which travels in the positive direction of z and whose attenuation constant is $1/\alpha_1$ and its half-wave length is τ_{pe}. The third term of Eqn (3-2) is an attenuating traveling wave generated at the exit end, which travels in the negative direction and whose attenuation constant is $1/\alpha_2$ and half-wave length is τ_{pe}. The B_1 wave is caused by the core discontinuity at the entry end and the B_2 wave is caused by the core discontinuity at the exit end, hence, both are called end effect waves. Both waves have an angular frequency ω, which is the same as that of power supply. They have the same half wave-length, which is different from half-wave length (equal to pole pitch) of the primary winding. The traveling speed of the end waves is given by $v_e = 2 f \tau_{pe}$ and is the same as the secondary part if high speed motors is studied. However, in low speed motors, the speed of the end waves can be much higher than that of secondary [6]. The length of penetration of entry end wave α_1 depends on motor parameters such as gap length and secondary surface resistivity. The impact of these parameters on α_1 are quite different at high speed motors and low speed motors. As a result, α_1 is much longer at high speed motors with respect to low speed motors. Also, in the high-speed motors, half wave length τ_{pe} is almost linearly proportional to the speed of secondary and is independent from gap length and secondary surface resistivity while it is dependent to such parameters at low speed motors. Therefore, the speed of the end waves is equal to the secondary speed at high speed motors

regardless the value of parameters such as supply frequency, gap length and surface resistivity, while in low speed motors, end waves speed depends on such parameters and may reach to even higher than synchronous speed at low slip operational region. The super-synchronous speed of the end-effect wave at motor speed lower and close to synchronous speed occurs only in low speed motors [6].

The entry-end-effect wave decays relatively slower than the exit-end-effect wave and unlike exit-end-effect wave, is present along the entire longitudinal length of the air-gap and degrades the performance of the high speed motor. The exit-end-effect wave attenuates much faster due to the lack of primary core beyond the exit edge. Therefore, the influence of the exit field component B_2 on motor performance is less than that of the entry component B_1, and it may be disregarded for many applications [7,14, 15].

For the motors with the number of magnetic pole pairs greater than two if the synchronous speed is below 10 m/s the end effects can be ignored. For the motors with higher synchronous speeds the influence of end effects can be seen even for the motors with higher number of pole-pairs [24].

3.2 Transverse Edge Effects

The transverse edge effect is generally described as the effect of finite width of the flat linear motor and is the result of z component of eddy current flowing in the solid plate secondary (Fig. 3-5 (b)).

Since, there are no designated paths for the currents, as it is in cage rotors of rotary motors, the currents within the primary area are flowing in a circular mode (Fig. 3-5 (b)). These

currents generate their own magnetic field, B_r, whose distribution is shown schematically in Fig. 3-6.

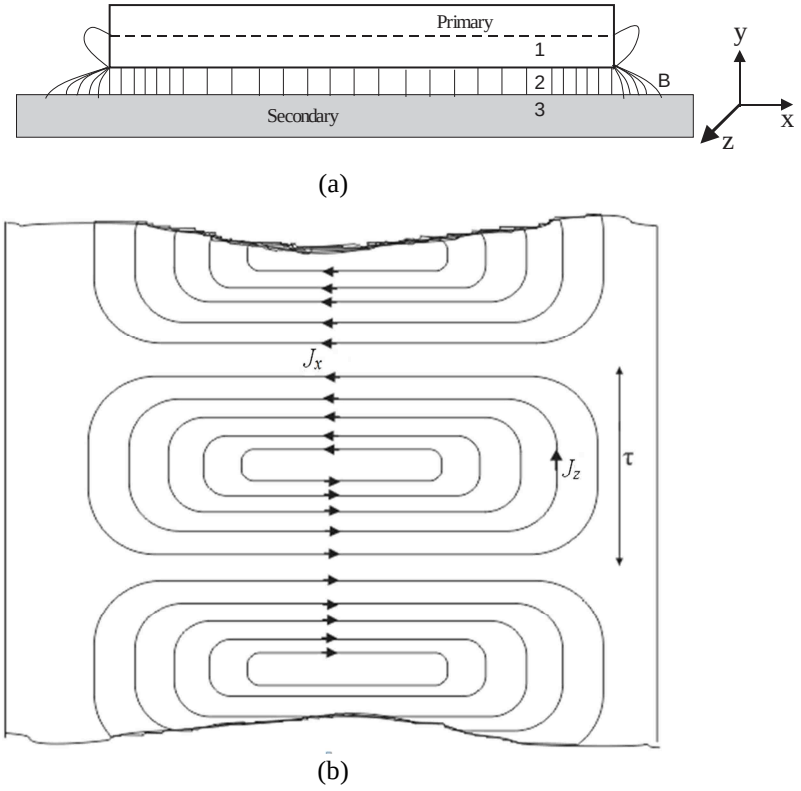

Fig 3-5. Transverse edge effect explanation: (a) The resultant magnetic flux distribution, (b) eddy current induced in the secondary.

This magnetic field subtracts from the magnetic field B_s generated by the primary part winding. The resultant field has non-uniform distribution in transverse direction (x axis) (Fig. 3-7). This non-uniform distribution of the magnetic field and circular pattern of the secondary currents contribute to the increase of power losses, decrease of motor efficiency and reduction of maximum electromagnetic force [25].

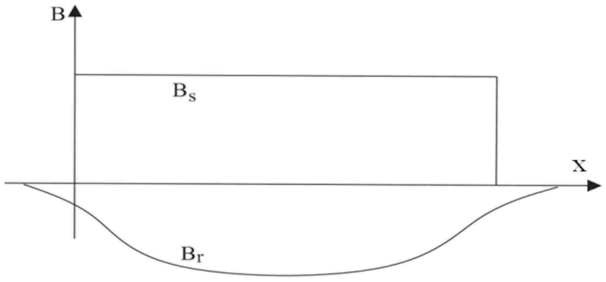

Fig 3-6. The distribution of magnetic flux density B_s produced by the primary current and B_r by the secondary currents [24].

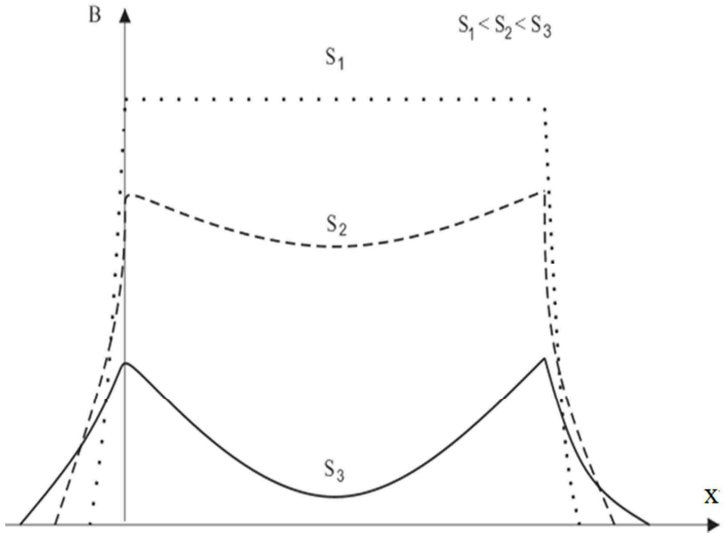

Fig 3-7. The resultant magnetic flux density distribution in the air-gap at different secondary slips [24].

As the rotary-linear motor is concerned, the transverse edge effect occurs for rotary armature. This effect has here more complex form due to the additional axial motion of the rotor. The above transverse edge effects superimpose on entry and exit effects whose nature is the same as discussed earlier for linear part of the rotary-linear motor. This motion makes the flux density distribution distorted as shown in Fig 3-8. At the entry edge the flux density in the air-gap is damped, but at the exit edge it increases.

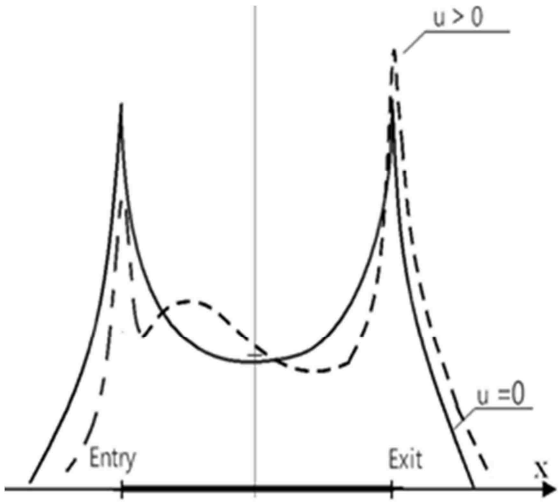

Fig 3-8. Resultant magnetic flux density in the air-gap of rotary part of the IM-2DoMF motor with linear speed greater than zero (u > 0) [24].

CHAPTER 4 : DESCRIPTION OF SOFTWARE USED IN MOTOR MODELING

Finite Element Method (FEM) is a numerical technique for solving problems with complicated geometries, loadings, and material properties where analytical solutions cannot be obtained. The basic concept is to model a body or structure by dividing it into smaller elements called ”Finite Elements”, interconnected at points common to two or more elements (nodes). The properties of the elements are formulated as equilibrium equations. The equations for the entire body are then obtained by combining the equilibrium equation of each element such that continuity is ensured at each node. The necessary boundary conditions are then imposed and the equations of equilibrium are then solved to obtain the required 3 variables.

The term finite element was first devised and used in 1960 by R.W.Clough [26]. After being developed and experimented with various applications for half a century, the finite element method has become a powerful tool for solving a wide range of engineering problems. Finite element methods for the analysis of electric machines were formulated in a series of papers in the early 1970’s by Peter P. Silvester et al.[27, 28, 29]. Much of the initial work in electromagnetic finite elements began with the analysis of synchronous machines. Nowadays finite-element-based CAD systems to solve two-dimensional field problems are in common use. However, they are far from perfect, and there are still many unsolved problems and limitations on application, making finite element analysis of electric machine still a very active research topic. Further developments of the finite element method lead to various directions according to applications. Examples include analysis of different types of machines [30, 31], incorporating external circuits to problem formulations with imposed voltage sources [32, 33, 34], coupling electromagnetic analysis with other physics [35], incorporating saturation effects [36], hysteresis effects [37] and

material anisotropy [38], etc. Among the various research directions, improvement of the computational efficiency of the FEM solver is one important branch.

The behavior of a phenomenon in a system depends upon the geometry or domain of the system, the property of the material or medium, and the boundary, initial and loading conditions.

The procedure of computational modeling using FEM broadly consists of four steps:

- Modeling of the geometry
- Meshing (discretization)
- Specification of material property
- Specification of boundary, initial and loading conditions

Modeling of the geometry: Real structures, components or domains are in general very complex, and have to be reduced to a manageable geometry. Curved parts of the geometry and its boundary can be modeled using curves and curved surfaces. However, it should be noted that the geometry is eventually represented by piecewise straight lines of flat surfaces, if linear elements are used. The accuracy of representation of the curved parts is controlled by the number of elements used. It is obvious that with more elements, the representation of the curved parts by straight edges would be smoother and more accurate. Unfortunately, the more elements, the longer is the computational time that is required. Hence, due to the constraints on computational hardware and software, it is always necessary to limit the number of elements.

Meshing: Meshing is performed to descretize the geometry created into small pieces called elements or cells. The solution for an engineering problem can be very complex and if the problem domain is divided (meshed) into small elements or cells using a set of grids or nodes,

the solution within an element can be approximated very easily using simple functions such as polynomials. Thus, the solutions for all of the elements form the solution of the whole problem domain. Mesh generation is a very important task of the pre-process. It can be a very time consuming task to the analyst, and usually an experienced analyst will produce a more credible mesh for a complex problem. The domains have to be meshed properly into elements of specific shapes such as triangles and quadrilaterals.

Property of material or medium**:** Many engineering systems consist of more than one material. Property of materials can be defined either for a group of elements or each individual element, if needed. For different phenomena to be simulated, different sets of material properties are required. For, example, Youg's modulus and shear modulus are required for the stress analysis of solids and structures whereas the thermal conductivity coefficient will be required for a thermal analysis. Input of material's properties into a pre-processor is usually straightforward. All the analyst needs to do is select material properties and specify either to which region of the geometry or which elements the data applies.

Boundary, initial and loading conditions**:** Boundary, initial and loading conditions play a decisive role on solving the simulation. To input these conditions is usually done using commercial pre-processor, and it is often interfaced with graphics. Users can specify these conditions either to the geometrical identities (points, lines or curves, surfaces, and volumes) or to the elements or grid.

There are many commercially used FEM programs. In this dissertation the FEM is used to solve both time harmonic magnetic problems (eddy current, transient) and time-invariant field problems (magneto-static). The 2-dimensional models are created and optimized using FEMM

4.2 [39]. The 3-dimensional models are then created in Maxwell v13 from Ansoft [40] to perform magneto-static and parametric analysis and time harmonic magnetic field problems.

4.1 2-D Fem Modeling: FEMM 4.2 Program

FEMM 4.2 is a suite of programs for solving low frequency electromagnetic problems of two-dimensional planar and axisymmetric domains. The program currently addresses linear/nonlinear magneto-static problems, linear/nonlinear time harmonic magnetic problems, linear electrostatic problems, and steady-state heat flow problems.

FEMM is divided into three parts [39]:

Interactive shell (femm.exe): This program is a Multiple Document Interface pre-processor and a post-processor for the various types of problems solved by FEMM. It contains a CAD like interface for laying out the geometry of the problem to be solved and for defining material properties and boundary conditions. Autocad DXF files can be imported to facilitate the analysis of existing geometries. Field solutions can be displayed in the form of contour and density plots. The program also allows the user to inspect the field at arbitrary points, as well as evaluate a number of different integrals and plot various quantities of interest along user-defined contours.

triangle.exe: Triangle breaks down the solution region into a large number of triangles, a vital part of the finite element process.

There are following Solvers:

- fkern.exe - for magnetics;

- belasolv - for electrostatics;
- hsolv - for heat flow problems;
- csolv - for current flow problems.

Each solver takes a set of data files that describe problem and solves the relevant partial differential equations to obtain values for the desired field throughout the solution domain.

The Lua scripting language is integrated into the interactive shell [39] and is used to link Matlab with FEMM.

4.2 3-D Fem Modeling MAXWELL Program

Maxwell 12v is an interactive software package that uses finite element method to solve three-dimensional (3D) electrostatic, magneto-static, eddy current and transient problems. It is used to compute:

- Static electric fields, forces, torques, and capacitances caused by voltage distributions and charges.
- Static magnetic fields, forces, torques, and inductances caused by DC currents, static external magnetic fields, and permanent magnets.
- Time-varying magnetic fields, forces, torques, and impedances caused by AC currents and oscillating external magnetic fields.
- Transient magnetic fields caused by electrical sources and permanent magnets [40].

4.3 Dynamic Simulation (Mechanical Movement)

The electrical machine is one of the many electrical devices which include parts that can move relative to others. To enable the dynamic behavior to be modeled, or to take into account the losses and forces (e.g. ripple torque) arising from mmf and permeance harmonics, movement must be incorporated in the Finite Element model for machine analysis. Dealing with movement in the FEM is problematic because of the air-gap. The air-gap of electric machines presents several difficulties for the FEM. First, since the air-gap is usually very thin, it is difficult to fit an adequate number of finite elements into it to model the important field interactions taking place there. Moreover, movement of the rotor will eventually destroy the integrity of the mesh in the air-gap, which can lead to inaccuracy in the field solution. The simplest way of dealing with movement is to move the rotor and remesh the problem. The obvious drawback of this method is the time and memory required for remeshing.

Several different approaches are described in the literature. They have their own advantages and disadvantages. The existing movement models can be divided into two categories: those, which construct a special ”band” in the air-gap, and those which model the air-gap region with techniques that more conveniently deal with relative motion.

Meshes are divided into two parts: the fixed part associated with the stator and the moving part associated with the rotor. The moving and stationary meshes are solved in their own inertial frames and are coupled through the elements on their interface. These methods are described and evaluated as follows.

4.3.1 Air-Gap Re-Meshing

To take into account the physical motion of the rotor when performing dynamic analysis,Yasuharu et al [41] combines the rotor movement equation with the fundamental equation of the 2-D finite element analysis. With the movement of the rotor provided, when large motion occurs, the nodal connection between rotor and stator are changed. i.e., the air-gap region is re-meshed. This method is sometimes also called 'moving band technique' [42, 43, 44] and is used very often. Fig. 4-1 shows the re-meshing of elements in the air-gap. The disadvantage of this method is the potential of mesh quality problems as elements with large aspect ratios can be produced. If the structure of the machine is complex this method becomes cumbersome and very expensive. Also, as connections are broken and remade, there can be a sudden transition in the sizes of the matrix coefficients and discontinuity of stiffness matrix as a function of rotor position. To avoid the later shortcoming Demenko [45] proposes a modification by the trigonometric interpolation of the band matrix, thus guaranteeing the continuity of stiffness matrix and its derivation as a function of rotor position.

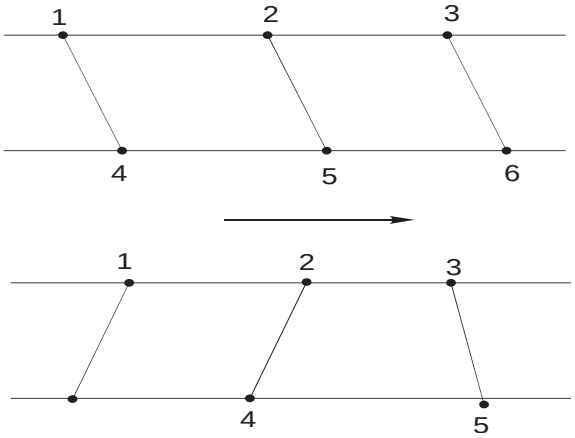

Fig 4-1. Illustration of air-gap re-meshing technique.

4.3.2 Time-Stepping Technique

The time-stepping method [46] creates a moving surface in the air-gap between stator and rotor (the slip surface). The surface is subdivided into a number of equal intervals whose length corresponds to the length of the time step so that as the rotor moves, nodes on the moving surface always coincide peripherally. It's easy to implement if the speed is constant. It is also suitable for the computation of forces [47]. The advantage of this method is that the moving problem need only be meshed once; the program can then take care of any rotations or shifts of mesh. The disadvantage is that the time step is fixed by the time taken to move from one mesh alignment to the next.

4.3.3 Sliding Interface Technique

Similar to the time-stepping technique, the sliding interface technique also uses a moving interface in the air-gap. Instead of requiring the mesh size to correspond to the time step, the nodes on the interface need not be coincident (Fig. 4-2) [48]. In Fig. 4-2, the rotor variable A_{rk} can be coupled to the variables in an adjacent stator element s by applying a constraint:

$$A_{rk} = \sum_{i=1}^{4} A_{si}\, N_{si}(k) \tag{4-1}$$

where $N_{si}(k)$ is the shape function evaluated at point k. All similar constraints on the sliding interface can be written as:

$$A_r - f(A_s) = 0 \tag{4-2}$$

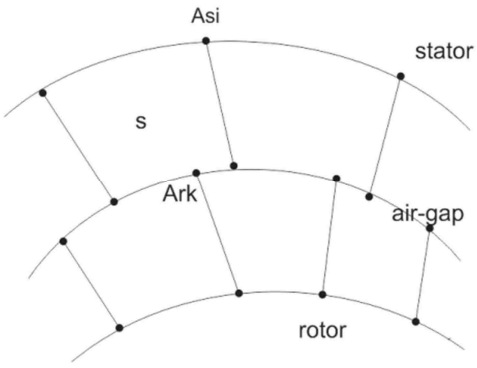

Fig 4-2. Illustration of sliding interface technique [48].

The constraint (4-2) is then enforced in the finite element equations by introducing a new set of variables, the Lagrange multipliers, which exist only on the sliding interface. Continuity of the normal flux density from rotor to stator is assured by the continuity of the constrained variables on the interface.

The advantage of this method, as stated before, is that irregular meshes and even different numbers of nodes and elements on both sides of the Lagrange surface are possible. The disadvantage being that the method is not simple and the matrix arising from this formulation is not well conditioned.

There are other methods in the literature such as “Analytical solution for air-gap combined with FEM [49]” and “Hybrid finite element-boundary element method [50]”.

CHAPTER 5 : TWIN-ARMATURE ROTARY-LINEAR INDUCTION MOTOR WITH DOUBLE SOLID LAYER ROTOR

5.1 Design Parameter of the Motor

One of a few design versions of rotary-linear motors is a Twin-Armature Rotary-Linear Induction Motor (TARLIM) shown schematically in Fig. 5-1. The stator consists of a rotary and linear armature placed aside one another. One generates a rotating magnetic field, another traveling magnetic field. A common rotor for these two armatures is applied. It consists of a solid iron cylinder covered with a thin copper layer.

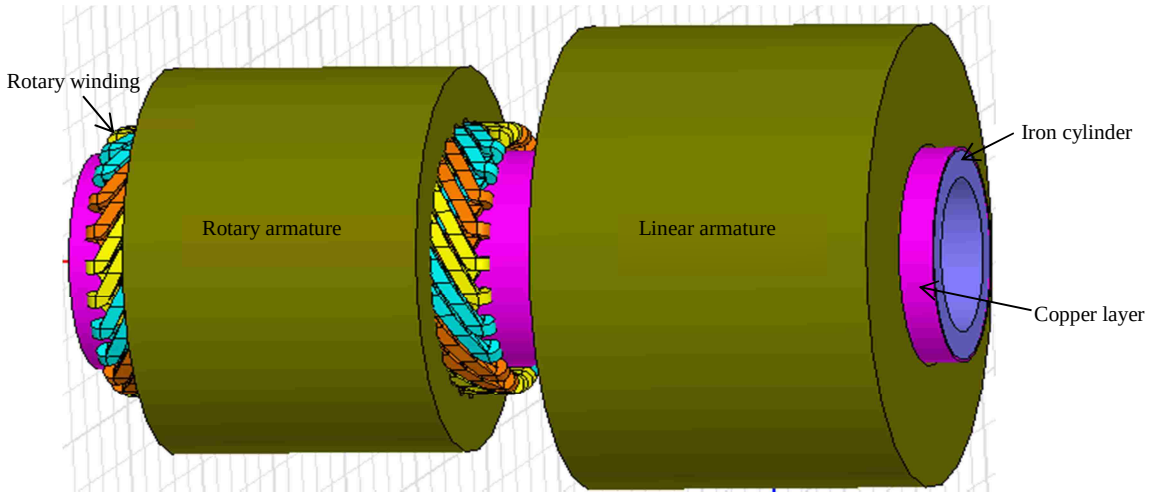

Fig 5-1. Schematic 3D-view of twin-armature rotary-linear induction motor.

The TARLIM in its operation can be regarded as a set two independent motors: a conventional rotary and tubular linear motor with the rotors joined stiffly. This approach can be applied only if there is no magnetic link between the two armatures [1], what is practically fulfilled due to the relatively long distance between the armatures and the low axial speed of the rotors. In case of the motor analyzed here both conditions are satisfied and the analysis of each

part of the TARLIM can be carried out separately as the analysis of IM 3-phase rotary and linear motors. The only influence of one motor on the other is during the linear motion of the rotor which will be considered at the end of this chapter. Both rotary and linear armatures are schematized separately in Fig. 5-2.

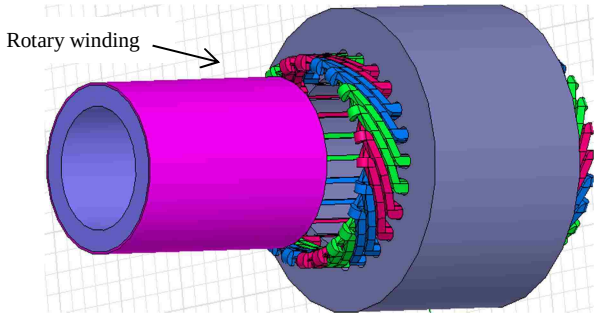

(a)

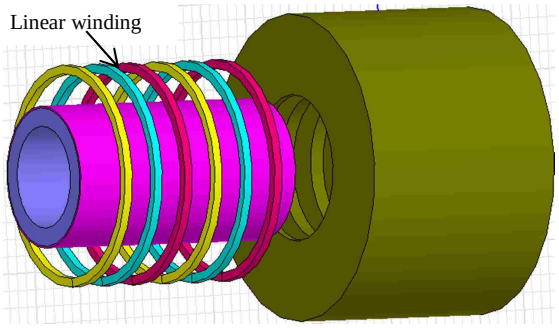

(b)

Fig 5-2. 3-D expanded view of: (a) rotary induction motor, (b) linear induction motor.

To study the performance of TARLIM the exemplary motor has been chosen with the dimensions shown in Fig. 5-3. The dimensions of rotary armature are presented in details in Fig. 5-4.

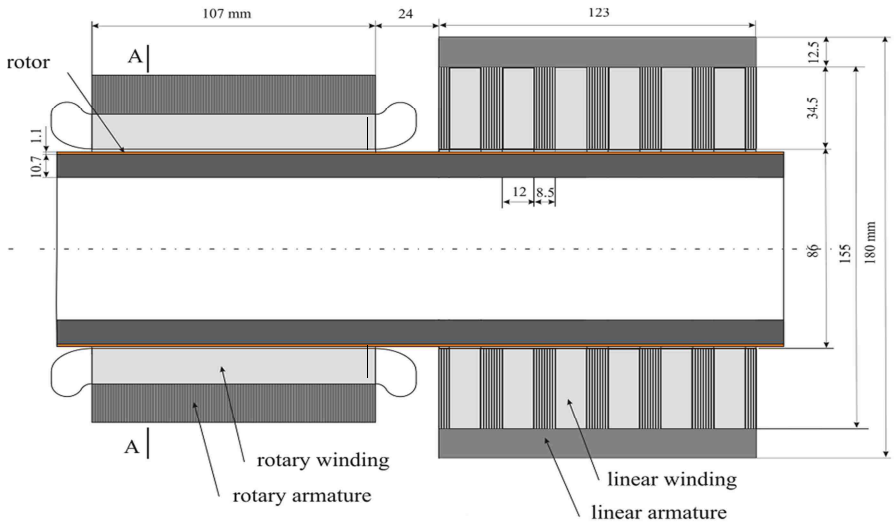

Fig 5-3. Dimensions of TARLIM chosen for analyses.

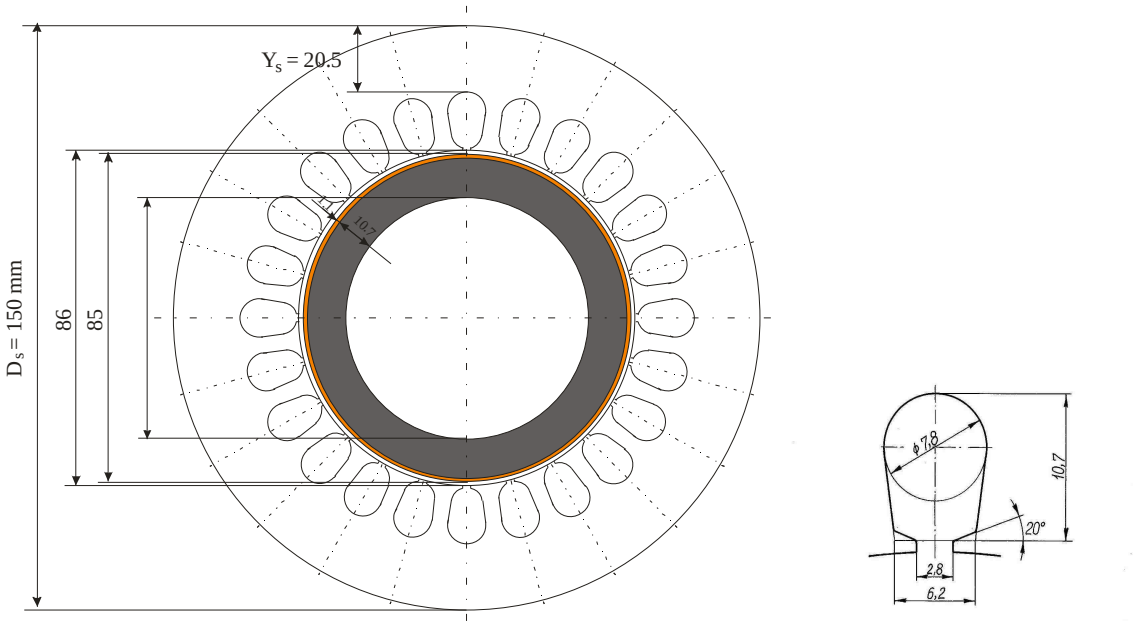

Fig 5-4. Rotary armature dimensions.

The core of both armatures is made of laminated steel. The common rotor is made of solid steel cylinder covered by copper layer. Both armatures possess a 3-phase winding. The

rotary and linear winding diagrams are shown in Fig 5-5 (a) and (b), respectively. The winding parameters and the data of stator and rotor core material are enclosed in Table 5-1.

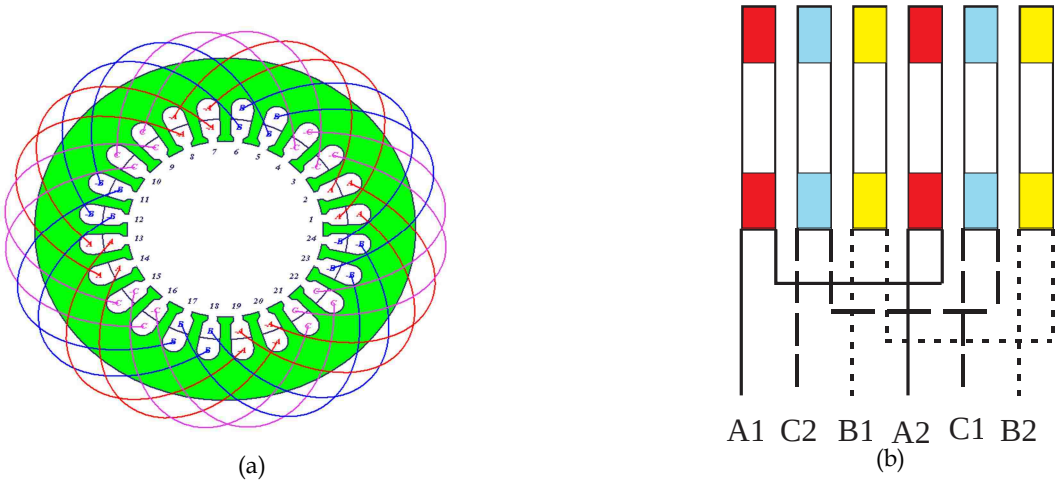

(a) (b)

Fig 5-5. Winding diagram of the TARLIM, (a) rotary winding, (b) linear winding.

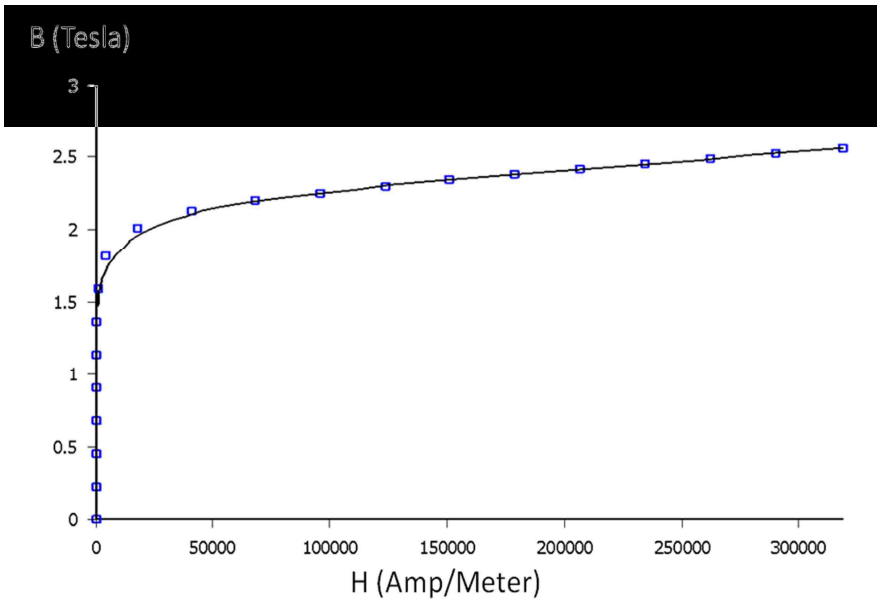

Fig 5-6. Magnetization characteristic of rotor core (iron) [39].

Table 5-1. Winding and materials data for TARLIM**.**

Linear winding data:	
Number of phases	3
Number of poles	2
Number of slots per pole per phase	1
Number of wires per slot, N_w	215
Copper wire diameter	1.29 mm
Rotary winding data:	
Number of phases	3
Number of poles	4
Number of slots per pole per phase	2
Number of wires per slot, Nw	96
Copper wire diameter	0.7 mm
Armature Core	Laminated steel
Air gap length,	0.5 mm
Rotor	
Copper layer	
Thickness mm	1.1 mm
Conductivity (γCu, @ 20C)	57.00×10^6 S/m
Solid iron cylinder	
Thickness mm	10.7 mm
Conductivity (γFe, @ 20C)	5.91×10^6 S/m
Magnetization characteristic	Fig 5-6

5.2 Linear Motor Performance

In rotating machines, end effects linked with the rotary motion do not occur, because there are no ends in the direction of motion. In linear induction motors (LIMs), due to the open magnetic circuit in the motion direction the electromotive forces induced in three phase windings

are no longer symmetric. This contributes to asymmetry of input impedance and phase primary currents in case of 3-phase windings balanced voltage-driven source. This asymmetry affects the performance of the motor under motoring and generating conditions [51].

The LIMs similar as conventional 3-phase motors are supplied, practically, from balanced voltage source. Thus, to have the end effects properly considered, the analysis of the motor performance should be done by having asymmetrical impedance taken into account. This ought to be done, in particular, in motors with two poles, where end effects are more visible.

Equivalent circuit parameters of LIM has been derived, in many papers, without considering such an effect [52, 53, 54]. Asymmetry nature of LIMs has been described analytically among others in [55]. However, to the best of author's knowledge there is no comprehensive work yet to propose a straightforward methodology for such a purpose.

Therefore, the author of this dissertation focused primarily on development of LIM equivalent circuit including asymmetry as well as other phenomena caused by end effects.

5.2.1 End Effect Modeling Using FEM

When a LIM is supplied with a constant voltage source, its performance is different from that under constant current drive. Performance under constant voltage drive is more difficult to analyze in FEM, because the primary current is not given at the beginning of performance calculations. Under constant voltage drive, the primary current changes as slip changes, while it remains the same under constant current drive.

The approach used in this section is based on the combination of the field theory and circuit theory. In the field theory the motor is modeled applying FEM and in circuit theory the

motor is represented by equivalent circuit. First, the induction motor is modeled in FEM in order to determine the parameters of the equivalent circuit. Ultimately, the characteristic of input current versus slip can then be obtained by performing some simple circuit analysis. The electric and magnetic asymmetries due to open magnetic circuit of LIM at series connection of coils windings are taken into account by the proposed method.

To study the influence of the end effects on the performance of linear induction motors, three different scenarios are considered:

No end effects are considered: To eliminate alternating magnetic field (static end effect) linked with the finite length of the primary the infinitely long motor should be considered. Practically, the infinitely long motor is modeled by increasing the number of pole pairs from 2 to 8 (Fig 5-7). The analysis of such a motor is performed using FEM through all the extended pole pairs that is 8 and then results are divided by 4 to comply with the real motor with 2 pole pairs. The field analysis is carried out in frequency domain with current driven source and the motion is modeled by slip frequency technique.

It can be assumed that, if the reference system is attached to the secondary, the fundamental magnetic field generated by the stator will move with the slip speed, what means that supplying the primary windings with the slip frequency current can simulate the secondary motion. The mover under study is an iron tube covered by a non-magnetic material (copper) layer and the magnetic flux penetration depth does not change significantly with supply frequency. Since the motion is modeled with slip frequency technique and in fact no actual transient phenomena takes place, the traveling magnetic field is not deformed by entry and exit waves and speed dependent (dynamic) end effect can also be ignored. Therefore, traveling

magnetic field generated by 3-phase winding is the only magnetic wave in the air-gap and is given by:

$$B(t,z) = B_{mt}\cos\left(\omega_s t - \frac{\pi}{\tau_p}z + \delta_m\right) \quad (5\text{-}1)$$

where Bmt - amplitude of travelling wave of magnetic flux density, ω_s - slip pulsation, τ_p – pole-pitch length, δ_m - phase angle. The slip pulsation is calculated as: $\omega_s = s\,\omega_1$ where ω_1 is a supply pulsation.

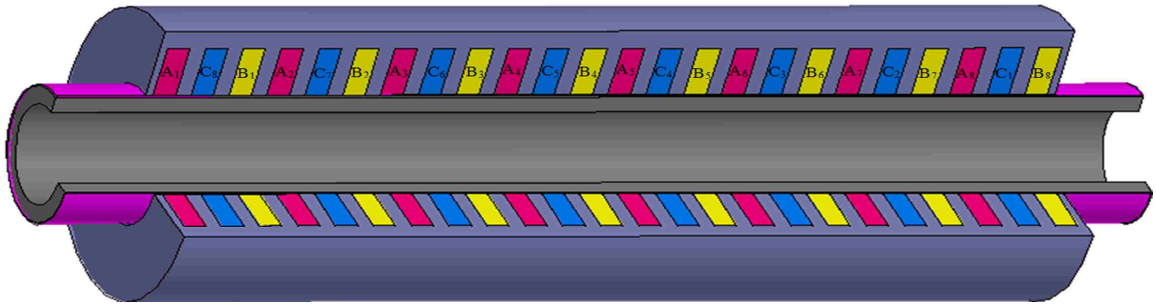

Fig 5-7. Scheme of LIM which represents the motor without end effects.

The linear armature winding is being supplied from the constant voltage source with slip frequency.

The algorithm, in which the input impedance and excitation current vs. slip are derived for a machine with two poles, is given as follows:

Step 1: Assume a rotor to be locked (slip = 1) while the stator winding is supplied with the nominal current.

Step 2: Solve the eddy current field problem for two adjacent poles of each phase (using 3-D FEM) with respect to the flux linkage λ

Step 3: Calculate the induced voltage E_i across each phase belt by multiplying total flux linkage obtained from field model by $j\omega_1$:

$$E_i = j\,\omega_1\,\lambda_i \tag{5-2}$$

where ω_1 is the source line angular frequency and i = phases a, b, c. Per phase magnetic flux linkage seen from the coil's terminal, is given by:

$$\lambda_i = N \oint \vec{B} \,.\, \overrightarrow{ds} \tag{5-3}$$

where: N is the total number of phase belt turns and S is the shaded area in the coil center shown for phase A in Fig 5-8.

In reality, the coil turns are evenly distributed throughout the whole circular area (not just shaded area) so the number of magnetic flux lines passing through (flux linked with) each turn is not necessarily the same with other turns but for simplicity all turns are assumed to be placed in the center so each turn is linked with the same flux and Eqn (5-3) can be easily solved. (Green arrows represent the flux linked with all coil turns)

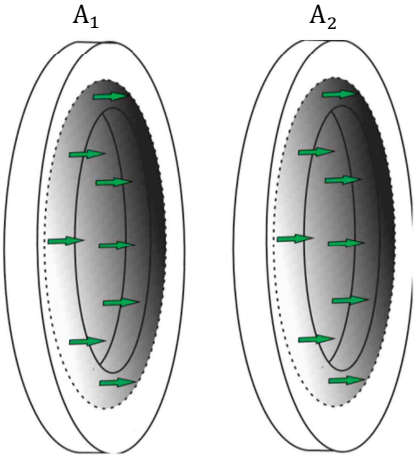

Fig 5-8. Magnetic flux (green arrows) linked with the coils of phase A (through the shaded area).

Step 4: Calculate the phase terminal voltage V_i by adding the voltage drop over primary resistance.

$$V_i = I R_1 + E_i \quad (5\text{-}4)$$

The primary resistance R1 can be obtained either from FEM analysis or directly from motor data (Appendix A)

Step 5: Calculate per phase equivalent impedance seen from the coil terminal using the following formula (Fig 5-9):

$$Z_i = \frac{V_i}{I} \quad (5\text{-}5)$$

where I is rms value of the primary phase current that was assumed in FEM model.

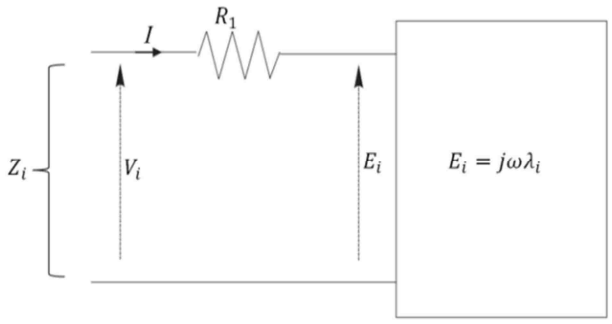

Fig 5-9. Thevenin equivalent circuit of phase winding.

Step 6: Having obtained the input impedance and assuming the rated phase voltage calculate the complex excitation current given by:

$$I_i = \frac{V}{Z_i} \quad (5\text{-}6)$$

where V is the new rms balanced phase voltage that supplies the linear armature winding

Step 7: Step 2 through 6 is then repeated for all other slips from s=0 to s=1.

With the above mentioned algorithm the calculations have been done. The results are shown in Figs. 5-10 through 5-12. Magnetic flux density distribution along the longitudinal axis in the middle of the air gap at the maximum rated phase current equal to 4.24 A at synchronous speed and locked rotor position are shown in Fig 5-10. Due to the reaction of eddy currents in the rotor layer, higher flux density is expected at synchronous speed. The envelope of flux density is still slightly deformed (apart from deformation caused by slotting), in particular at both ends, but in general this deformation may be ignored. This statement can be verified by calculating the impedance for each of all three phases.

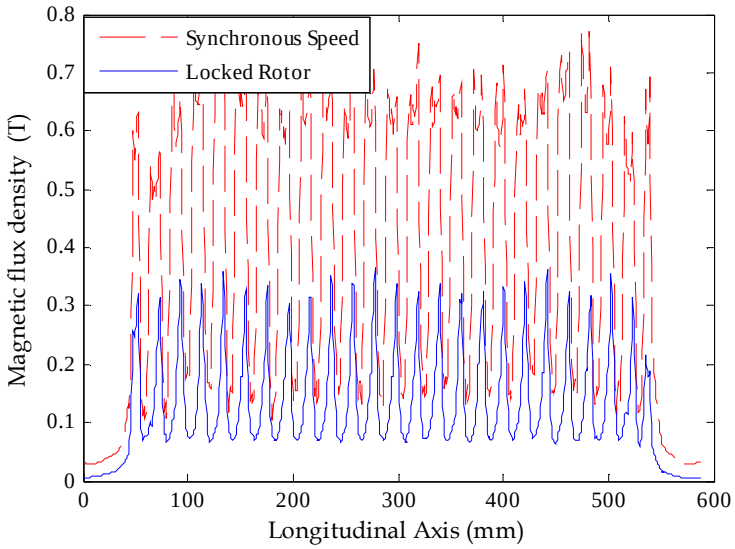

Fig 5-10. Magnetic flux density distribution in the middle of the air-gap along the longitudinal axis calculated at current of 4.24 A (maximum).

Fig 5-11 presents the impedance as an average per two magnetic poles versus slip. In case of uniform distribution of the magnetic flux in the air-gap, as it is for infinitely long motor, the

identical impedance characteristics for all three phases are expected. Since there is still some deformation caused by the finite primary length seen in Fig 5-10 the impedances of all three phases slightly differ. To minimize this difference, it is to eliminate the influence of end effects, the primary winding impedances were calculated choosing the coils A5, C4, B5, A6, C3 and B6 (see Fig 5-7). The results are shown in Fig 5-12. The differences between the impedances of all three phase are almost invisible.

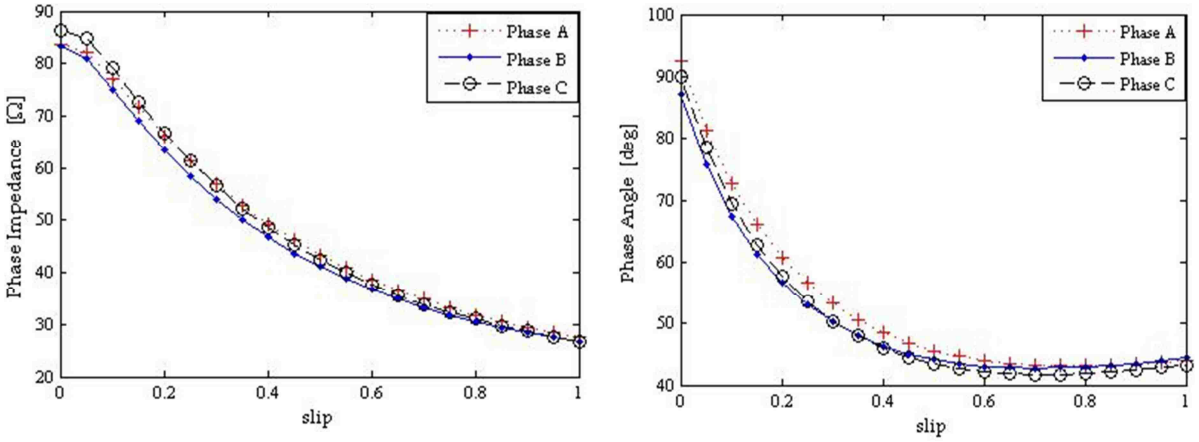

Fig 5-11. Phase impedances vs. slip characteristics calculated as an average per two magnetic poles.

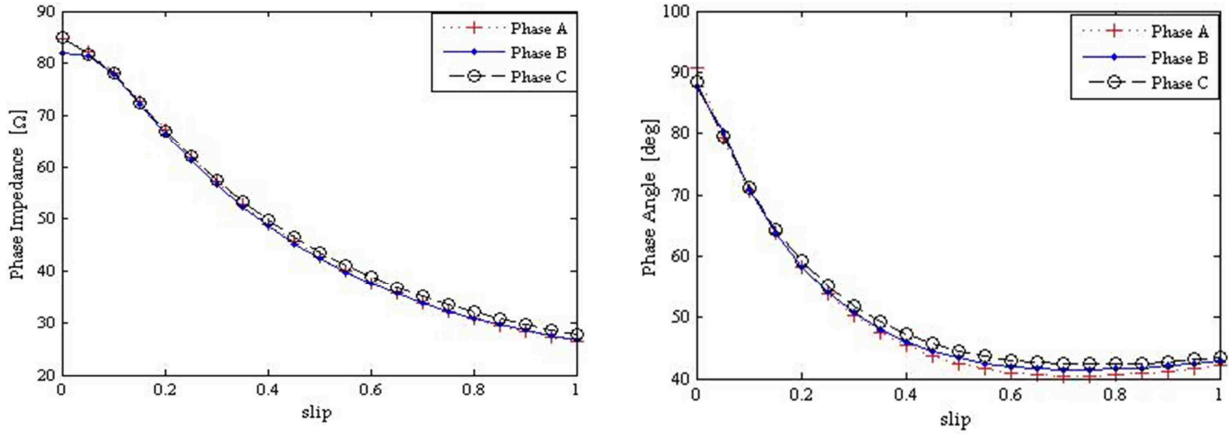

Fig 5-12. Phase impedances vs. slip calculated for the coils A_5, C_4, B_5, A_6, C_3 and B_6 (two magnetic poles) placed in the middle of armature (see Fig 5-7).

The impedance calculated in this way can be further used to calculate the currents in the case of constant voltage driven source. The currents vs. slip, calculated assuming balanced ac voltage supply are shown in Fig 5-13. From Figs 5-12 and 5-13, one can observe that input impedances and input currents are symmetrical and nearly the same for all three phases, meaning end effects are eliminated.

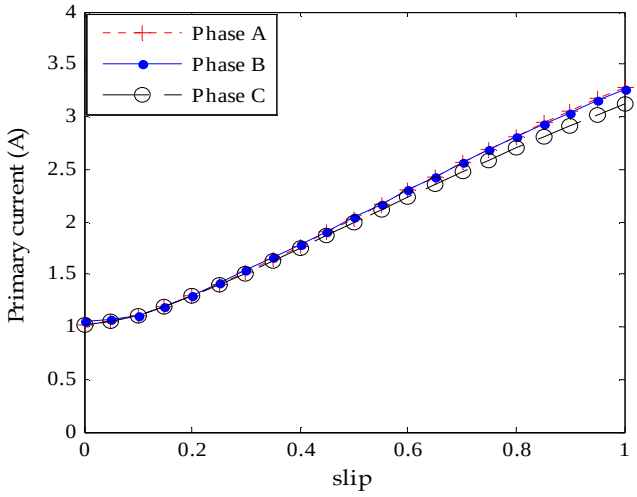

Fig 5-13. Primary (RMS) current vs. slip characteristics calculated under constant balanced supply voltage of 86.6 V rms phase voltage and 50 Hz frequency.

Static end effect: To have static end effect taken into account, finite length motor with the number of pole pairs equal to 2 is considered (Fig 5-14). The finite length of motor insures the presence of alternating magnetic field in addition to magnetic traveling field and the resultant magnetic flux density distribution is denoted by:

$$B(t,z) = B_{mt}\cos\left(\omega_s t - \frac{\pi}{\tau_p}z + \delta_m\right) + B_{ma}\sin\left(\omega_s t - \frac{\pi}{\tau_p} + \delta_a\right) \quad (5\text{-}7)$$

where B_{mt} and B_{ma} is the amplitude of traveling and alternating wave components respectively and δ_a is the phase angle. The alternating component occurs no matter what is the value of rotor linear speed [23].

To eliminate the dynamic end effects from the calculations the motor winding is supplied from the current source at different slip frequencies for the relevant slip, and the motion is modelled by slip frequency technique similar as it was for infinitely long LIM.

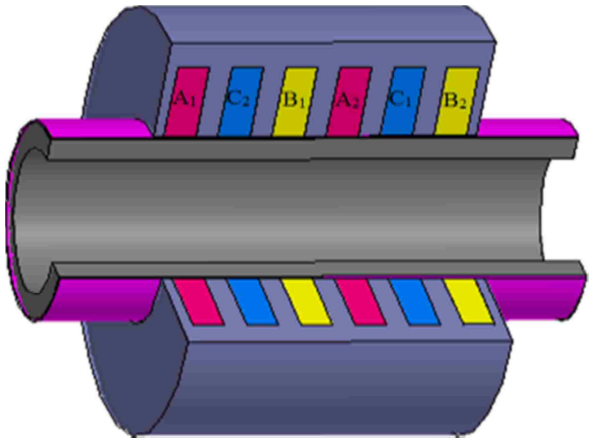

Fig 5-14. LIM with finite primary length.

The flux density distribution in the middle of air gap at both synchronous speed and locked rotor position are plotted in Fig 5-15. The influence of alternating flux component (second term of Eqn. (5-7)) on the resultant flux is clearly visible by bold dot-dashed curve. It differs with the change of the slip frequency. At high slip frequency (s=1) it is almost negligible while for zero slip frequency is way more significant. The coils of phases A and B are linked nearly with the same flux at slip s = 0, while the coils of phase C are linked with higher flux. This results in appropriate differences of impedances between three phases shown in Fig. 5-16. Impedance of phase C at slip 0 is higher than impedance of other two phases. At slip equal to 1

the differences between the impedances of all 3 phases are lower because their coils are linked with nearly the same flux (see Fig. 5-15). The differences between the impedance angles are much greater, in particular in the region at lower slips.

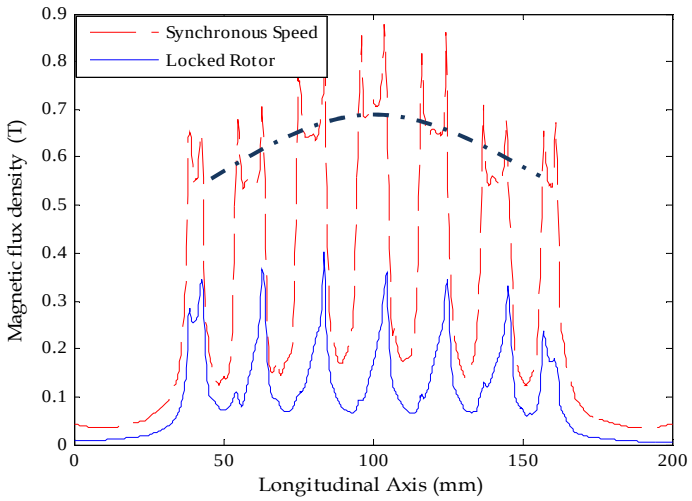

Fig 5-15. Envelop of magnetic flux in the middle of the air-gap along the longitudinal axis at constant current of 4.24 A.

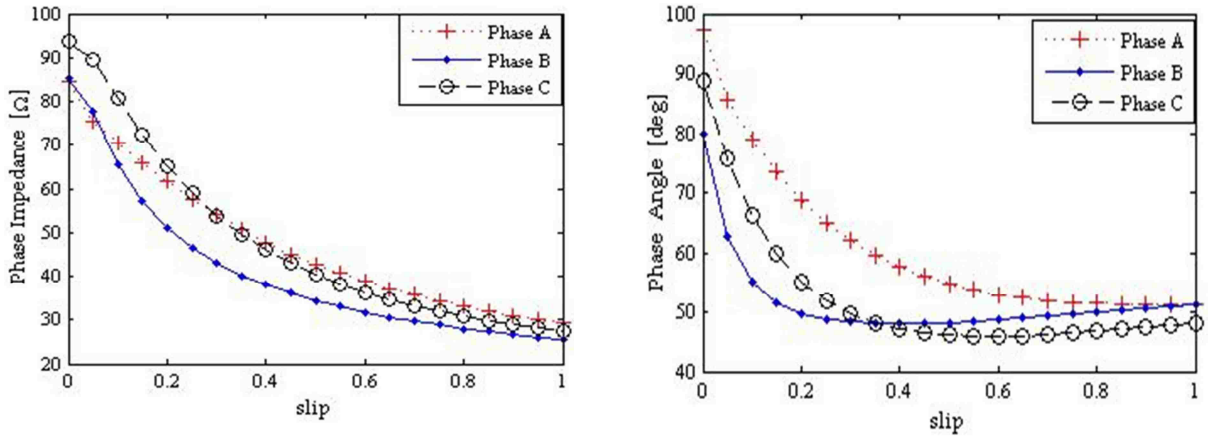

Fig 5-16. Input impedance versus slip characteristics if static end effect is taken into account.

Due to the open magnetic circuit and presence of the alternating magnetic field in the resultant flux the electromotive forces induced in three phase windings are no longer symmetric.

This makes the primary currents unbalanced when the 3-phase windings are supplied from balanced voltage source. It is illustrated in Fig 5-17 where the currents vs. slip characteristics are displayed.

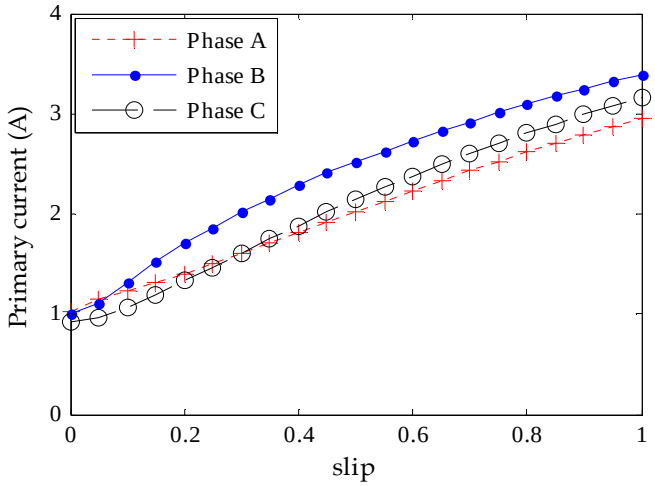

Fig 5-17. Primary (RMS) current versus slip characteristics under balanced 3-phase supply voltage of Vphase = 86.6 V rms.

Static and dynamic end effects: The dynamic end effects are the entry and exit effects that occur when the secondary moves with respect to the primary part. The resultant magnetic flux density in the air-gap can be then expressed as a summation of four flux density components as follows:

$$B(t,z) = B_t \cos\left(\omega t - \frac{\pi}{\tau_p} z + \delta_m\right) + B_a \sin\left(\omega t - \frac{\pi}{\tau_p} + \delta_a\right)$$
$$+ B_1 e^{-z/\alpha_1} \cos\left(\omega t - \frac{\pi}{\tau_{pe}} z + \delta_1\right) + B_2 e^{+z/\alpha_2} \cos\left(\omega t + \frac{\pi}{\tau_{pe}} z + \delta_2\right) \quad (5\text{-}8)$$

The first and second terms are the traveling and alternating magnetic field components, respectively. The third one is an attenuating traveling wave generated at the entry end, which travels along the positive direction of z, whose attenuation constant is $1/\alpha_1$ and half-wave length

is τ_{pe}. The last term of Eqn (5-8) is an attenuating traveling wave generated at the exit end, which travels in the negative direction with the attenuation constant $1/\alpha_2$. Entry and exit waves are the speed-dependent components and have more impact at high velocities.

To have the dynamic end effects taken into account the LIM operation is modelled in FEM by using time-domain transient motion under constant supply voltage. To ensure the presence of both static and dynamic end effect, finite length of primary with infinitely long secondary is considered. Primary winding is supplied by the phase voltage of 86.6 V (rms) and 50 Hz frequency at different secondary speeds. The results of the simulation are shown in Figs. 5-18 through 5-21.

The characteristics of the primary excitation current and input impedance vs slip are plotted in Fig 5-18. FEM software that was applied uses capacitance matrix to calculate the transient winding currents in case of time varying voltage source (Appendix B)

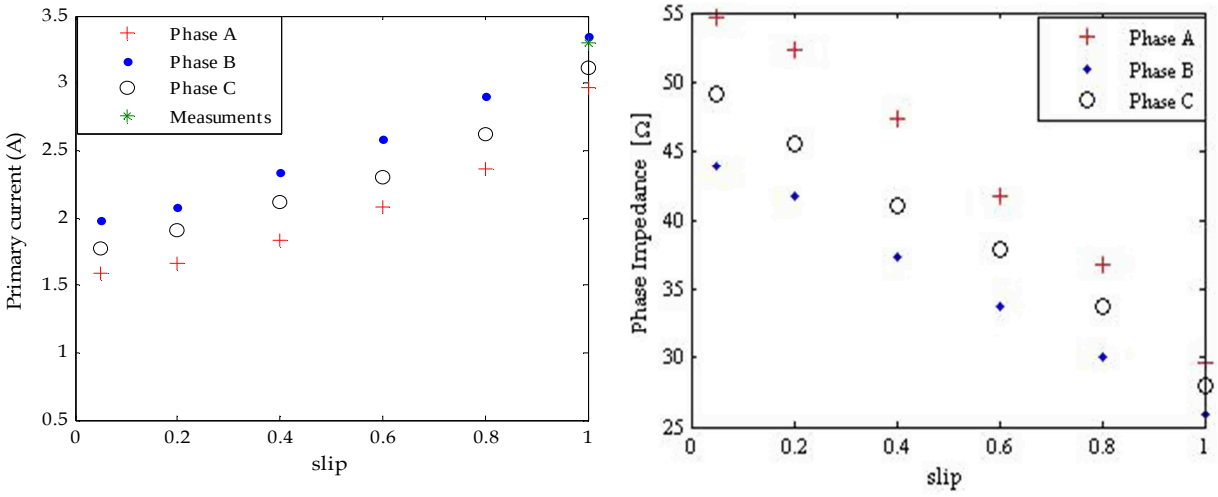

Fig 5-18. (a) Excitation currents (RMS), (b) Input impedance at 86.6 V phase voltage and 50 Hz frequency.

As mentioned earlier, the end effect leads to non-uniform distribution of magnetic field in the air-gap. Also the distribution of the currents in the secondary is not uniform. This makes the driving force density distribution being affected as well due to interaction of non-uniformly distributed current in the secondary and magnetic field. To examine how the performance of motor is affected by the end effects, results of simulation are shown in Figs. 5-19 and 5-21 (a) and (b) in form of the electromechanical force (Fem), mechanical power (Pm) and efficiency, respectively, versus linear slip of the rotor. These characteristics are drawn as continues line curves for the infinitely long motor when no end effects are considered, dotted lines for motor with static end effects and circles for the actual motor of finite armature length, when both static and dynamic end effects are taken into account. Fig. 5-20 shows the transient analysis for slip equal to 1.

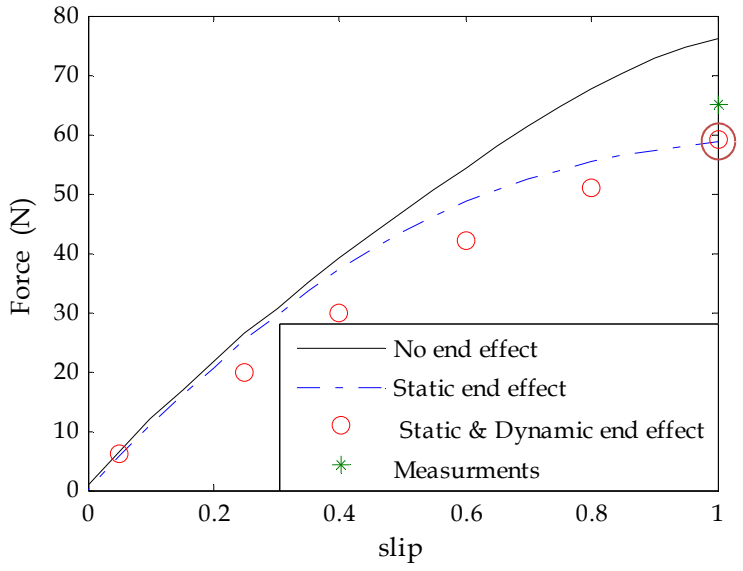

Fig 5-19. Force vs. slip characteristic under constant balanced supply voltage

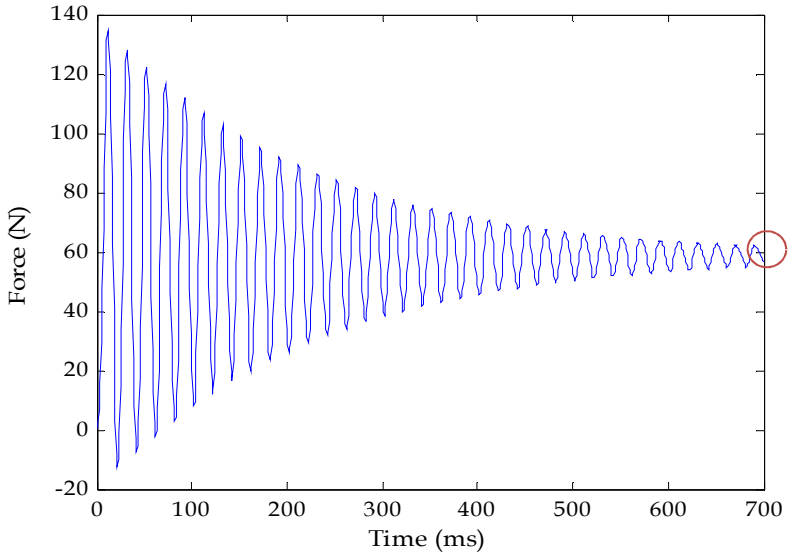

Fig 5-20. Force waveform obtained at slip =1 at transient analysis in the presence of static and dynamic end effects (initial conditions: 3-phase initial currents are equal to zero, rotor slip s = 1, initial resistance = 1.5 Ω, initial inductance = 0.1 mH , balanced supply phase voltage V_1 = 86.6 V (RMS).

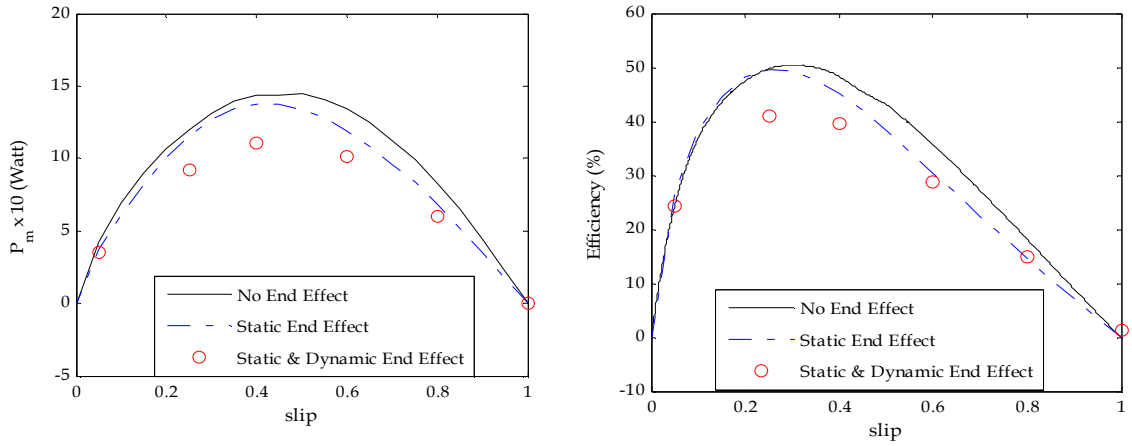

Fig 5-21. Characteristic of: (a)- Output power and (b)-Efficiency vs linear slip at V1=86.6 (RMS) and frequency equal to 50 Hz.

The motor under study has a linear synchronous speed equal to 6.15 m/s and is considered as low-speed motor. In low-speed motors, the speed of the end effect wave can be higher than the motor speed and even much higher than the synchronous speed, while in high-

speed motors the speed of the end effect wave is about the same as the motor speed and cannot be higher the synchronous speed. In low-speed motors, the attenuation of the entry end-effect wave is quick, while in high-speed motors the attenuation is very slow and the entry-end-effect wave presents over the entire longitudinal length of the air-gap. As a consequence of the difference, the influence of the end-effect wave on motor performance is also quite different at high-speed motors and low-speed motors. In low-speed motors, the end effect wave may improve motor performance in low-slip region, the important motor-run region, increasing thrust, power factor and efficiency, and allowing net thrust to be generated even at synchronous and higher speeds [6]. On the contrary, in high speed motors, thrust, power factor and efficiency are reduced to a large extent in the low-slip region.

To study the performance of the motor at higher speeds, let us change the supply frequency to 3 times higher (synchronous speed, v_s= 3 * 6.15 m/s) and then recalculate the forces acted on rotor when all end effects are taken into account. Table 5-2 compares the output forces of the low-speed and high-speed motor at relatively low operational slip region.

Table 5-2. Electromechanical force of low speed and high speed LIM.

Synchronous speed	Operational slip region	
	s=0.25	s=0.25
$\mathbf{v_s}$= 6.15 m/s	19 N	6 N
$\mathbf{v_s}$= 3*6.15 m/s	6 N	0 N

5.2.2 End Effect Modeling Using Equivalent Circuit

Dynamic end effect: One of the simplest approaches to analyze a LIM performance is to use an equivalent circuit. The steady-state analysis of a rotary induction motor is usually done by

a classical equivalent circuit shown in Fig. 5-22. The conventional equivalent circuit of rotary induction motors cannot be applied to the LIMs, because of their specific phenomena.

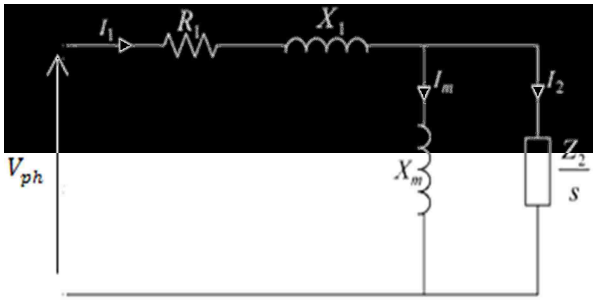

Fig 5-22. Equivalent circuit of linear induction motor by neglecting end effects.

One of the well-known models to analyze LIMs is the one suggested by Duncan [16]. In his model, first, the equivalent circuit parameters are obtained by the standard open and short circuit tests. Next, the end effect is taken into account by a proper coefficient and modification of the magnetizing branch. This model ignores the changes of parameters at different operating conditions. Because of the specific phenomena in induction motors such as skin effect and saturation of back iron, the equivalent circuit parameters change with slip and cannot be obtained by standard tests.

Duncan Model: If the secondary enters magnetic field zone (active zone), the eddy currents are induced to mirror the magnetizing current, nullifying the air gap flux at the entry to maintain its zero flux linkage (see Fig. 5-23 a). Similar phenomenon occurs at the exit edge when the secondary leaves the active zone. Induced eddy current try to maintain the flux linkage constant, making the magnetic field at the exit edge to take the form of magnetic tail (see Fig. 5-23 b).

The rise and decay of secondary eddy currents depends on the time constant $T = L/R_2$ which in the primary (active) zone $(T_r = L_r/R_2)$ differs from that outside this zone $(T_{lr} = L_{lr}/R_2)$. The secondary leakage time constant T_{lr}, is about 5% of the magnetizing or mutual inductance time constant T_r, what makes the secondary currents outside the active zone decay more rapidly than within this zone. The magnetic flux generated by the secondary currents superimposes the flux of primary part and the resultant flux density distribution looks like Fig. 5-23 b [56].

As stated above, at the entry edge the secondary eddy current grow very rapidly in such a way that the magneto-motive force of the secondary currents is almost equal and opposite to the primary magneto-motive force. Thus, the equivalent secondary current at time $t = 0^+$is practically equal to primary magnetizing current.

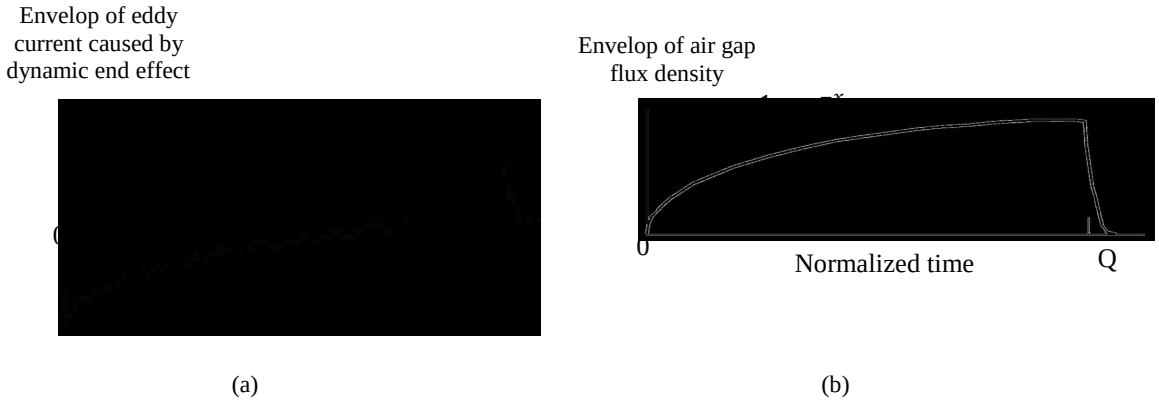

Fig 5-23. (a) Eddy-current density profile along the length of LIM generated by dynamic end effect, (b) Air gap flux profile [56].

The average value of entry eddy current over the motor length is given by:

$$i_2^e = \frac{I_m}{T_v} \int_0^{T_v} e^{-t/T_r}\, dt \tag{5-9}$$

where $T_v = l/v$ is the time that the motor needs to transverse a point on the active secondary with length equal to l. The distance travelled by the secondary in time constant is vT_r.Thus, the motor length can be normalized by such that [16]:

$$Q = \frac{T_v}{T_r} = \frac{lR_2}{(L_m + L_2)v} \tag{5-10}$$

Therefore, Q is dimensionless but represents the motor length on this normalized time scale. On this basis, the motor equivalent length is clearly dependent on the motor velocity, so that, at zero velocity, the motor length is infinitely long. As the velocity rises, the motor length will effectively shrink.

From Eqns. (5-9) and (5-10):

$$i_2^e = \frac{I_m}{Q} \int_0^{Q} e^{-x}\, dx = I_m \frac{1 - e^{-Q}}{Q} \tag{5-11}$$

Thus, the magnetizing current is reduced as follows:

$$I_m - i_2^e = I_m \left(1 - \frac{1 - e^{-Q}}{Q}\right) \tag{5-12}$$

The reduction in the magnetizing current is accounted by modifying the magnetizing inductance as follows:

$$L'_m = L_m\left(1 - \frac{1 - e^{-Q}}{Q}\right) \tag{5-13}$$

The induced eddy current circulates in secondary and causes ohmic loss. The effective value of eddy current over the motor length can be evaluated as:

$$i_{2rms} = \left(\frac{I_m^2}{Q}\int_0^Q e^{-2x}dx\right)^2 = I_m\left(\frac{1 - e^{-2Q}}{2Q}\right)^{1/2} \tag{5-14}$$

Therefore, the value of ohmic loss due to entry eddy current can be obtained by:

$$P_{entry} = i_{2rms}^2 R_2 = I_m^2 R_2 \frac{1 - e^{-2Q}}{2Q} \tag{5-15}$$

The total eddy current in the secondary placed within the primary (active) zone can be obtained from (5-12), as $I_m(1 - e^{-Q})$. To satisfy the steady-state condition in the air gap, the eddy current must be vanished at exit rail during the time T_v . Therefore, the ohmic loss caused by exit eddy current may be evaluated by:

$$P_{exit} = \frac{L_r I_m^2 (1 - e^{-Q})^2}{2\,T_v} = I_m^2 \frac{(1 - e^{-Q})^2}{2Q} \tag{5-16}$$

From (5-15), (5-16) the total ohmic loss due to eddy current caused by entry and exit end effect in the secondary takes the form:

$$P_{eddy} = I_m^2 R_2 \frac{1 - \exp(-Q)}{Q} \tag{5-17}$$

This ohmic power loss can be represented by a resistor which is connected in series to the magnetizing inductance. As it can be seen in Fig. 5-24, the difference between Duncan model

and conventional equivalent circuit of RIM is the change in the magnetizing branch due to the dynamic end effects.

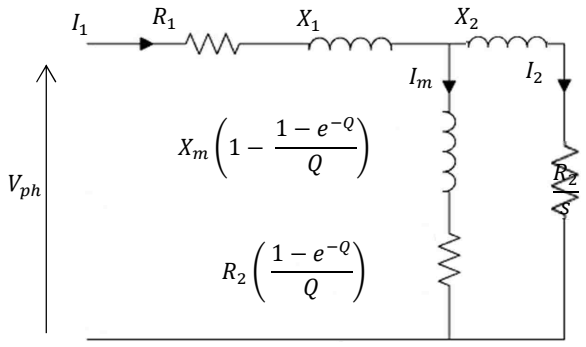

Fig 5-24. Duncan model.

Proposed Model: In LIMs, back iron material is made of steel or iron. So, at some operating conditions, saturation appears and should be taken into account.

In the suggested model, the equivalent circuit parameters are obtained from the field equations solved by FEM. First, by a simple and iterative method, permeability of back iron (μ) at each slip frequencies is obtained. Then, based on these values, the magnetic flux penetration depths are calculated at each slip frequencies. The effective thickness of the back iron is reduced accordingly in such a way that the thickness of the back iron becomes equal to the penetration depth of the magnetic flux at each particular slip frequency. Next, the field equations are solved by the FEM with the slip frequency set to zero for all of the cases. This prevents eddy currents to be induced in the secondary and makes the secondary impedance infinity which models the motor as if it were operating at synchronous speed for each operational slip. Now, the characteristic of the magnetizing inductance vs. slip can be obtained by subtracting the leakage inductance from the total inductance. (calculation of primary leakage inductance is brought in Appendix C). Having obtained the magnetizing inductance and total input impedance, one may

calculate secondary parameters by a simple circuit analysis. Finally, by using the Duncan method, the dynamic end effect is included in the model. Note, the transverse edge effect is not included in the model as it does not exist in the motor with cylindrical type of rotor. The procedure to determine the model parameters is shown in flowchart presented in Fig. 5-25.

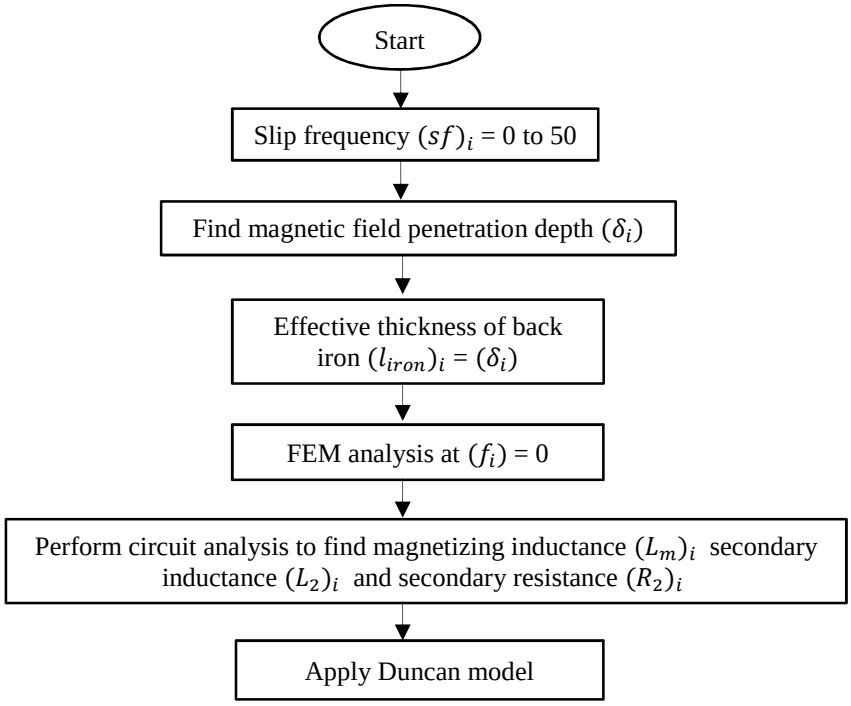

Fig 5-25. Proposed model procedure.

The saturation coefficient for the secondary back iron Ks is the ratio of back iron reluctance to the sum of the conductor and the air-gap reluctances. Considering the depth of field penetration in iron as δ_i and the average length of back iron flux path as $1/\beta$, the saturation factor takes the following form [13]:

$$K_s = \frac{\mu_i}{\mu_0 \, \delta_i \, g_0 \, K_c \, \beta^2} \tag{5-18}$$

$$\delta_i = \sqrt{\frac{2}{2\pi sf\sigma\mu_i}} \tag{5-19}$$

where K_c is Carter's coefficient, g_0 is the Magnetic air gap (mechanical air gap + copper thickness), σ is the back iron's conductivity in Siemens/meter, *sf* is slip frequency and μ_i is the average permeability of back iron at each slip frequency and is computed during an iterative procedure as follows [13]:

First, a reasonable value for μ_i is guessed. The saturation coefficient, Ks causes to increase in air gap length:

$$g_{ei} = g_0 K_c (1 + K_s) \tag{5-20}$$

Approximate value of the air gap flux density can be determined as follows: [57]:

$$B_{ag} = \frac{jJ_m\mu_0}{g_{ei}\beta(1 + jsG_e)} \tag{5-21}$$

where G_e is the goodness factor and J_m is the amplitude of an equivalent stator current sheet calculated as:

$$J_m = \frac{\sqrt{2}mN_{ph}K_wI}{p\tau} \tag{5-22}$$

where m is the number phases, N_{ph} is the number of turns per phase, K_w is the winding factor, I is the primary current, p is the number of poles, and τ is the pole pitch.

Assuming an exponential form for the field distribution in back iron, the flux density at the surface of iron is given by:

$$B_i = \frac{B_{ag}}{\delta_i \beta} \tag{5-23}$$

With this flux density and using back iron saturation curve, a new value for the back iron permeability, μ' is calculated. Using the following expression, a new iteration is commenced, and the computation is carried out until sufficient convergence is attained:

$$\mu_{new} = \mu_{old} + 0.1(\mu' - \mu_{old}) \tag{5-24}$$

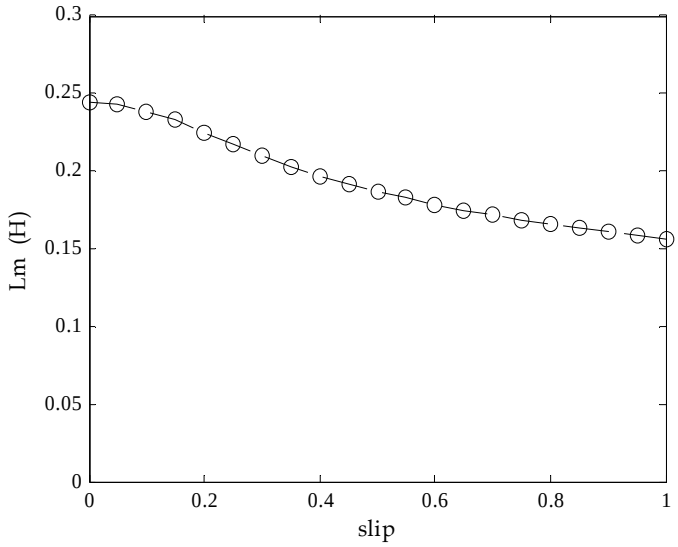

Fig 5-26. Characteristic of magnetizing inductance vs linear slip varying due to saturation of back iron (I = 4.24 A (max), f = 50 Hz).

Fig 5-26 shows how the magnetizing inductance changes vs slip due to saturation of back iron. Due to the skin effect, eddy currents induced in the secondary mostly flow on the surface and secondary resistance goes up at high frequencies (higher slip) (Fig 5-27). The calculations were done for phase current I = 4.24 A (max) and supply frequency f = 50 Hz. The equivalent circuit of the proposed method is shown in Fig 5-28.

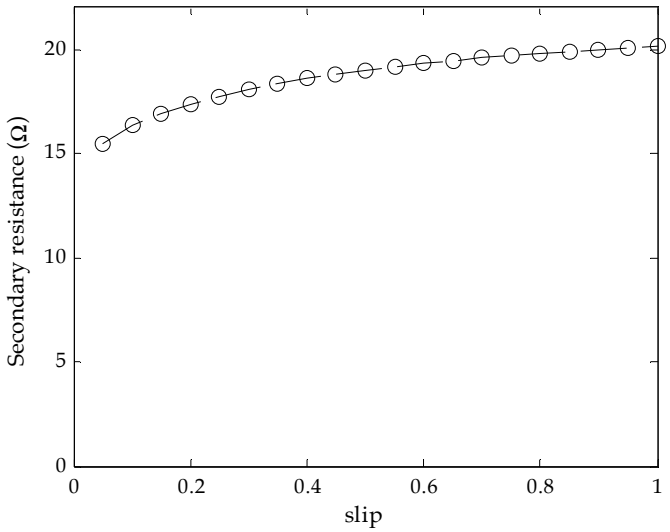

Fig 5-27. Characteristic of secondary resistance vs linear slip varying due to skin effect (I = 4.24 A (max), f = 50 Hz).

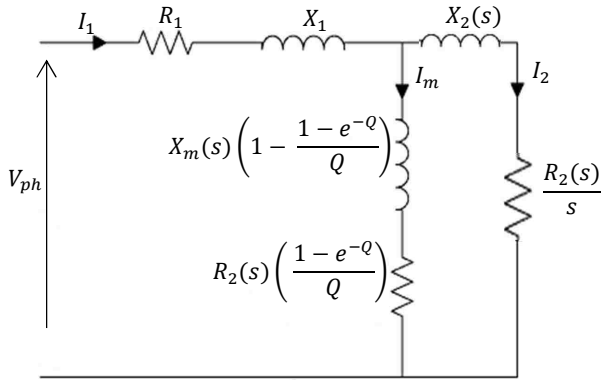

Fig 5-28. Equivalent circuit of the proposed method (Skin effect and dynamic end effects are included).

As mentioned earlier, because of the specific phenomena in LIMs, the equivalent circuit parameters change with slip and cannot be obtained by standard short and open circuit tests. One may obtain the force based on equivalent circuit approach as follows:

$$F = 3|I_2|^2 \frac{R_2}{s} \frac{1}{v_s} \tag{5-25}$$

where $v_s = 2\tau f$ is the synchronous speed.

The motor thrust plotted against slip without the end effect along with the results of the Duncan and proposed model is shown in Fig 5-29. As it is seen, the end effect decreases the motor thrust. Also, by comparing the result obtained from Duncan model with the ones obtained from the proposed model, one can observe that the skin effect influences the trust mostly at locked rotor position and slip close to1. As expected from the theory of induction motors, skin effect does not affect the performance of the motor at or close to synchronous speed.

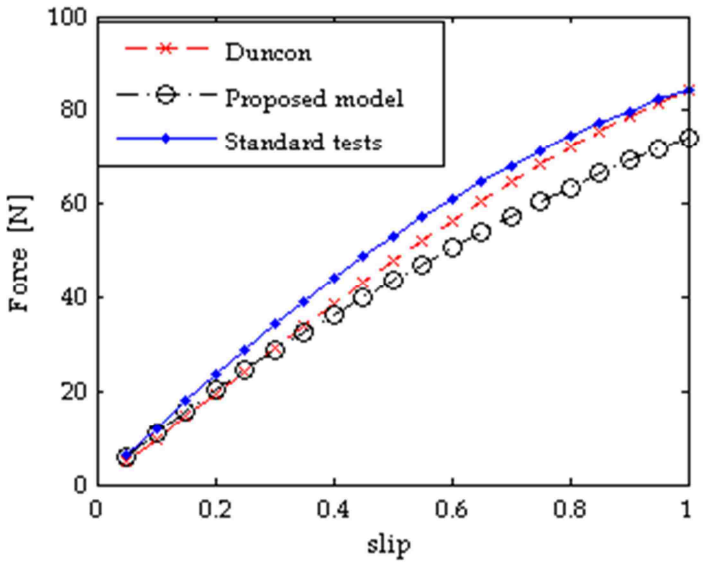

Fig 5-29. Characteristic of force vs linear slip using equivalent circuit approach.

Static end effect: A novel approach for modeling static end effect in the equivalent circuit is proposed. It is based on the theory that the alternating mmf (caused by static end effect) can be generated by a virtual coil that surrounds the primary. This coil is similar to the compensating

winding with the reversed current. Compensating coil can eliminate alternating magnetic field component responsible for static end effect. Therefore, by adding the counterpart of the compensating coil into the equivalent circuit model of infinitely long LIM, one may derive an equivalent circuit which includes static end effect.

Methods to compensate the ac mmf that is due to the short primary were proposed previously in [6], [19],[24], [58].One of these methods uses the compensating coil wound around the primary with the appropriate number of turns and current. This method creates the magnetic field directed opposite to the ac mmf. A diagram of the LIM with a compensating coil is shown in Fig. 5-30.

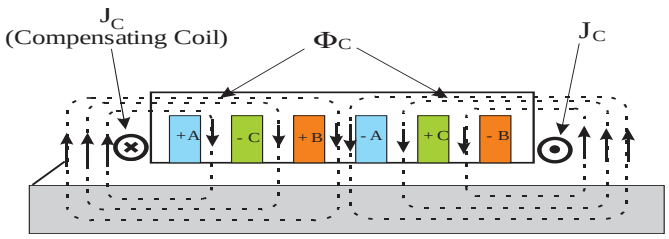

Fig 5-30. Schematic picture of LIM with compensating coil.

Another method is illustrated in Fig. 5-31 where a double-layer 3-phase winding is applied. Fig. 5-31(c) shows the distribution of current flowing in the winding at instant t_1 and its first space harmonic J_1. The traveling component of the mmf, F_t, produced by J_1 and the alternating component of the mmf, F_a, caused by the finite length of the stator are shown along with the compensating mmf, F_c, in Fig. 5-31(c).

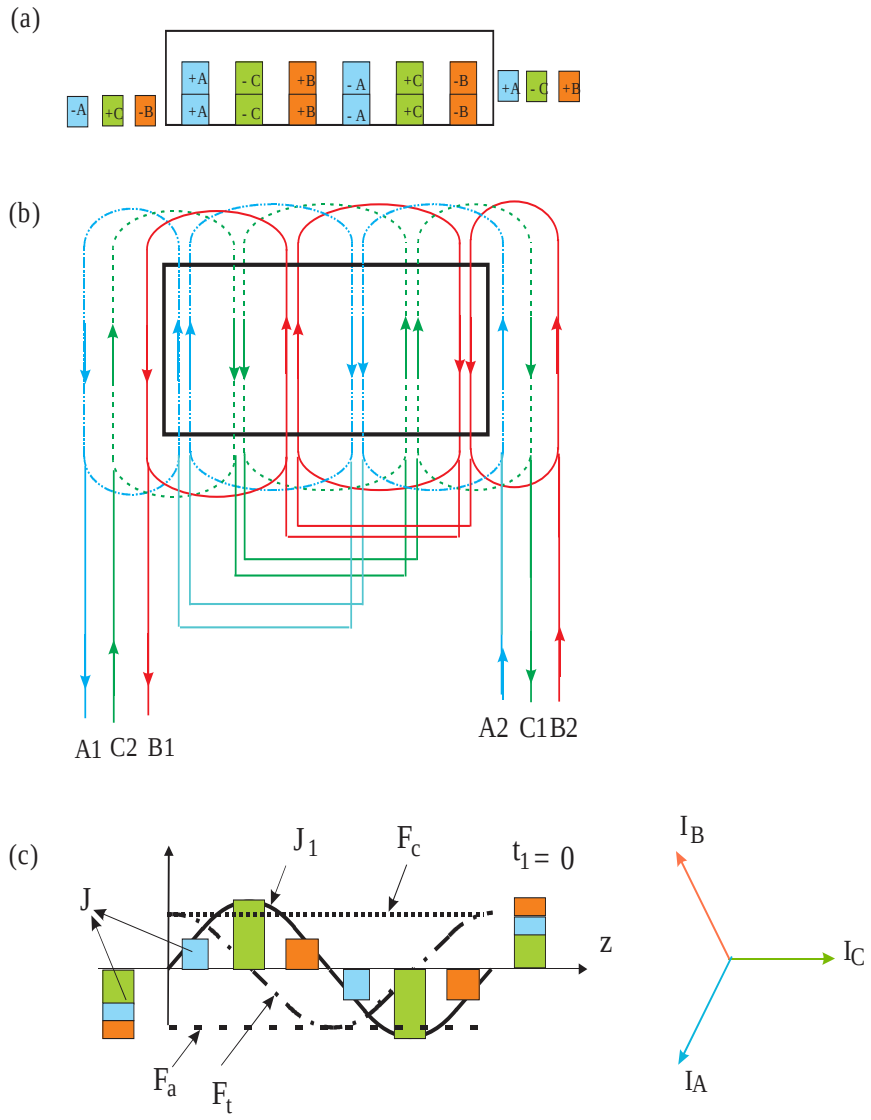

Fig 5-31. (a) - LIM with flat structure and double-layer 3-phase winding, (b) – circuit diagram of double layer winding that compensates ac component of magnetic field (c) – current density and magneto-motive force F distribution: J_1 – first harmonic of J, F_t – first harmonic of F (travelling component), F_a – alternating component of F (caused by finite lentgh of primary) F_c – compensating component of F generated by the coil sides placed out of the primary.

It is worth noting that the winding diagram shown in Fig. 5-31(b) is for a linear motor with a flat structure. The winding diagram for a tubular motor does not include end windings and is drawn in Fig 5-32.

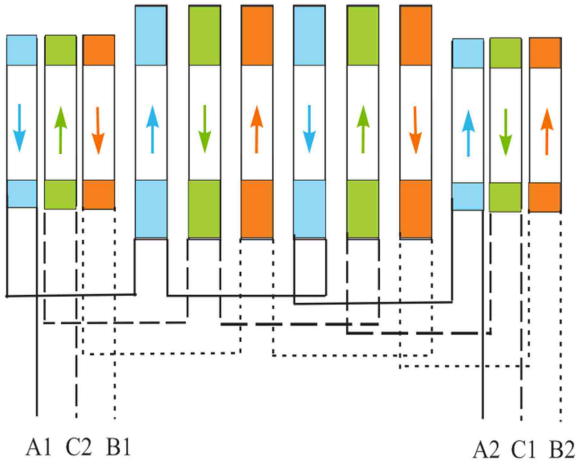

Fig 5-32. Double layer winding diagram for the tubular motor.

A cutaway 3-D view of a tubular LIM with a double-layer winding is shown in Fig. 5-33. The magnetic flux density distribution in the middle of the air gap along the longitudinal axis is computed at both synchronous speed and locked rotor position and compared to the motor with single-layer winding (Fig. 5-34). It can be observed that the flux density distribution in the model with a double-layer winding is more uniform which indicates that this type of winding significantly eliminates the alternating mmf created by the static end effect.

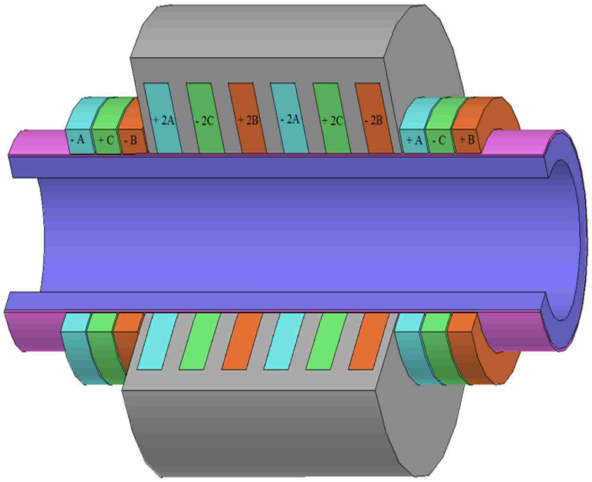

Fig 5-33. Cutaway 3-D view of a tubular LIM with a double-layer winding.

Furthermore, since current distribution in the active zone (currents in winding placed in slots) are the same in both types of windings the current flowing through the winding placed outside of the primary is in charge with compensating of ac component of the magnetic flux.

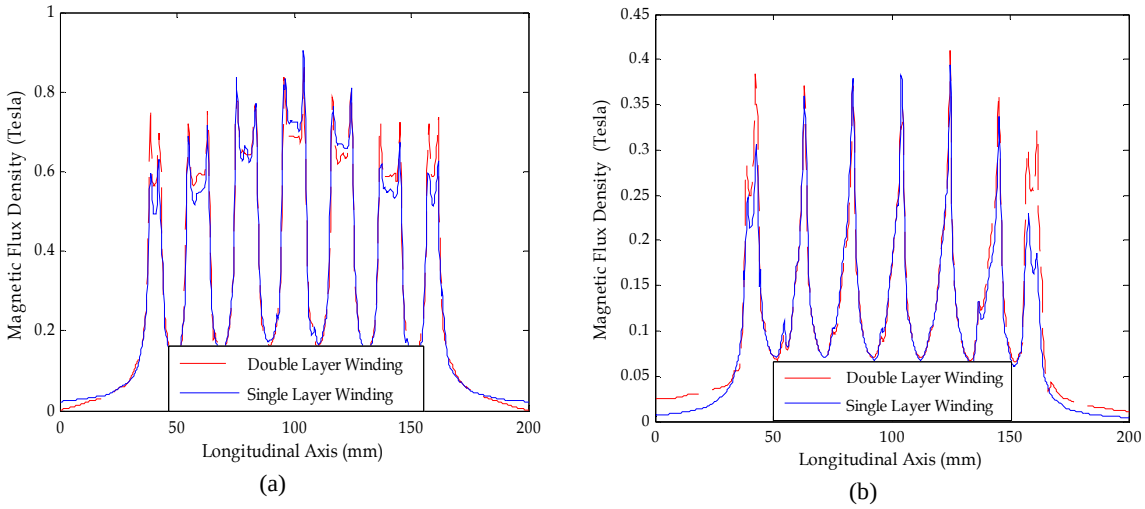

Fig 5-34. Magnetic flux density distribution in the middle of the air gap calculated for data enclosed in Table 5-1: a) Synchronous speed, b) Locked rotor position. No dynamic end effects are considered at synchronous speed.

To derive the function that describes the ac mmf, let us consider a balanced three-phase current flowing through the three-phase winding as shown in Fig. 5-31 (a). The currents are:

$$\left.\begin{aligned} i_a &= I_m \cos \omega t \\ i_b &= I_m \cos(\omega t - 120^o) \\ i_c &= I_m \cos(\omega t + 120^o) \end{aligned}\right\} \tag{5-26}$$

Let us consider the mmf produced by the part of the winding placed outside the primary core as shown in Fig. 5-35 (a). The distribution of mmf at time t_1 for each of the phases has a rectangular form as shown in Fig. 5-35 (b). For further consideration only first harmonic of mmf space distribution $F_1(\theta, t)$ (Fig. 5-35 (b)) is considered.

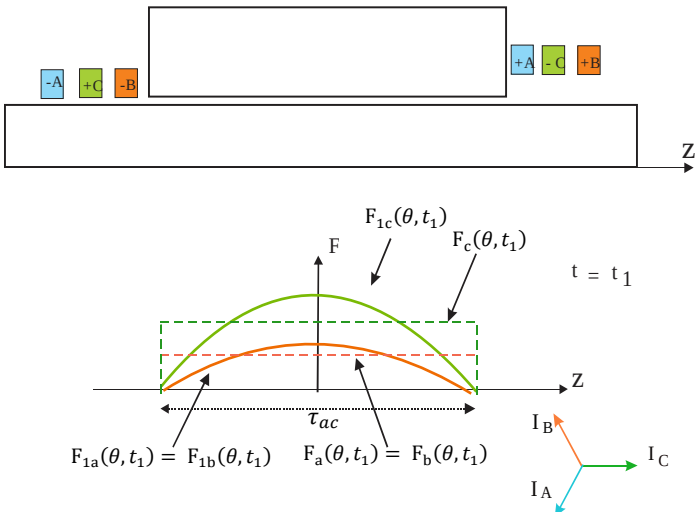

Fig 5-35. mmf produced by the part of the winding placed outside the primary core at time instant t = t_1.

The resultant magneto-motive force is the sum of:

$$F_1(\theta,t) = F_{1a}(\theta,t) + F_{1b}(\theta,t) + F_{1c}(\theta,t) \tag{5-27}$$

where

$$\left.\begin{aligned} F_{1a}(\theta,t) &= Ni_a \cos\theta \\ F_{1b}(\theta,t) &= Ni_b \cos\theta \\ F_{1c}(\theta,t) = Ni_c \cos(\theta - 180^0) &= -Ni_c \cos\theta \end{aligned}\right\} \tag{5-28}$$

where: N is the number of turns in each phase coil placed outside the LIM primary.

$$\theta = \frac{\pi}{\tau_{ac}} z \qquad \text{(See Fig. 5-35 (b))} \tag{5-29}$$

The phase currents i_a, i_b, and i_c are time functions. By replacing the phase currents in Eqn. (5-28) with the functions (5-26) and then inserting it into Eqn. (5-27), the resultant mmf takes the form:

$$F_1(\theta, t) = N I_m \cos\theta \{\cos\omega t + \cos(\omega t - 120^O) - \cos(\omega t + 120^O)\} \quad (5\text{-}30)$$

After trigonometric transformation:

$$F_1(\theta, t) = -2N I_m \cos\theta \cos(\omega t + 120^O) \quad (5\text{-}31)$$

or

$$F_1(\theta, t) = -2N i_c \cos(\theta) \quad (5\text{-}32)$$

Referring to Eq. (5-32), the resultant mmf of part of the 3-phase winding placed outside the LIM primary can be regarded as a single coil with double the number of turns (2N) and the current equal to that of phase C. Since Eq. (5-32) describes the mmf of the compensating component, the ac mmf generated by the virtual coil should have an opposite sign meaning a single coil placed outside the primary with double the number of turns (2N) with current equal and negative to that of phase C could simulate the presence of the static end effect in the model. (Fig. 5-36)

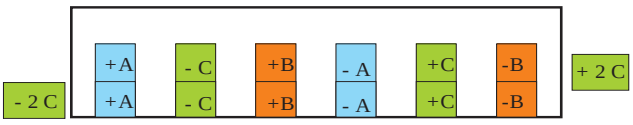

Fig 5-36. LIM with a single virtual coil and double the number of turns (2N) with current equal and negative to that of phase C.

Thus, the ac mmf generated by the virtual coil is expressed by the function:

$$F_{1ac}(\theta, t) = 2N i_c \cos(\theta) = 2N I_m \cos\theta \cos(\omega t + 120^O) \quad (5\text{-}33)$$

The ac mmf derived above can be expressed as the sum of two cosine functions revolving in opposite directions:

$$F_{1ac}(\theta,t) = NI_m \cos(\omega t + 120 - \theta) + NI_m \cos(\omega t + 120 + \theta) \qquad (5\text{-}34)$$

The ac component of static end effects magnetic flux contributes to the induction of emf Eac in the primary winding and to the eddy currents in the secondary part. To include this phenomenon in circuit theory of LIM, an equivalent circuit relevant to single-phase induction motor is proposed. According to this theory the ac magnetic flux ϕ_{ac} can be represented by two magnetic fluxes (ϕ_f, ϕ_b) rotating (travelling) with the same speed in opposite directions as shown in 5-37 (a). In the circuit theory these two components are represented by the equivalent circuit shown in 5-37 (b) [59]. In this equivalent circuit:

X_{2ac} = secondary leakage reactance of ac component

R_{2ac} = secondary resistance of ac component

X_{mac} = magnetizing reactance of ac component

$S_{f(b)}$ = secondary slip with respect to forward and backward of ac magnetic flux.

(a) (b)

Fig 5-37. a) Forward and backward ac magnetic flux b) Equivalent circuit of ac component.

In 3-phase LIM, the EC model of ac component of magnetic field can be added to the per-phase equivalent circuit relevant to the travelling magnetic field component determined for LIM with infinite long primary (no static end effects). This is shown in Fig. 5-38.

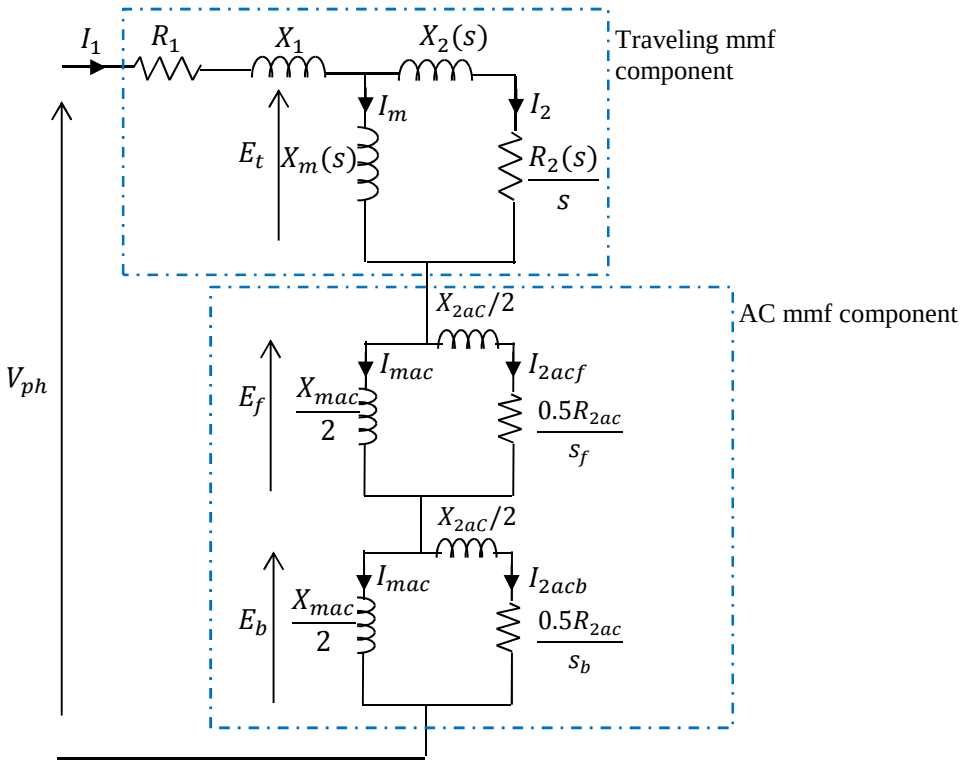

Fig 5-38. EC model of LIM with static end effect.

The primary current I_1 contributes to the voltage drop across the primary winding resistance R_1 and leakage reactance X_1. The voltage E_t is induced by the traveling field component and two voltages, E_f and E_b, which are induced in the primary winding by the forward and backward field components. Note that there is no real physical coil added to the motor, but, rather, the static end effect is modeled by the virtual 3-phase (or single phase with doubled turns) coils to model the interaction between the ac magnetic field of the static end effect and the currents induced in the secondary and its effect on the motor performance.

The parameters of this circuit can be determined from the field theory. The approach used for such a purpose is based on the standard tests which were extensively presented in previous section. Parameters related to the main travelling field component (infinitely long motor) and the ac field components (static end effect) are calculated separately by using superposition principle. For the sake of simplicity, in determining parameters related to the ac mmf (the part related to the static end effect), saturation of the magnetizing inductance is ignored and L_{mac} is calculated as a single value for all operational slip regions by the standard no load test via FEM. To obtain the proper value for the magnetizing inductance, the leakage inductance is first calculated and then subtracted from the total inductance. Secondary parameters are then determined by the blocked rotor test. The procedures of the tests are expressed by the Eqns. (5-35) through (5-38).

The ratio of the no-load voltage to current represents the no-load impedance which, from the no-load equivalent circuit, is:

$$\frac{V_{NL}}{I_{NL}} = Z_{NL} = \sqrt{R_{NL}^2 + X_{NL}^2} \tag{5-35}$$

Magnetizing inductance is calculated by subtracting leakage inductance from the total no-load inductance:

$$X_{mac} = X_{NL} - X_{1ac} \tag{5-36}$$

Once, the primary and magnetizing branch parameters are determined, the secondary circuit parameters referred to the primary side can be calculated from the equivalent circuit. The per phase equivalent impedance of the motor seen from the primary winding side at standstill (slip s = 1) is equal to:

$$Z_{eqac} = R_{1ac} + jX_{1ac} + \frac{jX_{mac}Z'_{2ac}}{jX_{mac} + Z'_{2ac}} \tag{5-37}$$

The secondary equivalent circuit parameters are then:

$$Z'_{2ac} = R'_{2ac} + jX'_{2ac} = -\frac{jX_{mac}\,(Z_{eqac} - R_{1ac} - jX_{1ac})}{Z_{eqac} - R_{1ac} - jX_{1ac} - jX_{mac}} \tag{5-38}$$

These types of calculations were carried out and the computed values of the all circuit parameters are enclosed in Table 5-3.

Table 5-3. EC parameters of the proposed model.

	R_1	L_1	$L_m(s)$	$R_2(s)$	L_2(s)
Travelling field component	2.22Ω	0.036 H	0.24 to 0.15 H	16 to 20	0.014 to 0.019 H
			L_{mac}	R_{2ac}	L_{2ac}
ac field component			0.01 H	2.7 Ω	0.003 H

As shown in Table 5-3, the leakage and the magnetizing inductances corresponding to the ac mmf is significantly lower than the main travelling field component which means the saturation caused by the ac mmf is far less than that caused by the main travelling field and can be ignored. Therefore, the assumption that is made on considering the linear magnetization characteristics of the rotor core in determining the ac mmf parameters does not affect the accuracy of the proposed model.

In general, the slip of the secondary with respect to the ac mmf is different than that of the traveling field. As it is known, this depends on the speed of the forward and backward travelling (rotating) components expressed as follows:

$$v_{1f} = 2\tau_{1f} f, \qquad v_{1b} = -2\tau_{1b} f \tag{5-39}$$

The pole pitches τ_{1f} and τ_{1b} have the same length equal to the length of primary core. This length is a multiple of the main travelling mmf component's pole pitch τ_t.Thus:

$$\tau_{1(f,b)} = p\,\tau_t \tag{5-40}$$

where p is the number of poles.

The slips of secondary with respect to travelling, forwards and backwards components are:

$$s = \frac{v_{1t} - v}{v_{1t}}, \qquad s_f = \frac{v_{1f} - v}{v_{1f}}, \qquad s_b = \frac{v_{1b} - v}{v_{1b}} \tag{5-41}$$

Inserting Eqns. 5-39, 5-40 into 5-41:

$$s = \frac{v_{1t} - v}{v_{1t}}, \qquad s_f = \frac{pv_{1t} - v}{pv_{1t}}, \qquad s_b = \frac{-pv_{1t} - v}{-pv_{1t}} \tag{5-42}$$

Rewriting Eqn. 5-42 in terms of p and s, yields:

$$s_f = \frac{p - 1 + s}{p}, \qquad s_b = \frac{p + 1 - s}{p} \tag{5-43}$$

In the motor under analysis with two poles (p=2) forward and backward slips take the form:

$$s_f = \frac{1 + s}{2}, \qquad s_b = 2 - \frac{1 + s}{2} \tag{5-44}$$

The resultant electromechanical force of EC at any operational slip region is given by the superposition principle:

$$F(s) = F_t(s) + F_f(s) + F_b(s) \quad (5\text{-}45)$$

At standstill, the forces produced by the forward and backward travelling fields of the ac mmf are equal in magnitude, but opposite $|F_f(s = 1)| = |F_b(s = 1)|$, which accounts for the fact that at standstill the resultant force produced by the ac mmf is zero ($F_{ac}(s = 1) = F_f(s = 1) + F_b(s = 1) = 0$). However, the EC series connection of the part representing the ac mmf to the main travelling component contributes to the higher EC input impedance and the lower primary current accordingly. Thus, the electromagnetic force produced by the stator winding and, accordingly, the total force decrease which is expected due to the presence of the static end effect. The motor primary current, thrust, mechanical power and efficiency plotted against linear slip in FEM along with the results of the proposed circuit model are shown in Figs. 5-39, 5-40 and 5-41 respectively. The calculations were carried out at supplied voltage of 86.6 V and 50 Hz frequency. As it is seen, the static end effect decreases the motor thrust. Also, results are in a quite good agreement with FEM, substantiating the validity of the proposed model.

It must be pointed out that the proposed part of the EC related to the ac mmf is valid only for a sinusoidaly distributed mmf, while, however, in reality the ac mmf distribution has a rectangular form which is not purely sinusoidal. Therefore, to make the ac mmf distribution compatible with the proposed solution, only the first space harmonic of the mmf distribution is considered. However, the EC parameters of the ac field component were determined in FEM for the actual distribution of the ac mmf. By doing this, the performance of the motor determined from the EC becomes closer to the actual performance.

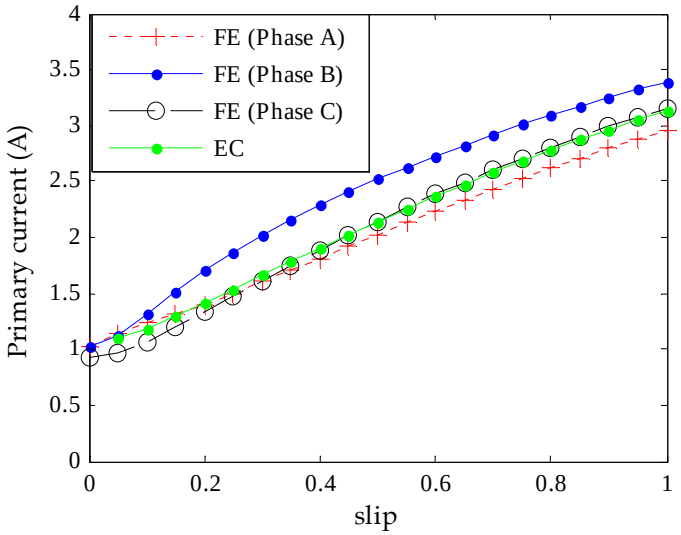

Fig 5-39. Primary (RMS) current versus slip characteristics under balanced 3-phase supply voltage of Vphase = 86.6 V.

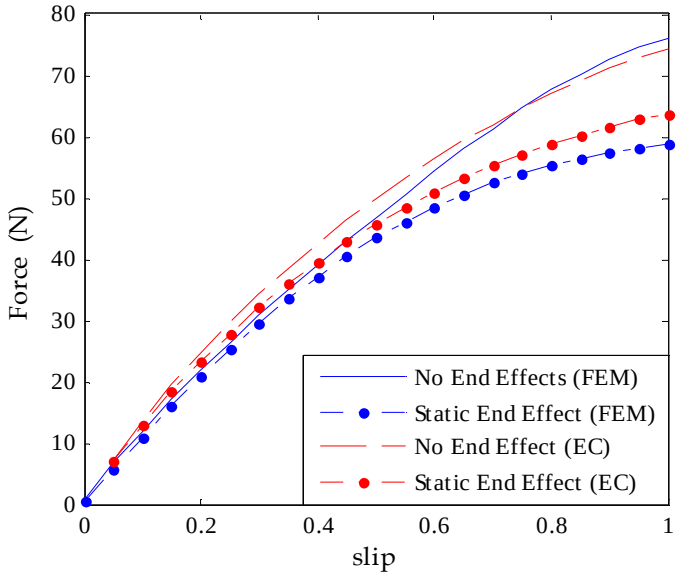

Fig 5-40. Motor thrust vs linear slip.

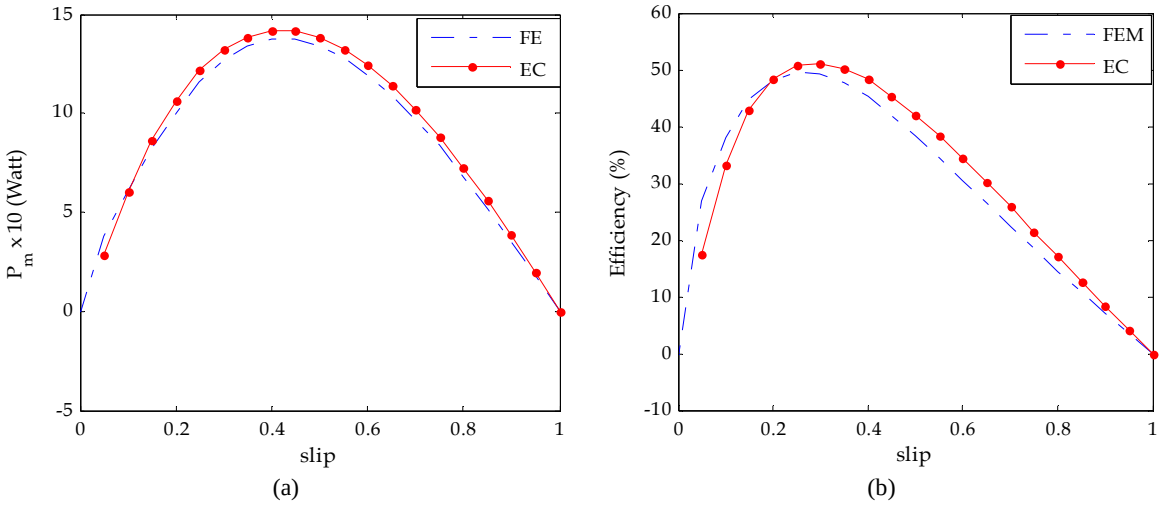

Fig 5-41. Characteristic of: (a) output power and (b) efficiency vs linear slip

Static & dynamic end effect: To include the dynamic end effect into proposed EC, magnetizing branch of traveling component is modified according to Duncan model (Fig. 5-42). To simplify the model, the influence of the dynamic end effect on the ac mmf component and vice versa is ignored.

For this type of EC with the circuit parameters shown in Table 5-3, calculations were carried out for the motor supplied with 86.6 V and 50 Hz frequency.

The characteristic of force versus linear slip for all possible three scenarios 1) no end effect, 2) static end effect, and 3) static and dynamic end effect are depicted in Fig. 5-41 and compared to the results obtained from FEM. It should be noted that the major phenomena such as saturation, skin effect, static end effect and dynamic end effect are all covered by the proposed EC model.

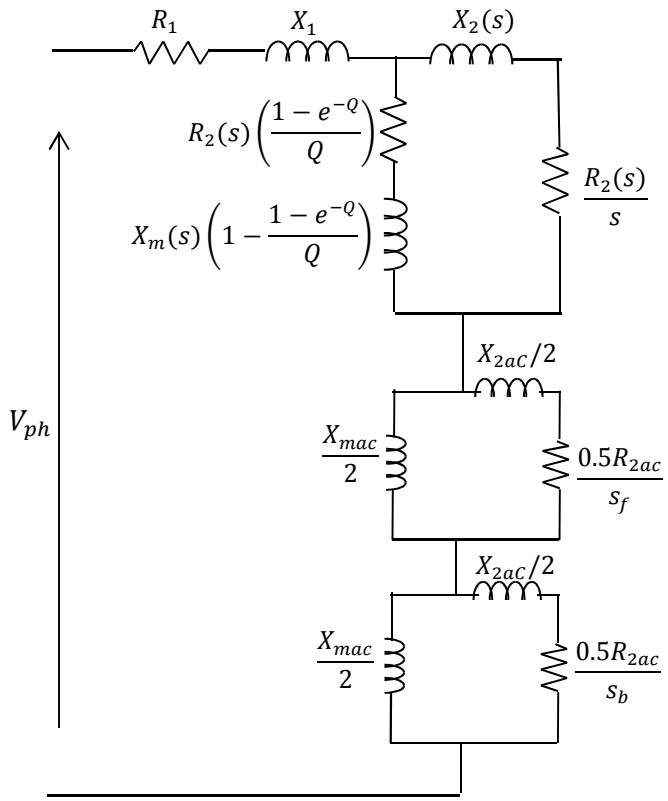

Fig 5-42. EC of LIM with static and dynamic end effect.

Dynamic end effect is present only at speeds greater than zero [60]. Therefore, at standstill (s=1), such an effect has no influence on the motor performance and the thrust with "static end effect" is equal to the thrust with "static & dynamic end effect". As shown in Fig. 5-43, the characteristics of the motor with "static & dynamic" end effect calculated by the proposed EC and FE models follow the same pattern which demonstrates the credibility of the proposed model. However, as stated before, the proposed part of EC that refers to the ac field component is valid for sinusoidaly distributed mmf, while in reality ac field component is not purely sinusoidal. Moreover, EC parameters of ac component were determined assuming linear permeability for secondary. Therefore, some discrepancies between proposed EC with FE model are expected.

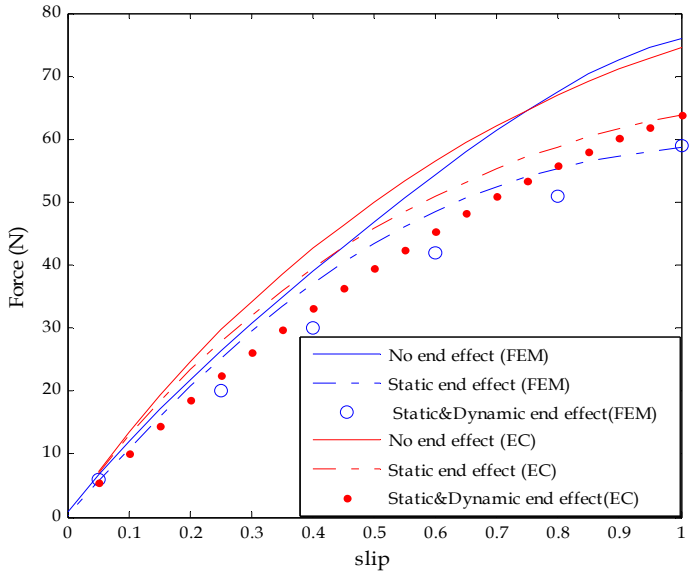

Fig 5-43. Motor of thrust vs slip.

The motor under study has a linear synchronous speed equal to 6.15 m/s and is considered as low-speed motor. In low-speed motors, the speed of the end effect wave can be higher than the motor speed and even much higher than the synchronous speed, while in high-speed motors the speed of the end effect wave is about the same as the motor speed and cannot be higher the synchronous speed. In low-speed motors, the attenuation of the entry end-effect wave is quick, while in high-speed motors the attenuation is very slow and the entry-end-effect wave presents over the entire longitudinal length of the air-gap. As a consequence of the difference, the influence of the end-effect wave on motor performance is also quite different at high-speed motors and low-speed motors. In low-speed motors, the end effect wave may improve motor performance in low-slip region, the important motor-run region, increasing thrust, power factor and efficiency, and allowing net thrust to be generated even at synchronous and higher speeds. On the contrary, in high speed motors, thrust, power factor and efficiency are reduced to a large extent in the low-slip region [6].

5.3 Rotary Motor Performance

Due to closed magnetic circuit in rotary armature (in its direction of motion), static and dynamic end effects do not exist in rotational direction. However, the performance of rotary armature might be affected by the transverse edge and dynamic end effects in axial direction during rotor axial motion. This is the only influence of linear part of TARLIM on rotary motion and, as stated earlier, both armatures have no more influence on one another due to the relatively long distance and the lack of magnetic interaction in between.

5.3.1 End Effect Modeling Using FEM

Unlike linear armature, modeling dynamic end effects in rotary armature requires a solution considering motion with two degrees of mechanical freedom (2DOF) and is more complicated than the one in linear motors. In other words, the rotor in the model would have to move between two space coordinates (rotary direction as a regular operation of rotary armature and axial direction). Neither of the available FE software package is currently capable to solve such a problem.

The approach used here to consider dynamic end effect is based on the application of time-domain transient analysis under voltage supply (for linear motion) and time-domain solution and slip transformation (for rotary motion). However, in case of motors with voltage-driven coils (the case considered) the equivalent impedance of the rotor and the primary winding currents are changed with slip frequency technique, what is a real challenge in modeling of two degree of mechanical freedom motions.

The following algorithm is proposed to circumvent such a problem:

Step 1*:* linear speed equals zero and rotary motion is modeled by time-domain transient analysis. Primary winding current is calculated and named as I_1. (Linear speed, u = 0 m/s, rotary slip, s_ω = 0.9, supply parameters: f =50 Hz and V=V_1=150 (rms)).

Step 2: linear speed still equals zero but rotary motion is modeled by slip frequency technique at current supply. The supply voltage V corresponding with the primary winding current I_1 (determined in step 1) at is calculated and named as V_2 (u = 0 m/s, s_ω = 0.9, f =45 Hz).

Step 3: linear and rotary motions are modeled through time-domain transient analysis and slip frequency technique respectively (u = 3 m/s, s_ω = 0.9, f =45 Hz and V=V_2).

Step 4: step 1 through 3 is repeated for all other rotary slips.

It is worth noting that the selection of the linear speed (u = 3 m/s) is arbitrary and the procedure remains the same for all other linear speeds. With the use of above algorithm, one may model both rotary and linear motion without having primary winding current changed due to slip frequency. Note that the difference between the primary winding currents in step 2 and step 3 is due to the presence of dynamic end effect. To determine the influence of rotor axial motion on the performance of rotary armature, the characteristics of electromagnetic torque (Tem), mechanical power (Pm), primary winding current and efficiency versus rotary slip at three different linear speeds (u = 0 m/s, u =3 m/s and u = 6 m/s) were computed and plotted in Figs 5-44 (a), (b), (c), (d). It can be seen that the associated end effects contribute to diminishing the motor performance in terms of produced torque, mechanical power and efficiency. One can observe the higher axial speed is, the lower rotary torque, mechanical power and efficiency are.

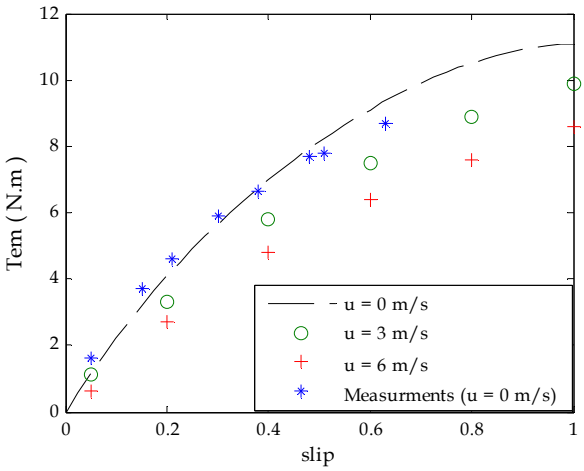

(a)

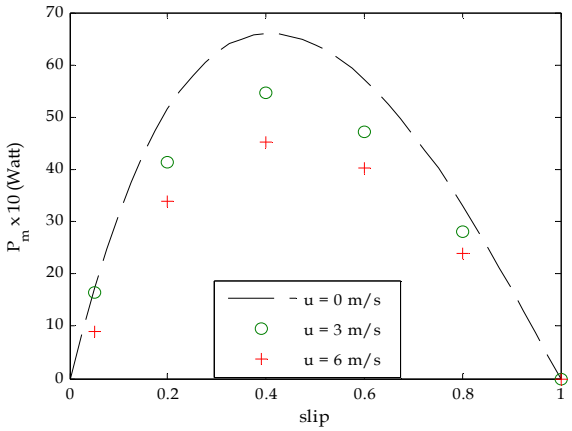

(b)

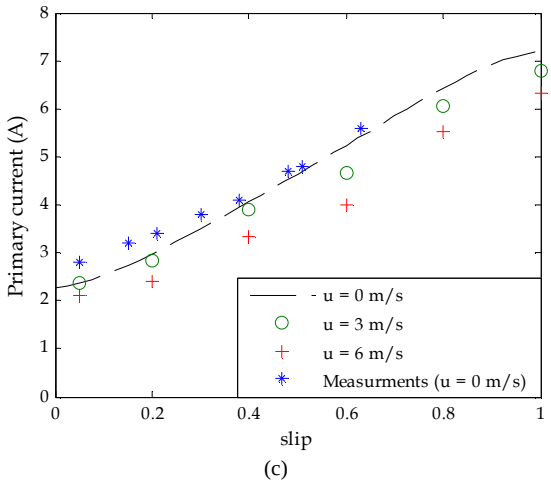

(c)

Fig 5-44. Characteristic of : (a) - Torque, (b) - Output power, (c) - Primary current (RMS), (d) – Efficiency vs rotary slip at different linear speeds (u) at V1=150 (rms) and f =50 Hz.

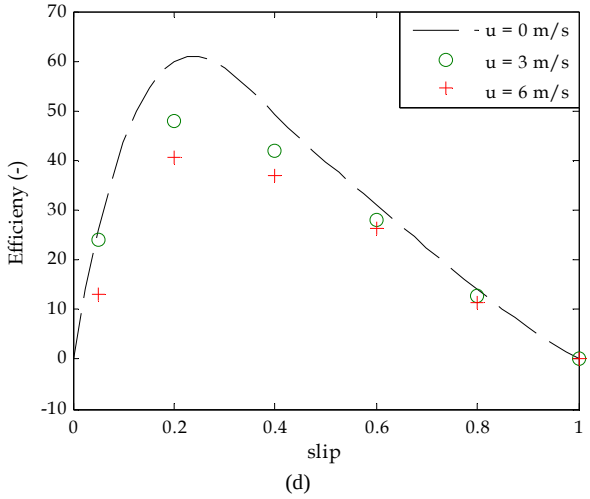

(d)

(Fig 5-44. continued).

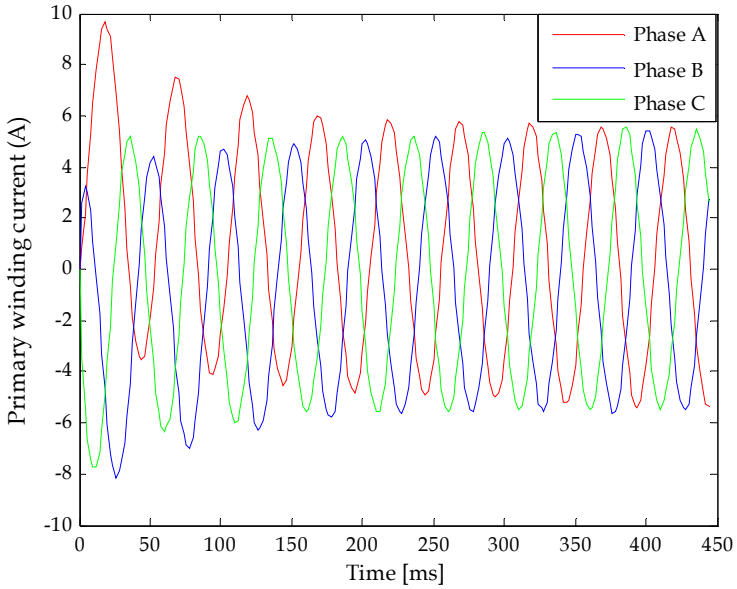

Fig 5-45. Transient characteristic of the three phase primary winding current at rotary slip = 0.4, linear speed = 3 m/s after switching on, V1 =150 (RMS) and frequency equal to f =50 Hz.

Even though the dynamic end effect reduces the primary winding currents, the three phase windings are all positioned at the same distance with respect to the edges. Therefore, the dynamic end effect caused by linear motion does not lead to currents' asymmetry and the steady-state three-phase currents are balanced. This is shown in Fig. 5-45 where the transient currents of

the rotary armature subjected to 3 m/s linear motion are depicted. It is clear that after some transient time 3-phase primary winding currents get equal at steady state condition.

5.3.2 End Effect Modeling Using Equivalent Circuit

Induction motor's conventional equivalent circuit is properly modified to address phenomena such as dynamic end effects, skin effect as well as saturation of back iron caused by rotary motion. As stated earlier, static end effect does not exist in rotary armature. The solution of the problem was extensively presented and discussed in section 5-2-2. Here, we briefly outline the solution procedure. Dynamic end effects caused by rotor axial motion is modeled by Duncon model, this is done by modifying the magnetizing branch (Fig 5-46). The saturation of back iron (due to rotary motion) is taken into account by the proposed model, similar as it was in linear armature. Note that, in case of zero axial speed, the envelope of rotary magnetic field (along the rotor circumference) is a straight line (ignoring deformation caused by slotting) so the Ducnon model is still applicable in such motors. (saturation caused by axial motion is ignored here)

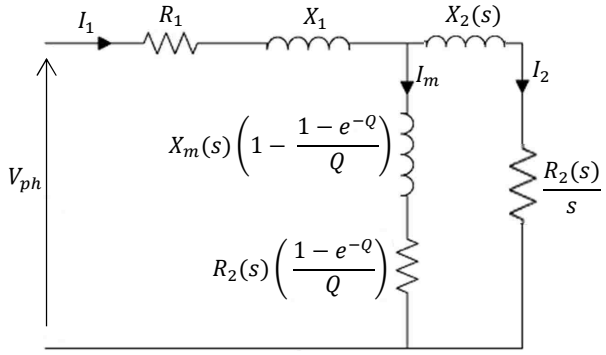

Fig 5-46. Equivalent circuit of the proposed method.(Skin effect and dynamic end effects are included).

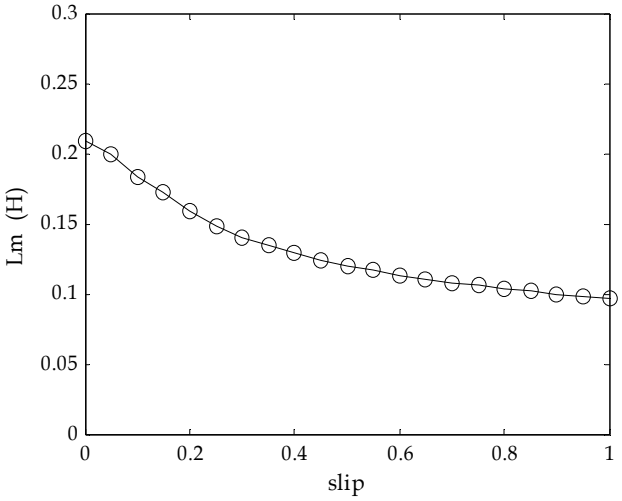

Fig 5-47. Characteristic of magnetizing inductance vs rotary slip due to saturation of back iron.

The effect of the saturation of back iron (due to rotary motion) on making the magnetizing inductance as a variable quantity in different operational conditions is shown in Fig 5-47.The values of equivalent circuit parameters are enclosed in Table 5-4.

Table 5-4. EC parameters of the proposed RIM.

EC Parameters	R_1	L_1	$L_m(s)$	$R_2(s)$	L_2(s)
	6.28Ω	0.01 H	0.21 to 0.1 H	10 to 11.5 Ω	0.01 to 0.04 H

The characteristics of electromagnetic torque (Tem) and mechanical power (Pm) versus rotary slip obtained from proposed circuit model that includes dynamic end effects at three different linear speeds (u = 0 m/s, u =3 m/s and u = 6 m/s) are plotted in Figs 5-48 and 5-49. Results obtained from EC model are in good agreement with FEM results demonstrating credibility of the proposed circuit model.

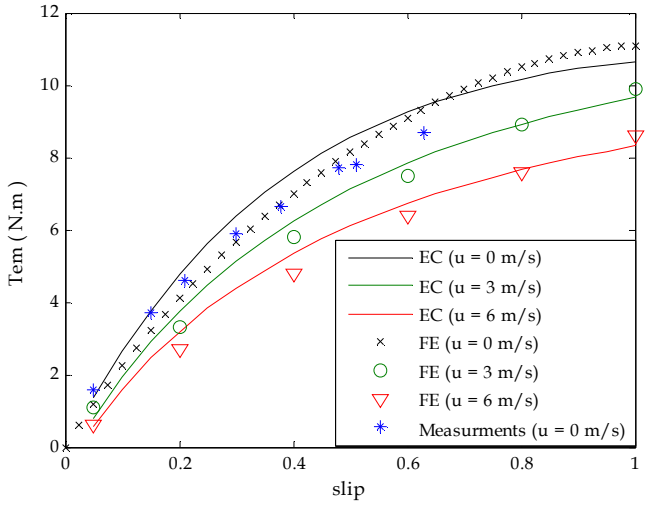

Fig 5-48. Characteristic of torque vs rotary slip at different linear speeds (u) at V1=150 (rms) and f =50 Hz.

As shown in Fig 5-49, results obtained from proposed model are in a good agreement with the experimental results especially at high operational slip region where saturation is more likely takes place. This validates the proposed model.

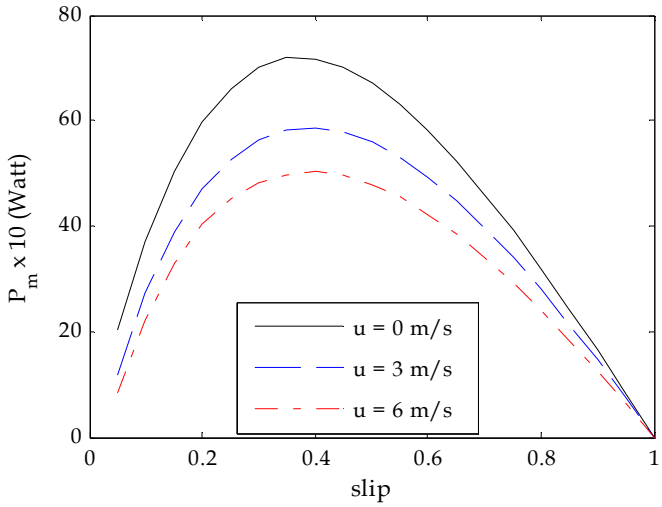

Fig 5-49. Characteristic of mechanical power vs rotary slip at different linear speeds (u) (u=0) at V1=150 (rms) and f =50 Hz.

5.4 Experimental Model

To verify the modeling results, they were compared with the results obtained from the test carried out on TARLIM shown in Fig 5-50. The measurement results for linear and rotary armatures are shown in Figs. 5-51 and 5-52 respectively. The considered quantities are extremely dependent on the properties of the materials used. The conductivity of the materials in the finite element analysis was kept constant, but in reality it is influenced by the temperature. Therefore, a mismatch between the experimental results (wherein the temperature changes during the test) and those obtained from the idealized finite element analysis exists. On the other hand, FEM needs as dense mesh as possible to compute quantities accurately, but the execution time of such a complicated model is enormous. Therefore, some trade-off between accuracy and execution time is required to obtain a good solution at reasonable cost. However, the discrepancies between test and simulation results are relatively small which validates the simulation models.

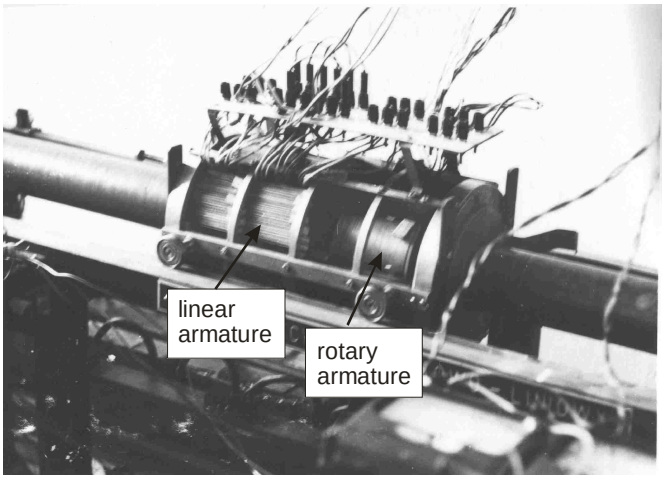

Fig 5-50. Laboratory model of twin-armature rotary-linear induction motor [1].

The laboratory model of TARLIM has a relatively short secondary length; therefore, measuring motor performances at linear speed greater than zero was technically difficult so the

test was carried out only at zero linear speed. The TARLIM operates practically at low rotary slip and at linear slip close to one. Thus the dynamic end effects does not influence much the motor performance but the static end effect caused by finite length of each of the armatures has a significant impact on the linear motor performance.

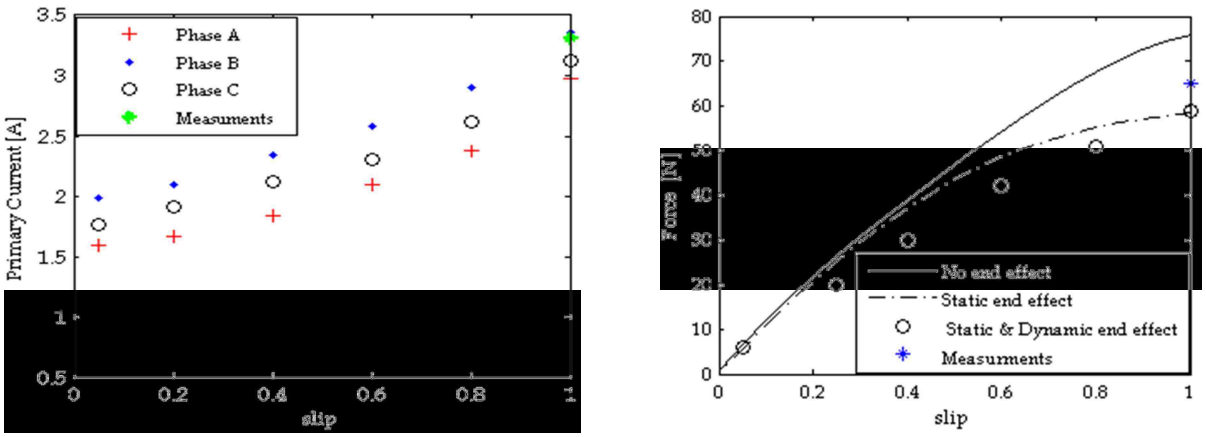

Fig 5-51. Experimental and simulated characteristic of linear armature (a) Primary current, (b) Electromagnetic force versus linear slip at V1=86.6 (rms) and f =50 Hz.

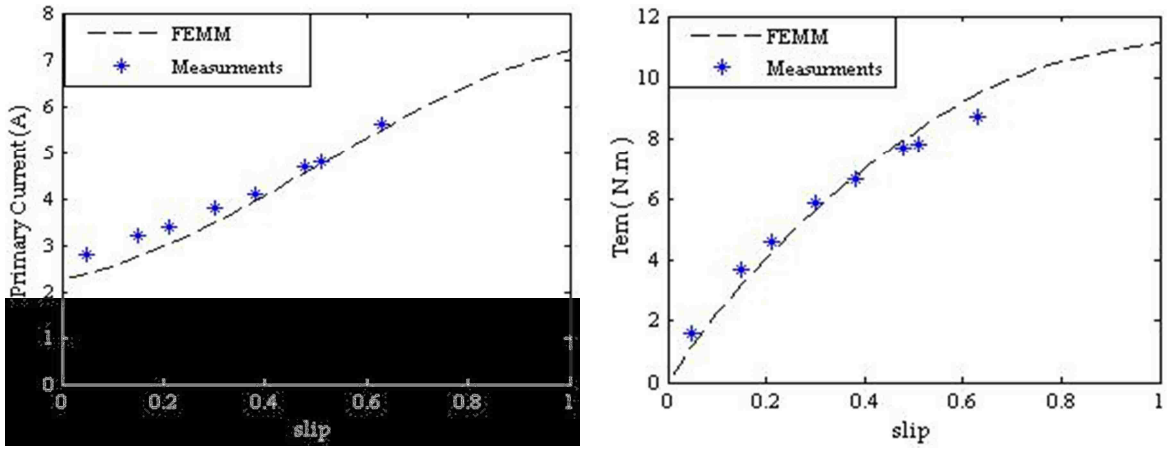

Fig 5-52. Experimental and simulated characteristic of rotary armature (a) Primary current, (b) Electromagnetic torque versus rotary slip at V1=150 (rms) and f =50 Hz.

5.5 Twin-Armature Rotary-Linear Induction Motor with Cage Rotor

The TARLIM with a cage rotor is shown schematically in Fig. 5-53. Each of the rotary and linear armatures is supplied with the same excitation as the one with solid rotor. The dimensions of the aluminum rings are optimized to provide the maximum thrust at zero speed (Fig 5-54).

Schematic 3-D view of the linear armature with cage rotor is shown in Fig 5-55. Aluminum rings used in the cage rotor provides a path for eddy currents to be induced in a perpendicular direction with respect to the traveling wave. This makes the interaction between eddy current and magnetic flux stronger. As a result, higher electromagnetic force is expected in motors with cage rotor at the same excitation current. Fig 5-56 shows FEM simulation results for cage rotor in terms of electromagnetic force with the inclusion of static end effects compared to motor with solid rotor.

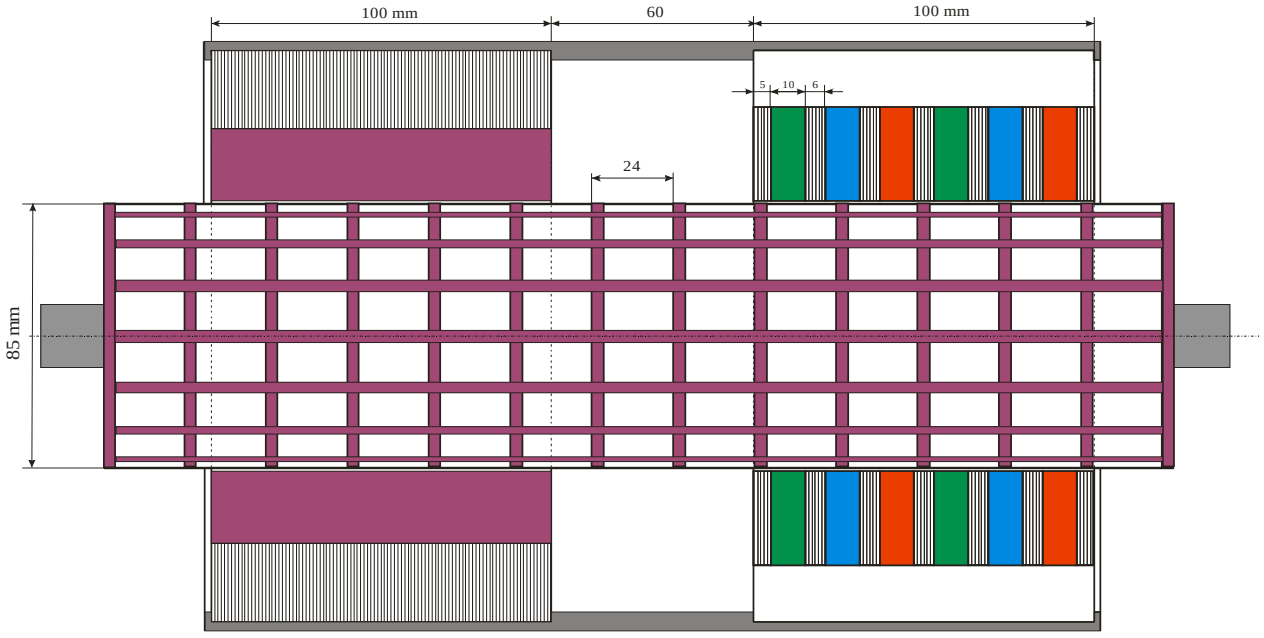

Fig 5-53. TARLIM with cage rotor.

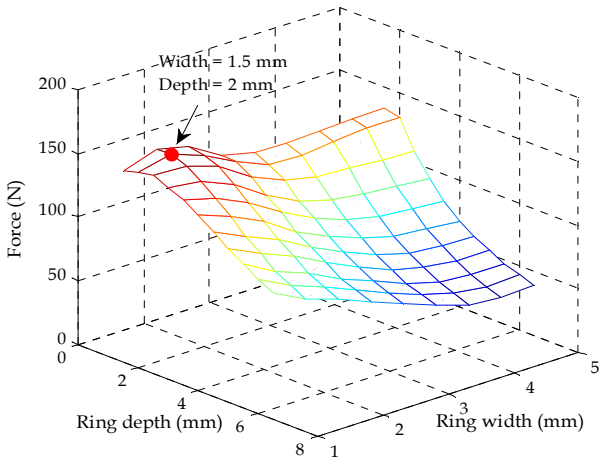

Fig 5-54. Optimized dimension of the rings.

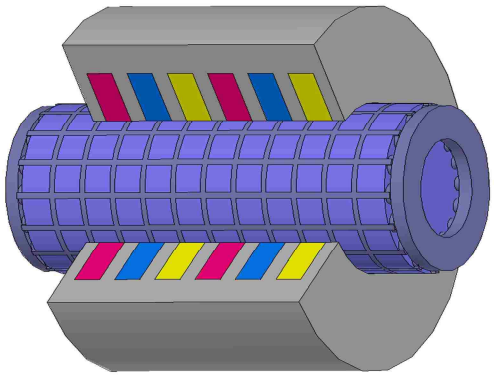

Fig 5-55. LIM with cage rotor (with aluminum rings and bars).

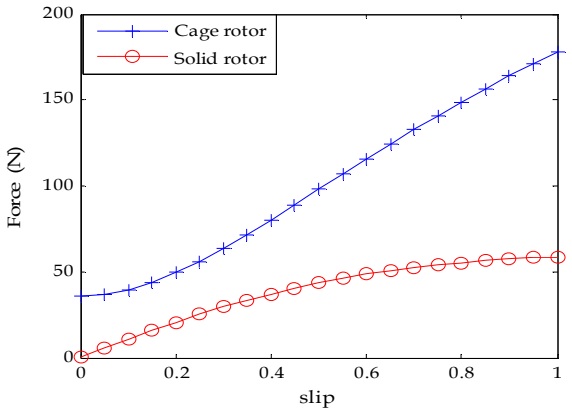

Fig 5-56. Characteristic of force vs slip when the motors with cage and solid rotor are supplied with the same excitation current.

Note that the impedance of cage rotor is greater than the solid rotor. As a result, motor with cage rotor would have lower excitation current under constant voltage source (see Fig. 5-57). Therefore, to maintain the same excitation current; motor with cage rotor was fed by higher supply voltage.

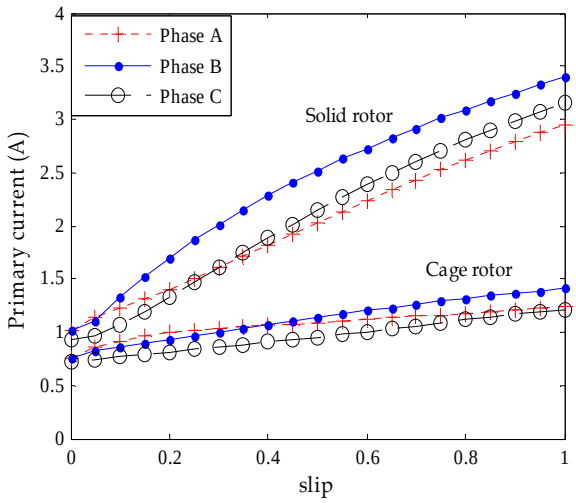

Fig 5-57. Primary current vs. slip characteristics calculated under constant balanced supply voltage equal to 86.6 V and frequency equal to 50 Hz with static end effect taken into account for both motors.

Unlike aluminum rings that provide a path for eddy currents to be induced in a perpendicular direction with respect to the traveling wave, aluminum bars are in parallel with the magnetic travelling field, thus, are not expected to contribute in improving the linear part motor performance. To study the contribution of the aluminum bars in improving the linear part motor performance the same analysis is done for the linear motor part with cage rotor with aluminum rings (Fig 5-58). Simulation results corresponding with this type of rotor are shown in Figs 5-59, 5-60 and 5-61. It is shown that the FEM results obtained for the cage rotor with aluminum rings

are almost equal the results previously obtained for the cage rotor with aluminum rings and bars meaning aluminum rings are the key part to improve the linear part motor performance.

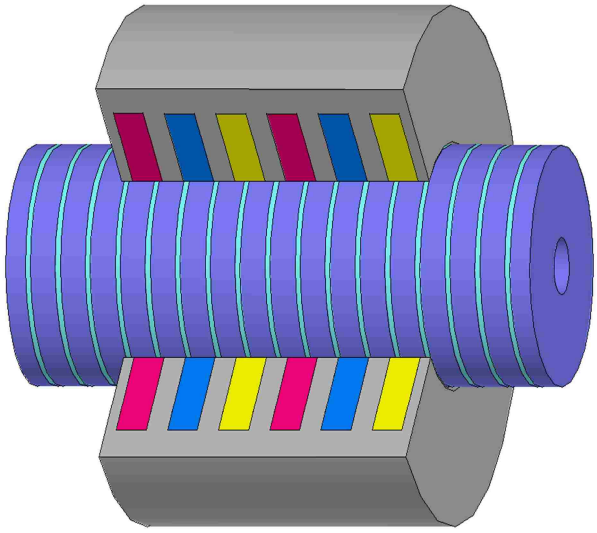

Fig 5-58. LIM with cage rotor (only with aluminum rings).

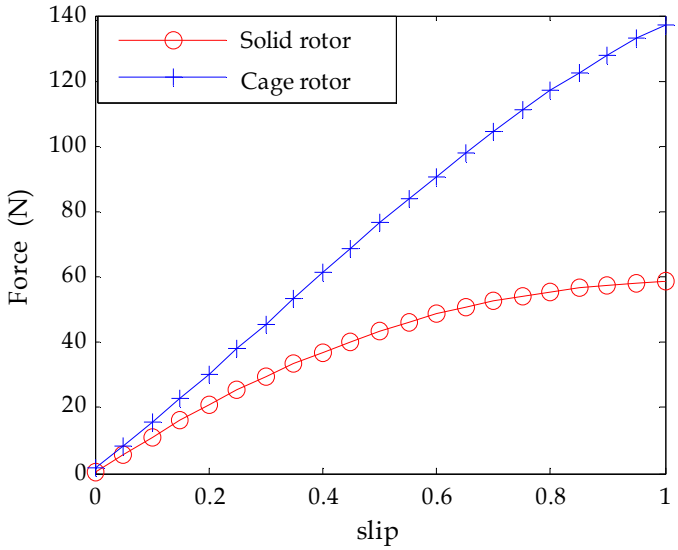

Fig 5-59. Characteristic of force vs slip when the motors with cage and solid rotor are supplied with the same excitation current.

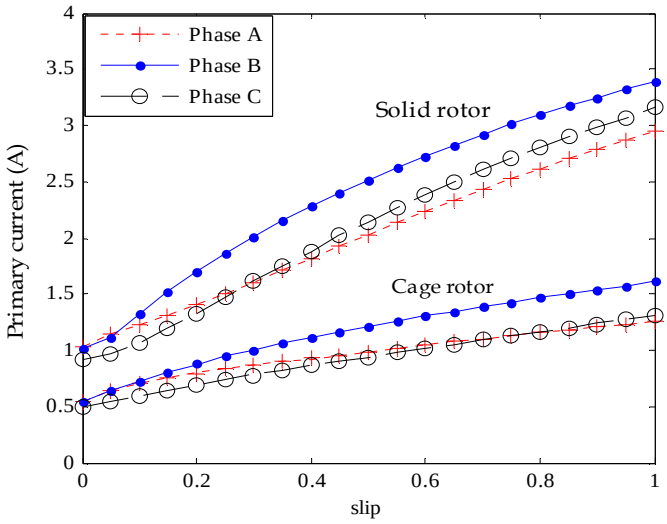

Fig 5-60. Primary current vs. slip characteristics calculated under constant balanced supply voltage equal to 86.6 V and frequency equal to 50 Hz with static end effect taken into account for both motors.

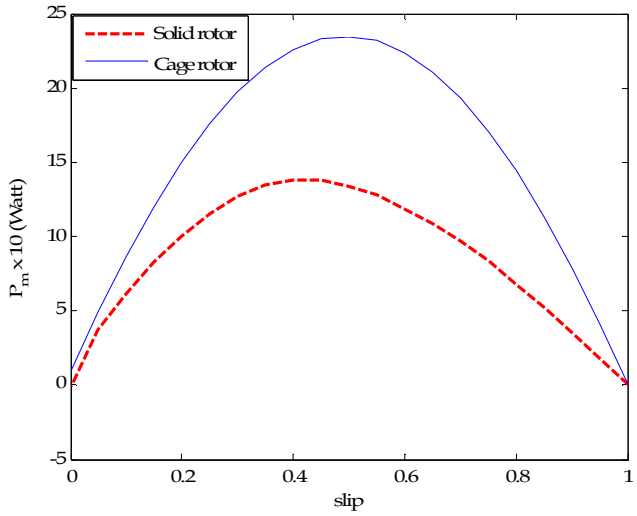

Fig 5-61. Characteristic of mechanical power vs. slip when the motors with cage and solid rotor are supplied with the same excitation current.

The 3-D schematic view of the rotary motor part with cage rotor is shown in Fig 5-60. In rotary armature, aluminum bars provide a path for eddy currents to be induced in a perpendicular direction with respect to the rotating wave, thus, contribute to rising up the electromagnetic

torque. However, the rotor resistivity and, thus, the electromagnetic torque may vary accordingly based upon the dimensions of the aluminum bars. Fig 5-61 shows the electromagnetic torque calculated for the cage rotor with two different bars' dimensions compared to the solid rotor.

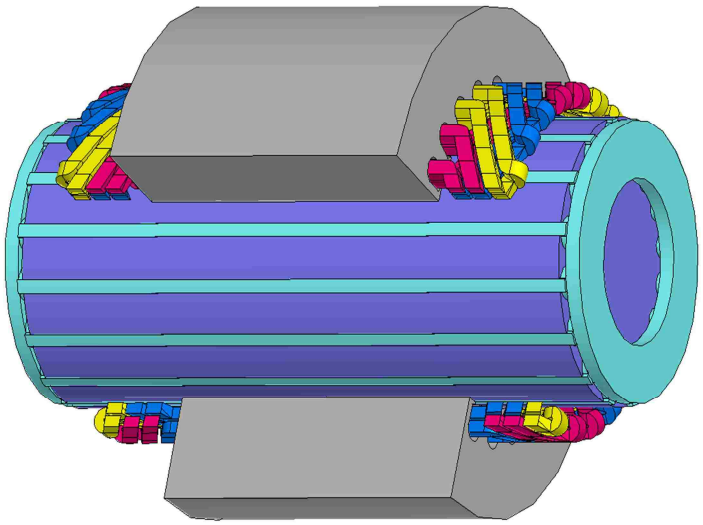

Fig 5-62. RIM with cage rotor (only with aluminum bars).

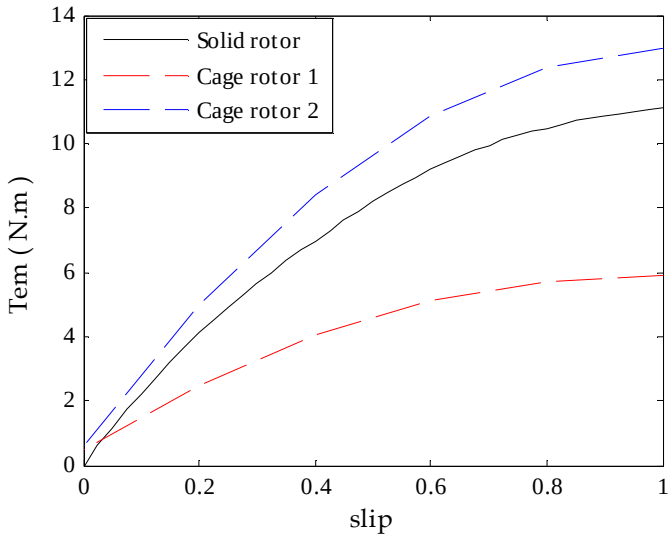

Fig 5-63. Characteristic of torque vs rotary slip calculated for the cage rotor with two different bars' dimensions compared to the solid rotor (motors are supplied with the same excitation current).

CHAPTER 6 : CONCLUSIONS AND PROPOSAL FOR FUTURE RESAERCH

6.1 Conclusions

The TARLIM, with two solid layer rotor was analyzed and its performance was determined using 3-D FEM and equivalent circuit model. The operation of the motor does not differ from the operation of machine set consisting of rotary and tubular linear motor of which rotors are firmly coupled. Thus, the analysis of the TARLIM was done separately for the motor with rotary and linear armature.

The performance of the motor is affected by the end effects and variation of electromagnetic field in the rotor. These two phenomena were taken into account in the motor performance analysis. The analysis was carried out using FEM modeling (applying field theory) and equivalent circuit.

By applying circuit modeling three equivalent circuits were developed.

- Circuit that does not include any end effect.
- Circuit that includes dynamic end effect.
- Circuit with static and dynamic end effect.

The development of different equivalent circuits enabled to independently study the impact of each phenomenon on the motor performance.

The equivalent circuits that were developed allow analyzing TARLIM performance in steady state under different supply and load conditions and are the major contribution of this dissertation to the induction motor theory.

The results obtained from circuit modeling, which characterizes the TARLIM operation were partially verified by the experimental results obtained from the measurements carried out on the physical motor model.

Motor with the rotor cage made in form of grid placed on the cylindrical core is another version of TARLIM that was analyzed. Its electromechanical characteristics were compared with the ones obtained for motor with two solid layer rotor. In motor with the cage rotor, copper layer is replaced with aluminum rings resulting in a lower effective air gap with respect to the motor with solid rotor. The major conclusion deducted from this comparative analysis is that the motor with cage rotor could develop higher force if the dimension of aluminum rings is optimized.

6.2 Future Works

For further researches in this area, the following tasks could be added:

- Analysis of double winding rotary-linear induction motor in which one winding overlaps another. In this model all windings (rotary and linear part) are placed in one armature and the benefits of the modified model in terms of performances, volume, weight and cost are studied.
- Dynamic analysis of the motor.
- Study the influence of static and dynamic end effects on one another.
- Find the optimized thickness for the rotor layer.

REFERENCES

[1] E.Mendrela, J,Fleszar, E,Gierczak. Modeling of Induction Motors with One and Two Degrees of Mechanical Freedom. Norwell, MA: Kluwer Academic Publishers, 2003.

[2] G. Krebs, A. Tounzi, B. Pauwels and D. Willemot, "General overview of integrated linear rotary actuators," *in Proc. ICEM 2008 Conf.*

[3] Bolognesi P, Bruno O, Landi A, Sani L, Taponecco L. Electromagnetic actuators featuring multiple degrees of freedom: a survey. In: ICEM conference, Krakow (Poland), 5–8 September 2004.

[4] B. Giancarlo and B. Tellini, "Helicoidal electromagnetic field for coilgun armature stabilization," *IEEE Trans. Magn.*, vol. 39, no. 1, pp. 108–111, Jan. 2003.

[5] Anorad Corp., New York, USA, "Rotary linear actuator," U.S. Patent 6 215 206, Oct. 4, 2001.

[6] S. Yamamura, Theory of Linear Induction Motors, John Wiley & Sons, 1972.

[7] R. C. Creppe, J. A. C. Ulson, and J. F. Rodrigues, "Influence of design parameters on linear induction motor end effect," *IEEE Trans. Energy Convers.*, vol. 23, no. 2, pp. 358–362, Jun. 2008.

[8] J. Faiz, H. Jafari, Accurate Modelling of Single-Sided Linear Induction Motor Considers End Effect and Equıvalent Thickness, IEEE Transactions on Magnetic, 36, (2000).

[9] J. Turowski, Electromagnetic calculations of machine elements and electro mechanics. WNT Warsaw, 1982. (in Polish).

[10] E.Gierczak, E.Mendrela "Magnetic flux, current, force and power loss distribution in twin-armature rotary-linear induction motor", Scientia Electrica, Vo. 31, pp. 65-74, 1985.

[11] H. Mosebach, T. Huhns, E.S. Pierson, D. Herman, "Finite Length Effects in Linear Induction Machines with Different Iron Contours" IEEE Trans. On PAS-96, 1977, pp. 1087-1093.

[12] M. Poloujadoff, B. Morel, A. Bolopion, "Simultaneous Consideration of Finite Length and Finite Width of Linear Induction Motors" IEEE Trans. On PAS, Vol. PAS-99, No. 3, 1980, pp. 1172-1179.

[13] Pai, R.M., Boldea, I., and Nasar, S.A.: 'A complete equivalent circuit of a linear induction motor with sheet secondary', IEEE. Trans., 1988, MAG-24, (1), pp. 639–654.

[14] J. F. Gieras, G. E. Dawson, and A. R. Eastham, "A new longitudinal end effect factor for linear induction motors," *IEEE Trans. Energy Convers.*, vol. 2, no. 1, pp. 152–159, Mar. 1987.

[15] T. Hirasa, S. Ishikawa, and T. Yamamuro, “Equivalent circuit of linear induction motors with end effect taken into account,” *Trans. IEE Jpn.*, vol. 100, no. 2, pp. 65–71, 1980.

[16] J. Duncan, “Linear induction motor—Equivalent circuit model,” *Proc. Inst. Elec. Eng.*, pt. B, vol. 130, no. 1, 1983.

[17] M. Mirsalim, A. Doroudi, and J. S. Moghani, “Obtaining the operating characteristics of linear induction motors: A new approach,” IEEE Trans. Magn., vol. 38, no. 2, pp. 1365–1370, Mar. 2002.

[18] B. I. Kwon, K. I. Woo, and S. Kim, “Finite element analysis of direct thrust controlled linear induction motor,” IEEE Trans. *Magn*., vol. 35, no. 3, pp. 1306–1309, May 1999.

[19] N. Fujii , T. Kayasuga and T. Hoshi "Simple end effect compensator for linear induction motor", *IEEE Trans. Magn.*, vol. 38, no. 5, pp.3270 -3272 2002.

[20] D.-k. Kim and B.-I. Kwon, “A novel equivalent circuit model of linear induction motor based on finite element analysis and and its coupling with external circuits,” IEEE Trans. Magn., vol. 42, no. 10, pp. 3407–3409, Oct. 2006.

[21] G. Krebs, A. Tounzi, B. Pauwels, D. Willemot, and F. Piriou, “Modeling of a linear and rotary permanent magnet actuator,” IEEE Trans. Magn., vol. 44, no. 10, pp. 4357-4360, Nov. 2008.

[22] E. Amiri, P. Gottipati, E. A. Mendrela, “ 3-D Space Modeling of Rotary-Linear Induction Motor With Twin-Armature” The 1st IEEE International Conference on Electrical Energy Systems, Chennai, Tamil Nadu, India, Jan 2011.

[23] M. Poloujadoff, “ The Theory of Linear Induction Machinery” Oxford University Press, 1980.

[24] E. Mendrela, “Electric Machines”, Course Pack “Advanced Electric Machine”, Louisiana State University, 2004.

[25] Ion Boldea, S.A.Nasar, Linear Motion Electromagnetic Devices, Taylor and Francis, 2001.

[26] Clough, R. W., Original Formulation of the Finite Element Method, Finite Elements in Analysis and Design 7, pp. 89-101, 1991.

[27] Chari, M.V.K.; Silvester, P.; Finite-Element Analysis of Magnetically Saturated D-C Machines, IEEE Trans. on PAS, Vol.PAS-90 1971,pp.2362 to 2372.

[28] P. Silvester, H.S. Cabayan and B.T.Browne Efficient techniques for finite element analysis of electric machines, IEEE Trans. on PAS, Vol.PAS-92 1973,pp.1274 to 1281.

[29] Fahmy, S.M.; Browne, B.T.; Silvester, P.; Barton, T.H.; The open-circuit magnetic field of a saturated synchronous machine, an experimental and computational study, IEEE Trans. on PAS, Vol.PAS-94 1975,pp.1584 to 1588.

[30] Chai Feng; Cui Shumei; Cheng Shukang; Study of a novel double-stator permanent-magnet electric machine, Electric Machines and Drives Conference, 2003. IEMDC'03. IEEE International, Volume 3:1375-1378, June 2003.

[31] Salon, S.; Chari, M.; Sivasubramaniam, K.; O-Mun Kwon; Selvaggi, J.; Computational Electromagnetics and the Search for Quiet Motors, IEEE Transactions on Magnetics, 45(3):1694-1699, Mar. 2009.

[32] Nakata, T.; Takahashi, N.; Fujiwara, K.; Ahagon, A.; 3-D finite element method for analyzing magnetic fields in electrical machines excited from voltage sources, IEEE Transactions on Magnetics, 24(6):2582-2584, November 1988.

[33] Righi, L.A.; Sadowski, N.; Carlson, R.; Bastos, J.P.A.; Batislsla, N.J.; A new approach for iron losses calculation in voltage fed time stepping finite elements , IEEE Transactions on Magnetics, 37(5)Part 1:3353-3356, Sept 2001.

[34] Lu, J.; Yamada, S.; Bessho, K.; Harmonic balance finite element method taking account of external circuits and motion, IEEE Transactions on Magnetics, 27(5),pp.4024-4027, Sept, 1991.

[35] Ha, K.H.; Hong, J.P.; Dynamic rotor eccentricity analysis by coupling electromagnetic and structural time stepping FEM, IEEE Transactions on Magnetics, 37(5):3452-3455, Sept. 2001.

[36] S. Li and H. Hofmann. Numerically efficient steady-state finite element analysis of magnetically saturated electromechanical devices using a shooting newton/gmres approach. IEEE Transactions on Magnetics, 39(6):3481–5, November 2003.

[37] Saitz,J:, Magnetic field analysis of induction motors combining Preisach hysteresis modeling and finite element techniques, IEEE Transactions on Magnetics, 37(5)Part1:3693-3697, Sept. 2001.

[38] Isaac, F.N.; Arkadan, A.A.; El-Antably, A.; Magnetic field and core loss evaluation of ALA-motor synchronous reluctance machines taking into account material anisotropy, IEEE Transactions on Magnetics, 34(5)Part1:3507-3510, Sept. 1998.

[39] David Meeker, "Finite Element Method Magnetics, Version 4.2, User's Manual" November 26, 2009.

[40] Maxwell v12 Magnetostatic Guide, Ansoft Corporation, USA, February 2008.

[41] Yasuharu Ohdachi, Yoshihiro Kawase and Masaru Hirako Dynamic analysis of vector controlled induction motor using finite element method, IEEE Transactions on Magnetics, vol.31,pp.1904-1907,1995.

[42] B.Davat, Z.Ren and M.Lajoie-Mazenc The movement in field modeling *IEEE Transactions on Magnetics, vol.21,pp.2296-2298,* November, 1985.

[43] Herbert De Gersem and Thomas Weiland Harmoinc weighting functions at the sliding interface of a finite-element machine model incorporating angular displacement, *IEEE Transactions on Magnetics, vol.40,pp.545-548,* March,2004.

[44] N.Sadowski,Y.Lefevre,M.Lajoie-Mazenc,J.Cros, Finite element torque calculation in electrical machines while considering the movement, *IEEE Transactions on Magnetics, vol.28,pp.1410-1413,* March, 1992.

[45] Andrzej Demenko, Movement simulation in finite element analysis of electric machine dynamics, *IEEE Transactions on Magnetics, vol.32,pp.1553-1556,* May, 1996.

[46] T.W.Preston, A.B.J.Reese, P.S.Sangha Induction motor analysis by timestepping techniques, IEEE Transactions on Magnetics, vol.24,pp.471- 474, January,1988.

[47] I.Tsukerman, J.D.Lavers, A.Konrad Using complementary formulations for accurate computations of magnetostatic fields and forces in a synchronous motor, IEEE Transactions on Magnetics, vol.30,pp.3479-3482,September,1994.

[48] D.Rodger,H.C.Lai and P.J.Leonard Coupled elements for problems involving movement, IEEE Transactions on Magnetics, vol.26,pp.548-550, March, 1990.

[49] A.A.Abdel-razek, J.L.Coulomb, M.Feliachi, J.C.Sabonnadiere, ”Conception of an air-gap element for the dynamic analysis of the electromagnetic field in electric machines,” IEEE Transactions on Magnetics, Vol.18,pp.655-659, March 1982.

[50] M.Trlep,L.Skerget,B.Kreca, B.Hribernik, Hybrid finite element-boundary element method for nonlinear electromagnetic problems, IEEE Trans. on Magnetics, vol.31,pp.1380-1383, May, 1995.

[51] H. Yu, R. Jayabalan, B. Fahimi, M. Moallem, "Field Oriented Linear Induction Motor Drives: An Electromagnetic Perspective", Electromagnetic Field Computation, 2006, 12 Biennial IEEE Conference, 2006, pp. 282-282.

[52] A. Yahioui, F. Bouillault, 2D and 3D numerical computation of electrical parameters of an induction motor, IEEE Trans. Magn. 30 (5) (1994) 3690–3692.

[53] Ping Zhou, John Gilmore Zsolt Badics, Zoltan J.cendes., “Finite element Analysis of Induction motors based on computing detailed Equivalent circuit Parameters.,” IEEE Trans. On Magnetics, vol. 34, no.5, pp.3499-3502 Sep 1998.

[54] D. Dolinar, G. ˇStumberger, and B. Grˇcar, “Calculation of the linear induction motor model parameters using finite elements,” IEEE Transactions on Magnetics, vol. 34, no. 5, pp. 3640–3643, 1998.

[55] Rinkevičienė R., Petrovas A. “Dynamic Models of Linear Induction Drive”, Information Technology and Control, ISSN 1392-124x. – Kaunas: Technologija, 2005, Vol. 34, No. 1, pp. 37 – 41.

[56] KANG, G.—NAM, K. : Field-Oriented Control Scheme for Linear Induction Motor with the End Effect, IEE Proc., Electric Power Application 152 No. 6 (Nov 2005), 1565-1572.

[57] A. Nasar, Linear Electric Motors, Theory, Design and Practical Application.Englewood Cliffs, NJ: Prentice-Hall, 1987.

[58] S. A. Nasar and I. Boldea, Linear Motion Electric Machines. New York: Wiley, 1976, pp. 127–128.

[59] P. C. Sen, Principles of Electric Machines and Power Electronics. New York: John Wiley & Sons, 1989, pp. 377-391.

[60] Ebrahim Amiri and Ernest Mendrela, Induction Motors with Rotor Helical Motion, Induction Motors - Modelling and Control, Prof. Rui Esteves Araújo (Ed.), ISBN: 978-953-51-0843-6, pp 247-274, InTech, 2012.

APPENDIX A: PRIMARY RESISTANCE (R_1) CALCULATIONS

The primary resistance can be obtained directly from motor data as follows:

$$R_1 = L_{c,av} \times N_W \times N_C \times R_r \times \frac{10^{-3}}{m} = 0.378 \times 215 \times 6 \times 13.17 \times \frac{10^{-3}}{3} = 2.22\Omega$$

where $L_{c,av}$ is the average length of the coil and is denoted by:

$$L_{c,av} = \pi . r . 2 = \pi * 120.5 * 2 = 378.4 \text{ mm}$$

- r is the radius of the coil at the center
- $N_W$is the number of turns per coil
- N_C is the number of coils
- R_r is the resistance per kilometer of the AWG wire
- m is the number of phases

The stator phase resistance obtained from FEM model is 2.165 Ω which is close to the value obtained straight from motor data.

APPENDIX B: TRANSIENT WINDING CURRENT CALCULATION IN FEM

A capacitance matrix represents the relationship between currents and time varying voltages in a system of conductors. Given the three transmission lines shown in Fig 1, the currents caused by the time varying voltage source on each line are given by the following equation:

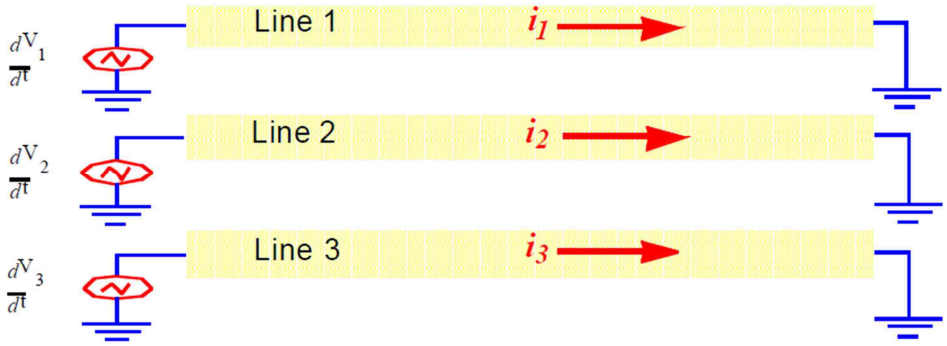

Current caused by 3 phase time varying voltage source in a 3 phase line.

$$\begin{bmatrix} i_1 \\ i_2 \\ i_3 \end{bmatrix} = \begin{bmatrix} C_{10}+C_{12}+C_{13} & -C_{12} & -C_{13} \\ -C_{12} & C_{20}+C_{12}+C_{23} & -C_{23} \\ -C_{13} & -C_{23} & C_{30}+C_{13}+C_{23} \end{bmatrix} \begin{bmatrix} \frac{dV_1}{dt} \\ \frac{dV_2}{dt} \\ \frac{dV_3}{dt} \end{bmatrix}$$

APPENDIX C: PRIMARY LEAKAGE INDUCTANCE (L_1) CALCULATIONS

To determine the primary phase leakage inductance L_1 the FEM model is used with the boundary conditions on the secondary surface as shown in Fig. 2. Only the phase A is supplied with DC current. The phase inductance in this case is the leakage inductance (the magnetic flux does not link the primary part). L_1 = 0.0366 H

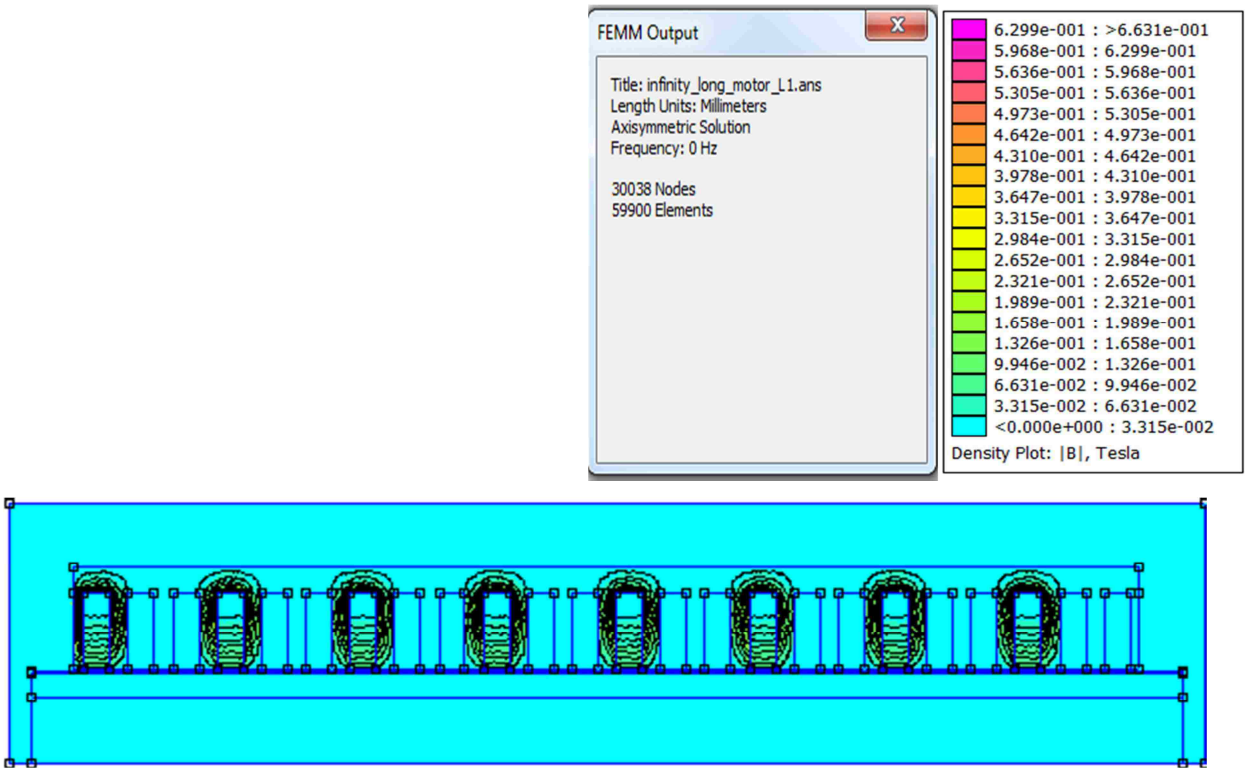

Leakage flux generated by phase A.

APPENDIX D: PERMISSIONS TO REPRINT

Permission from the author

Ebrahim Amiri <eamiri3@tigers.lsu.edu>

Permission to Reprint
3 messages

Ebrahim Amiri <eamiri3@tigers.lsu.edu> Tue, Nov 12, 2013 at 1:56 PM
To: Ernest Mendrela <ermen1@lsu.edu>

Dear Prof. Ernest Mendrela,

I am requesting permission to reprint [a portion of] the following work:

E.Mendrela, J,Fleszar, E,Gierczak. Modeling of Induction Motors with One and Two Degrees of Mechanical Freedom. Norwell, MA: Kluwer Academic Publishers, 2003.

This request is for permission to include the above content as part of the following project that I am preparing:

Ebrahim Amiri, "Induction motors with rotor helical motion" Doctorate Dissertation, Louisiana State University, December 2013.

This request is for a non-exclusive, irrevocable, and royalty-free permission, and it is not intended to interfere with other uses of the same work by you. I would be pleased to include a full citation to your work and other acknowledgement as you might request.

Sincerely,

Ebrahim Amiri

Ernest Mendrela <ermen1@lsu.edu> Tue, Nov 12, 2013 at 4:31 PM
To: Ebrahim Amiri <eamiri3@tigers.lsu.edu>

Hi Ebrahim,

My Permission is hereby granted.

Ernest Mendrela
Louisiana State University
Division of Electrical and Computer Engineering
School of Electrical Engineering and Computer Science
3106B Patrick F. Taylor Hall
Baton Rouge, LA 70803

Date: 11/12/2013

Permission from the publisher

Ebrahim Amiri <eamiri3@tigers.lsu.edu>

RE: TN 203177 Permission to reprint DA

1 message

Permissions Europe/NL <Permissions.Dordrecht@springer.com> Wed, Nov 13, 2013 at 7:59 AM
To: "eamiri3@tigers.lsu.edu" <eamiri3@tigers.lsu.edu>

Dear Sir,

With reference to your request to reprint material in which Springer Science and Business Media control the copyright, our permission is granted free of charge and at the following conditions:

Springer material

- represents original material which does not carry references to other sources (if material in question refers with a credit to another source, authorization from that source is required as well);
- requires full credit [Springer and the original publisher/journal title, volume, year of publication, page, chapter/article title, name(s) of author(s), figure number(s), original copyright notice] to the publication in which the material was originally published, by adding; with kind permission from Springer Science+Business Media B.V.;
- may not be altered in any manner. Abbreviations, additions, deletions and/or any other alterations shall be made only with prior written authorization of the author and/or Springer Science + Business Media.
- may not be republished in Electronic Open Access.

This permission

a. is non-exclusive.
b. includes use in an electronic form: provided it's password protected, or on intranet or university's repository, including UMI (according to the definition at the Sherpa website: http://www.sherpa.ac.uk/romeo/), or CD-Rom/E-book,
c. is subject to a courtesy information to the author (address is given with the article/chapter).
d. is personal to you and may not be sublicensed, assigned, or transferred by you to any other person without Springer's written permission.
e. is valid only when the conditions noted above are met.

Permission free of charge on this occasion does not prejudice any rights we might have to charge for reproduction of our copyrighted material in the future.

Best regards,

Kind regards,

Nel van der Werf (Ms)

Rights and Permissions/Springer

Van Godewijckstraat 30 | P.O. Box 17

3300 AA Dordrecht | The Netherlands

tel +31 (0) 78 6576 298

fax +31 (0)78 65 76-377

Nel.vanderwerf @springer.com

www.springer.com

From: Ebrahim Amiri [mailto:eamiri3@tigers.lsu.edu]
Sent: Friday, November 08, 2013 12:47 AM
To: Journal Service Springer NY
Subject: Permission to reprint

Dear Kluwer Academic Publisheres Group,

This is Ebrahim Amiri, PhD Candidate in Electrical and Computer Engineering Dept of Louisiana State University. I am requesting permission to reprint [a portion of] the following work

E.Mendrela, J,Fleszar, E,Gierczak. "Modeling of Induction Motors with One and Two Degrees of Mechanical Freedom". Norwell, MA: Kluwer Academic

Publishers, 2003.

This request is for permission to include a portion of the above content as part of the following project that I am preparing under the supervision of the Prof. Ernest Menedrela

Ebrahim Amiri, "Induction motors with rotor helical motion" Doctorate Dissertation, Louisiana State University, December 2013.

Prof Mendrela has already given me the permission to reprint a part of his book into my dissertation but permission is also needed from the publisher.

The following request is also attached in the word file.

I appreciate your time.

Sincerely,
Ebrahim Amiri

SPRINGER LICENSE
TERMS AND CONDITIONS

Nov 12, 2013

This is a License Agreement between Ebrahim Amiri ("You") and Springer ("Springer") provided by Copyright Clearance Center ("CCC"). The license consists of your order details, the terms and conditions provided by Springer, and the payment terms and conditions.

All payments must be made in full to CCC. For payment instructions, please see information listed at the bottom of this form.

License Number
3266650059582
License date
Nov 12, 2013
Licensed content publisher
Springer
Licensed content publication
Springer eBook
Licensed content title
Chapter 1: Introduction
Licensed content author
Ernest Mendrela
Licensed content date
Jan 1, 2003
Type of Use
Thesis/Dissertation
Portion
Full text
Number of copies
1
Author of this Springer article
No
Order reference number
Title of your thesis / dissertation
Induction motors with rotor helical motion
Expected completion date
Dec 2013
Estimated size(pages)
120
Total
0.00 USD

SPRINGER LICENSE
TERMS AND CONDITIONS

Nov 12, 2013

This is a License Agreement between Ebrahim Amiri ("You") and Springer ("Springer") provided by Copyright Clearance Center ("CCC"). The license consists of your order details, the terms and conditions provided by Springer, and the payment terms and conditions.

All payments must be made in full to CCC. For payment instructions, please see information listed at the bottom of this form.

License Number
3266641291709
License date
Nov 12, 2013
Licensed content publisher
Springer
Licensed content publication
Springer eBook
Licensed content title
Chapter 2: Mono-Harmonic Induction Motor with Two Degrees of Mechanical Freedom (IM-2DMF)
Licensed content author
Ernest Mendrela
Licensed content date
Jan 1, 2003
Type of Use
Thesis/Dissertation
Portion
Full text
Number of copies
1
Author of this Springer article
No
Order reference number
Title of your thesis / dissertation
Induction motors with rotor helical motion
Expected completion date
Dec 2013
Estimated size(pages)
120
Total
0.00 USD

Terms and Conditions

Introduction
The publisher for this copyrighted material is Springer Science + Business Media. By clicking "accept" in connection with completing this licensing transaction, you agree that the following terms and conditions apply to this transaction (along with the Billing and Payment terms and conditions established by Copyright Clearance Center, Inc. ("CCC"), at the time that you opened your Rightslink account and that are available at any time at http://myaccount.copyright.com).

Limited License
With reference to your request to reprint in your thesis material on which Springer Science and Business Media control the copyright, permission is granted, free of charge, for the use indicated in your enquiry.

Licenses are for one-time use only with a maximum distribution equal to the number that you identified in the licensing process.

This License includes use in an electronic form, provided its password protected or on the university's intranet or repository, including UMI (according to the definition at the Sherpa website: http://www.sherpa.ac.uk/romeo/). For any other electronic use, please contact Springer at (permissions.dordrecht@springer.com or permissions.heidelberg@springer.com).

The material can only be used for the purpose of defending your thesis, and with a maximum of 100 extra copies in paper.

Although Springer holds copyright to the material and is entitled to negotiate on rights, this license is only valid, subject to a courtesy information to the author (address is given with the article/chapter) and provided it concerns original material which does not carry references to other sources (if material in question appears with credit to another source, authorization from that source is required as well).

Permission free of charge on this occasion does not prejudice any rights we might have to charge for reproduction of our copyrighted material in the future.

Altering/Modifying Material: Not Permitted
You may not alter or modify the material in any manner. Abbreviations, additions, deletions and/or any other alterations shall be made only with prior written authorization of the author(s) and/or Springer Science + Business Media. (Please contact Springer at (permissions.dordrecht@springer.com or permissions.heidelberg@springer.com)

Reservation of Rights
Springer Science + Business Media reserves all rights not specifically granted in the combination of (i) the license details provided by you and accepted in the course of this licensing transaction, (ii) these terms and conditions and (iii) CCC's Billing and Payment terms and conditions.

Copyright Notice:Disclaimer
You must include the following copyright and permission notice in connection with any reproduction of the licensed material: "Springer and the original publisher /journal title, volume, year of publication, page, chapter/article title, name(s) of author(s), figure number(s), original copyright notice) is given to the publication in which the material was originally published, by adding; with kind permission from Springer Science and Business Media"

Warranties: None

Example 1: Springer Science + Business Media makes no representations or warranties with respect to the licensed material.

Example 2: Springer Science + Business Media makes no representations or warranties with respect to the licensed material and adopts on its own behalf the limitations and disclaimers established by CCC on its behalf in its Billing and Payment terms and conditions for this licensing transaction.

Indemnity
You hereby indemnify and agree to hold harmless Springer Science + Business Media and CCC, and their respective officers, directors, employees and agents, from and against any and all claims arising out of your use of the licensed material other than as specifically authorized pursuant to this license.

No Transfer of License
This license is personal to you and may not be sublicensed, assigned, or transferred by you to any other person without Springer Science + Business Media's written permission.

No Amendment Except in Writing
This license may not be amended except in a writing signed by both parties (or, in the case of Springer Science + Business Media, by CCC on Springer Science + Business Media's behalf).

Objection to Contrary Terms
Springer Science + Business Media hereby objects to any terms contained in any purchase order, acknowledgment, check endorsement or other writing prepared by you, which terms are inconsistent with these terms and conditions or CCC's Billing and Payment terms and conditions. These terms and conditions, together with CCC's Billing and Payment terms and conditions (which are incorporated herein), comprise the entire agreement between you and Springer Science + Business Media (and CCC) concerning this licensing transaction. In the event of any conflict between your obligations established by these terms and conditions and those established by CCC's Billing and Payment terms and conditions, these terms and conditions shall control.

Jurisdiction
All disputes that may arise in connection with this present License, or the breach thereof, shall be settled exclusively by arbitration, to be held in The Netherlands, in accordance with Dutch law, and to be conducted under the Rules of the 'Netherlands Arbitrage Instituut' (Netherlands Institute of Arbitration).***OR:***

All disputes that may arise in connection with this present License, or the breach thereof, shall be settled exclusively by arbitration, to be held in the Federal Republic of Germany, in accordance with German law.

Other terms and conditions:

v1.3

If you would like to pay for this license now, please remit this license along with your payment made payable to "COPYRIGHT CLEARANCE CENTER" otherwise you will be invoiced within 48 hours of the license date. Payment should be in the form of a check or money order referencing your account number and this invoice number RLNK501157610.
Once you receive your invoice for this order, you may pay your invoice by credit card. Please follow instructions provided at that time.

Make Payment To:

VITA

Ebrahim Amiri was born, in 1982, in Kermanshah, Iran. He received the B.S. and M.S. degrees in Electrical Engineering from Amirkabir University of Technology, Tehran, Iran, in 2005 and 2008 respectively. With a continued interest in the field of machine design, he joined the doctoral program at LSU, where he is currently a candidate for the degree of Doctor of Philosophy. He held an internship with Entergy Inc. Mississippi, USA in summer 2013 and is currently an Assistant Professor of Electrical and Computer Engineering at Jackson State University, Jackson, MS, USA. His current research interests include electric machines, electric drives and power electronics.